ISSN 2432-8375

BULLETIN OF THE

LABORATORY FOR ADVANCED NUCLEAR ENERGY

VOL. 5 2020

LABORATORY FOR ADVANCED NUCLEAR ENERGY
INSTITUTE OF INNOVATIVE RESEARCH
TOKYO INSTITUTE OF TECHNOLOGY

BULLETIN OF THE LABORATORY FOR ADVANCED NUCLEAR ENERGY

(Formerly, BULLETIN OF THE RESEARCH LABORATORY FOR NUCLEAR REACTORS)

Abbreviation of the "**BULLETIN OF THE LABORATORY FOR ADVANCED NUCLEAR ENERGY**" is BULL. LAB. ADV. NUCL. ENERGY

All communications should be addressed to the editor, Laboratory for Advanced Nuclear Energy, Institute of Innovative Research, Tokyo Institute of Technology (Tokyo Kogyo Daigaku),
2-12-1-N1-16, O-okayama, Meguro-ku, Tokyo 152-8550, Japan.

TEL. +81-3-5734-3052, FAX. +81-3-5734-2959, E-mail bulletin@lane.iir.titech.ac.jp

http://www.lane.iir.titech.ac.jp/

BULLETIN OF THE LABORATORY FOR ADVANCED NUCLEAR ENERGY
BULL. LAB. ADV. NUCL. ENERGY, Vol.5, 2020

CONTENTS

Research staffs of
THE LABORATORY FOR ADVANCED NUCLEAR ENERGY,
TOKYO INSTITUTE OF TECHONOGY
AS OF 2020 JAPANESE FISCAL YEAR

Director

Kenji TAKESHITA	Professor

Innovative Nuclear Energy System Division

Toru OBARA	Professor
Yukitaka KATO	Professor
Yoshinao KOBAYASHI	Professor
Tatsuya KATABUCHI	Associate Professor
Hiroshige KIKURA	Associate Professor
Masatoshi KONDO	Associate Professor
Jun NISHIYAMA	Assistant Professor
Hiroki TAKASU	Assistant Professor
Hideharu TAKAHASHI	Assistant Professor
Shintaro YASUI	Assistant Professor

Actinide Management Division

Kenji TAKESHITA	Professor
Koichiro TAKAO	Associate Professor
Takehiko TSUKAHARA	Associate Professor
Masahiko NAKASE	Assistant Professor
Naokazu IDOTA	Assistant Professor

Global Nuclear Security Division

Hiroshi SAGARA	Associate Professor
Katsumi YOSHIDA	Associate Professor
Tetsuo SAWADA	Assistant Professor
Anna GUBAREVICH	Assistant Professor

Advanced Medical Application Division

Yoshiyuki OGURI	Professor
Noriyosu HAYASHIZAKI	Professor
Yoshihisa MATSUMOTO	Associate Professor
Jun HASEGAWA	Associate Professor
Mikio SHIMADA	Assistant Professor

Fundamental Research Division

Shunji IIO	Professor
Satoshi CHIBA	Professor
Hiroshi AKATSUKA	Associate Professor
Hiroaki TSUTSUI	Associate Professor
Chikako ISHIZUKA	Assistant Professor

Advanced Research and Education Program

Akira NISHIMURA	Specially Appointed Professor
Hideki MORI	Specially Appointed Associate Professor

Common Staffs

Hiroyasu MOCHIZUKI	Specially Appointed Professor
Tadashi NARABAYASHI	Specially Appointed Professor
Masahiro OKAMURA	Specially Appointed Professor
Satoru TSUSHIMA	Specially Appointed Associate Professor
Sunil CHIRAYATH	Specially Appointed Associate Professor
Hidekazu ASANO	Visiting Professor
Takatoshi TAKEMOTO	Visiting Associate Professor

Technical Staffs

Isao YODA	Senior Technical Specialist
Kazuo TAKEZAWA	Senior Technical Specialist
Ken-ichi TOSAKA	Senior Technical Specialist
Atsushi NEZU	Senior Technical Specialist
Hitoshi FUKUDA	Senior Technical Specialist

I. Special Article in Commemoration of Retiring Professor

I.1 Plasma Confinement Properties Learnt from Experiments on JT-60/JT-60U

Shunji Tsuji-Iio

1. Introduction

Since most of the studies I have conducted at Tokyo Tech since I joined the faculty in March, 1995 have been reported in these bulletin series, I briefly review the results of experiments on the JT-60/JT-60U tokamak in which I directly involved. I believe it is instructive to present those obtained in the late years of the 20th century including unpublished figures to young researchers on tokamaks.

2. JT-60 tokamak

JT (JAERI Torus) -60 was one of three large tokamaks in the world. It was designed to achieve the break-even condition required for the scientific demonstration of possible realization of fusion reactors. Its standard plasmas with nearly circular cross-sections were bounded by limiters made of initially TiC coated molybdenum, and later-on of graphite. When JT-60 was designed in 1970's, conventional circular cross-section with sizes shown in Fig. 1(a) was considered to be enough to confine plasmas satisfying the break-even condition. The approximate plasma volume of 60 m^3 was the origin of the number in the device name.

Exploiting the spacious volume in the outer side of tours in the bore of toroidal field (TF) coils left to reduce the TF ripple at the plasma edge, a set of divertor coils were installed in the vacuum vessel so that a divertor configuration with an outer X-point as illustrated in Fig. 1 (b) was uniquely possible in JT-60. Another divertor coil was added in the lower side of torus in 1990. Hence, the plasma confinement in three configurations, limiter and outer or lower X-points could be compared in the same device, the volume of the last configuration were smaller than those of the others though.

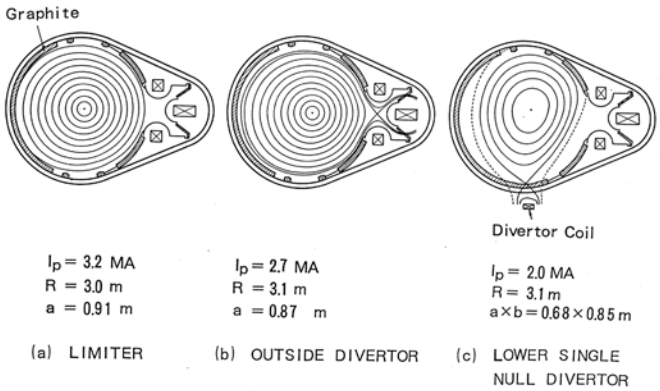

Fig. 1 Three plasma configurations could be formed in JT-60 with respective parameters at $B_t \leq 4.8$ T.

3. Diamagnetic measurement

3.1. Diamagnetic loop and Rogowski coil used for JT60

The energy confinement time, which is defined as the decay time of the plasma stored energy, is one of the three important parameters such as the ion temperature to evaluate the plasma confinement performance. It is calculated by dividing the plasma stored energy by the plasma heating power. The diamagnetic measurement is conventional and the most powerful method to evaluate the plasma stored energy since it measures both the ion and electron components together. Even when ion and electron temperature profiles and the electron density profile are obtained, it is not easy to estimate the ion component of the plasma stored energy since there is ambiguity to speculate the ion density distribution since it requires information not only on fuel density but also on impurity ion density profiles. The diamagnetic diagnostics however, is not easy to implement since the variation in the toroidal magnetic flux due to the plasma is less than one thousandth of the vacuum toroidal flux. That why good confinement reported on early tokamaks measured with diamagnetic loops in 1960s had been received suspiciously until it was confirmed by Thompson scattering diagnostics on electron temperature and density profiles by a U.K. team from the Culham laboratory.

The diamagnetic loop and a Rogowski coil for effective TF coil current including eddy currents flowing in the TF coil case made of manganese steel installed on JT-60 is shown in Fig. 2 [1]. Initially JT-t60 was not equipped with any diamagnetic loops. A return loop of a backup Rogowski coil for plasma current was converted as diamagnetic loop whose plane was tilted from the toroidally symmetric plane the torus axis by 5 degrees as shown in Fig, 2(b). So that not only it picked horizontal component of poloidal magnetic fields but also it coupled with plasma current depending on the vertical position of the current centroid. Hence numerical correction of them is a key to obtain accurate values of the diamagnetic flux.

Although it is common to use two loops with different linkage areas to cancel the vacuum toroidal magnetic flux, it was not possible to wind another loop inside the vacuum vessel. Accordingly, the effects of eddy currents flowing in the structures between the diamagnetic loop and the Rogowski coil such as the vacuum vessel and poloidal field coil supports were corrected with a circuit added to an analogue integrator with ultra-low drift.

3.2. Energy confinement in JT-60

The plasma stored energy of neutral beam (NB) heated hydrogen plasma in limiter configuration is plotted as a

function of absorbed heating power in Fig. 3 [2]. Note that the data points increase linearly with the heating power when the plasma current is kept constant and that its slope does not depend on the plasma current. The offsets rise with the plasma current. Power law scalings such as the Goldston scaling indicated by dashed curves in the figure do not fit well in low heating power ranges. Although power low scalings expressed by the products of operational parameters such as ITER scalings are useful to design tokamaks, they hide confinement physics in tokamaks. Since anomalous plasma transport has not been fully understood, the offset linear increase in the plasma stored energy with the heating power in L-mode should be revisited.

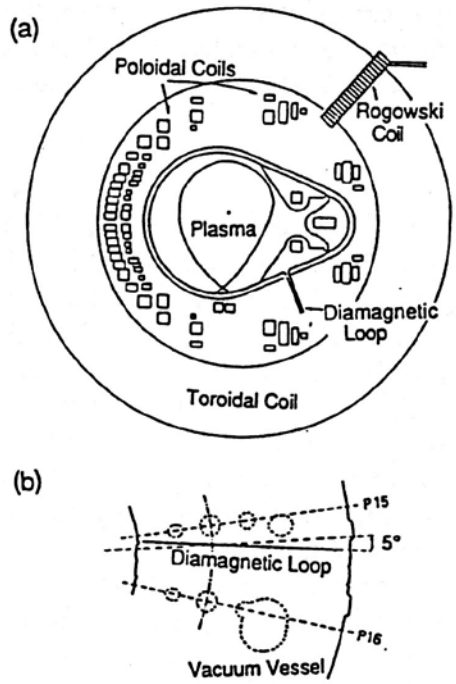

Fig. 2 Diamagnetic diagnostics installed on JT-60.

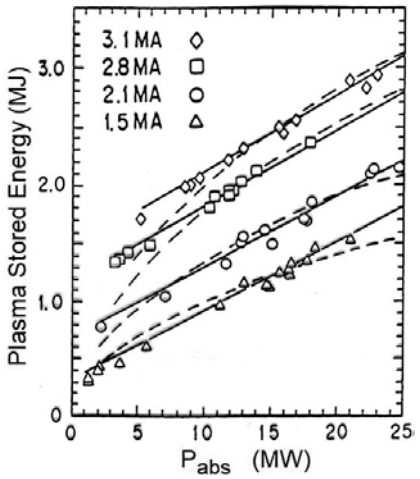

Fig. 3 Offset-linear increase in the plasma stored energy observed by diamagnetic measurements.

3.3. Plasma pressure anisotropy in JT-60

The diamagnetic flux reflects the plasma pressure perpendicular to magnetic fields and the poloidal beta separated from the internal inductance both contained in the Shafranov lambda from MHD equilibrium analysis gives the average value of parallel and perpendicular components of the poloidal beta. Consequently the plasma pressure anisotropy can be examined by subtracting the both values. Figure 4 shows example plots of shots in high β_p mode in JT-60 [3]. The pressure anisotropy rises with poloidal beta and drops with increasing line averaged electron density. Hence the anisotropy is interpreted to be caused by beam components supplied by NB injection.

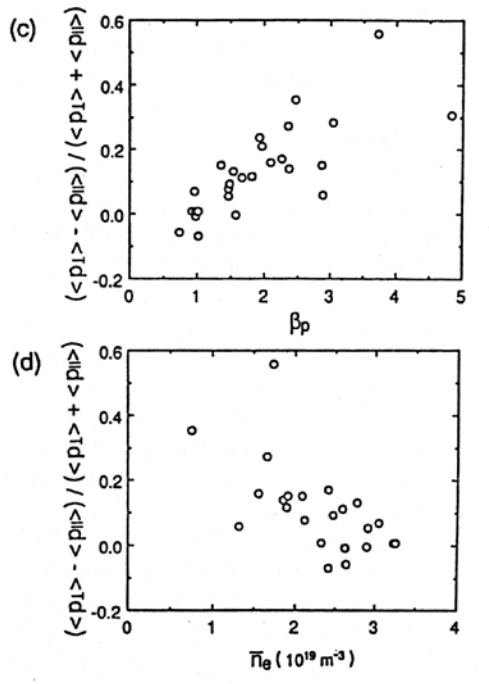

Fig. 4 Plasma pressure anisotropy evaluated in combination of diamagnetic measurement and MHD equilibrium analysis.

3. Particle confinement and divertor performance

3.1. Particle confinement

Particle confinement is an important aspect for evaluating plasma confinement properties as well as energy confinement. However, it has received less attention partly because quantitative measurements on particle confinement are scarce compared with those on energy confinement. Nevertheless, it is impossible to design realistic reactors without a quantitative evaluation of particle confinement. Suppression of the erosion of divertor plates and helium pumping are crucial issues for future reacting plasmas.

The main fueling source is particle recycling and its amount can be estimated from the intensity of Hα line emission since there is not much difference between the ionization energy and the energy to excite hydrogen atoms to a state with principal quantum number three. Moreover, absorption by atoms can be neglected in tokamak plasmas

since the Hα emission belongs to the Balmer series. It can be measured with interference filters and photodiodes. Hence multi-channel measurements are easily implemented. The line-integral nature of the measurement, however, necessitates tomographic tomographic analysis. Unless we subtract the fraction of the Hα emission radiating in the SOL, we estimate the particle confinement time slightly shifted to that defined at first walls [4].

The Hα emission was measured along three vertical chords in the outer X-point divertor configuration. The particle recycling in the divertor configurations is more axisymmetric than that in limiter ones, so that the errors in evaluating the total emission from one poloidal cross-section measurement are not so large. We used a two-dimetional and up-down symmetric neutral transport code [5] to evaluate the two-dimensional distribution from three chord data. The neutral particle distribution was determined by fitting the three-chord integrals of Ha emission to the experimental data. The collisional radiative model was adopted to estimate the number of ionizing hydrogen atoms from the Hα emission intensity.

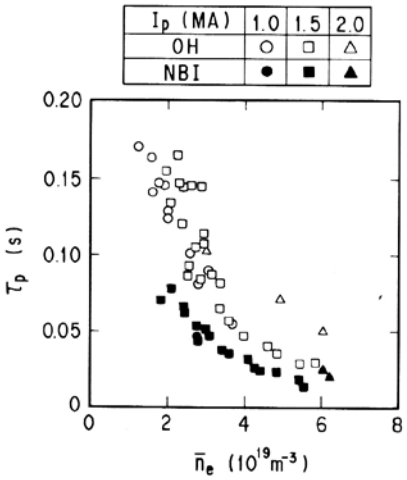

Fig. 5 Density dependence of particle confinement.

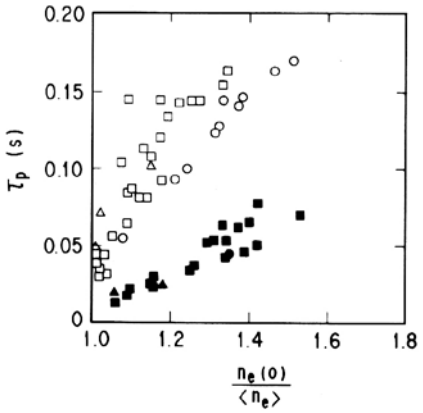

Fig. 6 Particle confinement time as a function of peaking parameter of electron density profile where < > means volume average.

Figure 5 shows the particle confinement tome drops with increasing electron density both in ohmic and beam-heated (PNB > 10 MW) plasmas. The time is about a few tens of milliseconds at high densities. The particle confinement time correlates well with the peaking of electron density profiles as indicated in Fig. 6, which can be explained by the observation that the particle recycling localizes more near the edge with increasing line-averaged density. Although the dependence on plasma current is weak, the particle confinement time tens to be longer with higher plasma current. Its values of NB plasmas are about one third of those of ohmic plasmas when compared with the same peaking factor of electron density.

The heating power dependence of the particle confinement time is plotted in Fig. 7. The particle confinement time falls in approximately inverse proportion to the square root of the heating power when the electron density peaking factor is nearly the same. This behavior is also the same as that of the energy confinement time.

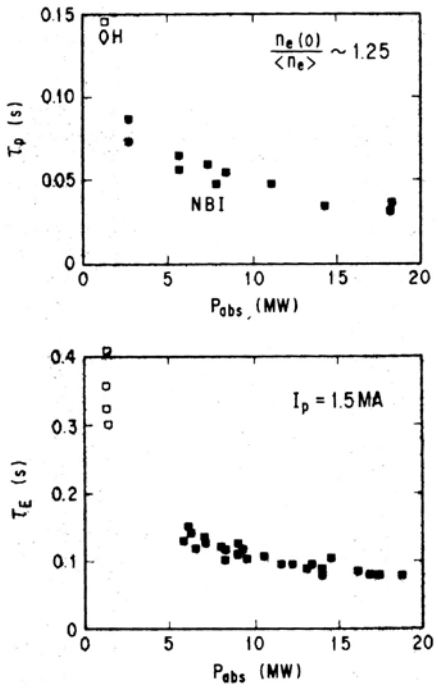

Fig. 7 Particle confinement degradation with heating power similar to energy confinement.

3.2. Particle exhaust

The anomalous particle confinement of plasmas heated by auxiliary is preferable with respect to the particle pumping. The neutral pressure in the divertor chamber monitored with an ion gauge shown in Fig. 8 increases approximately in proportion to the square of the line-averaged density because of the inversely linear dependence of the particle confinement time on density. The compression ratio of the neutral gas pressure of the divertor chamber to the main chamber was about 45 in outer X-point divertor configuration as can be seen from Fig. 9 for both Ohmic and NB heated discharges [6].

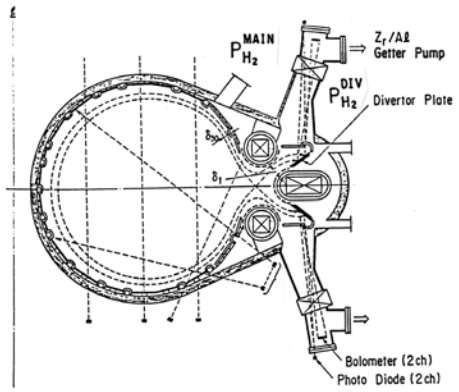

Fig. 8 Cross-sectional view of diagnostics and pumping ports for outer X-point divertor.

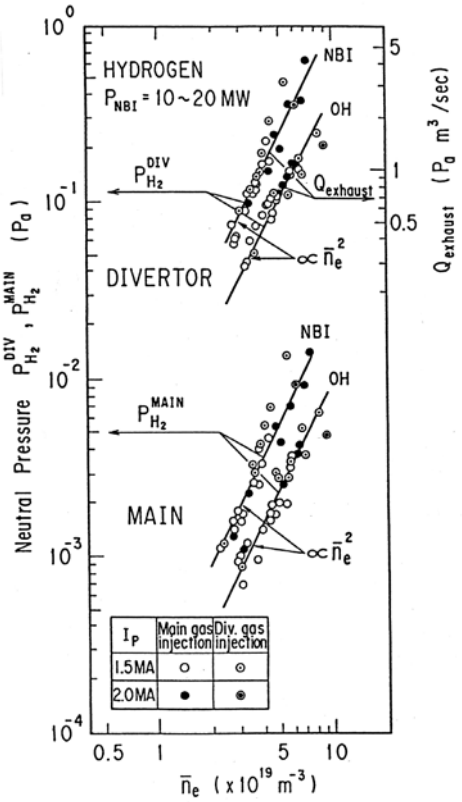

Fig. 9 Neutral pressures in the main and divertor chambers as a function of the line-averaged electron density. The particle exhaust rate is proportional to the divertor neutral pressure.

Owing to the high neutral pressure, the particles fueled by 75-keV NBI at a rate of about 3 Pa m^2/s was demonstrated to be pumped out by the pumping system connected to the divertor chamber combined with absorption on the divertor plates. Although the latter effects cannot be expected in steady-state operation since the plates saturate with particles, particle pumping is possible with pumping systems alone provided that the operational density is slightly raised.

3.3. Improved divertor confinement in JT-60

Improvement of both energy and particle confinement was observed in beam heated hydrogen plasmas in JT-60 when the heating power and the line averaged density exceeded thresholds. This regime was termed improved divertor confinement (IDC) [7]. The discharges with improvement of the energy confinement by up to 20% and enhanced divertor radiation lasted for several seconds in a quasi-steady state without significant impurity accumulation in the core. The improvement was observed only when the ion grad-B drift was towards the X-point. The behavior of light impurities and in-out asymmetries in particle recycling changed with reversal of the toroidal magnetic field as shown in Fig. 10. As plotted in Fig. 11, the radiation power from the divertor plasma increased to as much as 50% of the heating power in the IDC regime.

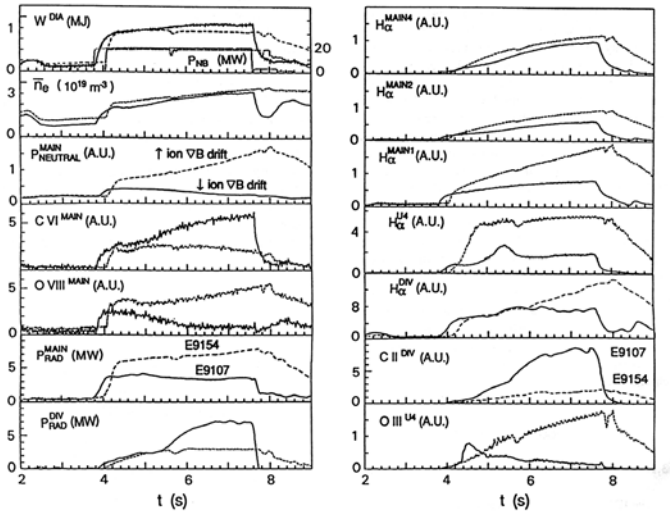

Fig. 10 Comparison of two discharges with nearly identical operational parameters except for the B_t and I_p polarities. The solid and broken lines show traces with the ion grad-B drift towards the X-point and away from it, respectively.

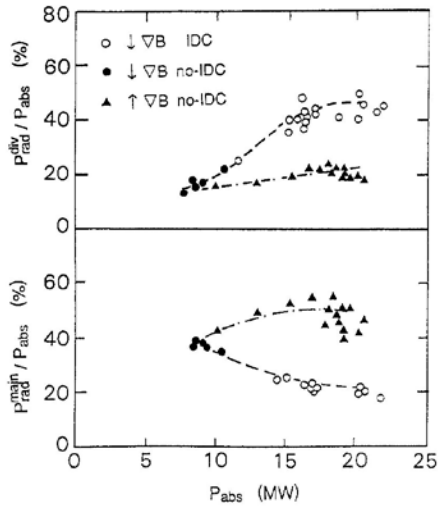

Fig. 11 Changes in radiation power fractions from the main plasma and divertor region with B_t reversal.

The threshold of line averaged electron density for the IDC regime increased linearly with power and dropped with increasing safety factor. These findings are consistent with the theoretical model in which collisional transport near the separatrix is connected with the onset of the IDC regime.

3.3. Field reversal effects on divertor plasmas in JT-60U

Reversal effects of the toroidal magnetic field on the divertor plasma parameters were investigated in detail under radiative and detached divertor conditions in L mode discharges of JT-60U. The ion flux to the inboard separatrix strike point decreased before a MARFE occurred, irrespective of the ion grad-B drift direction. The maximum fraction of power radiated in the divertor was comparable between the two B_t directions. With the power flowing into the two divertor fans being slightly larger on the outboard than on the inboard, a nearly symmetric in-out heat load was observed for the ion grad-B drift away from the target as shown in Fig. 12. This was caused by enhanced asymmetries in the particle flux and radiation loss distributions. From the viewpoint of in-out symmetry in the target heat load and $T_{e,div}$, operation with the ion grad-B drift away from the target plate is desirable as long as the attached divertor condition is maintained. On the contrary, during the MARFE, although deterioration of the energy confinement as well as the increase in the fueling efficiency were comparable, for the ion grad-B drift towards the target the plasma did not detach completely, and the strong in-out asymmetry in the particle recycling was relaxed to a relatively symmetric distribution. From the viewpoint of particle exhaust to the divertor, operation with the ion grad-B drift towards the target is favorable [8].

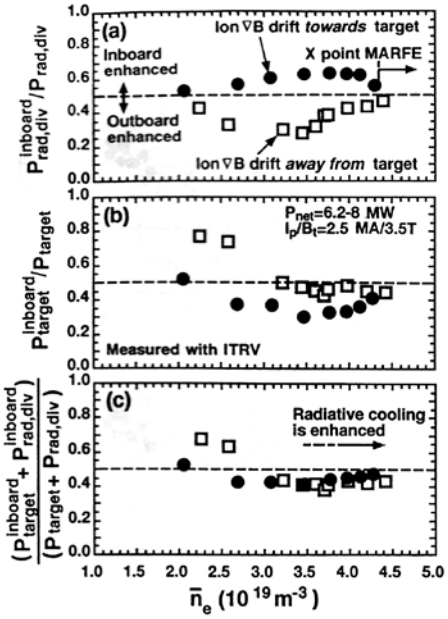

Fig. 12 Fractions of (a) radiation power loss; (b) heat load; and (c) total power loss in the inboard divertor compared with B_t reversal. Radiation losses affect the in-out asymmetry in P_{target} with increasing electron density.

4. Limiter H mode with lower-hybrid current drive

4.1. H mode characteristics

The H mode was achieved in limiter discharges of a tokamak with lower-hybrid current drive (LHCD) for the first time [9]. Simultaneous application of RF powers at two different frequencies such as 1.74 and 2.23 GHz or 1.74 and 2.0 GHz appeared to be effective in the attainment of the H mode. The threshold lower-hybrid power was as low as the Ohmic-heating power with hydrogen plasmas. Typical plasmas had R = 3.04 m, a = 0.89 m, and nearly circular cross section which contacted inner bumper-type limiters. The gap between the outermost flux surface and the outside limiters was about 5 cm. Graphite first walls were conditioned by Taylor-type discharge cleaning. LH power was applied from two launchers located at the outer (low field) side of the torus at an upward angle of 40 deg. from the midplane.

In JT-60, the H mode was obtained in the outer or lower divertor configuration with NBI heating and combined heating with NBI and ICRH or NBI and LH. The threshold heating power was about 16 MW. In contrast to the beam-heated H mode with frequent edge localized modes (ELM) in the divertor configuration, the limiter H mode with LHCD produced ELM-free H phases longer than 3 s. Typical time traces are shown in Fig. 13.

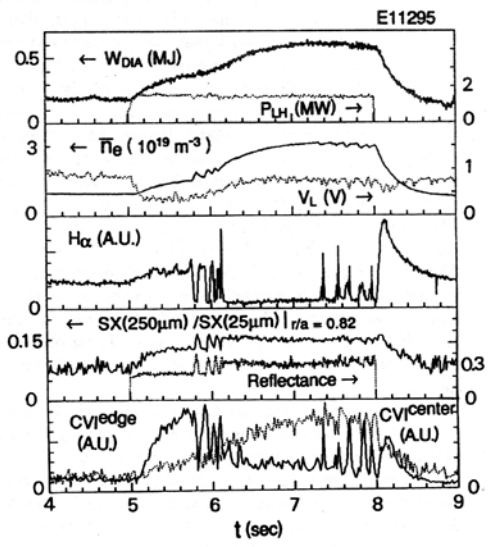

Fig. 13 Time evolution of plasma stored energy evaluated by diamagnetics, injected LH power, line-averaged electron density, one-turn loop voltage, Hα emission, ratio of soft-x-ray signals through Be foils, reflection coefficient of the conventional launcher, and CVI line signals along chords near the edgeand through the center.

The properties of energy confinement are summarized in Fig. 14. The plasma stored energy increases almost linearly with the total input power as shown in Fig. 14(a). Here we assumed that the injected LH power was completely absorbed by the plasma. The scatter of the data points is mainly due to the variation of the electron density. The energy confinement is enhanced by up to 30% by the H mode. The increment in the plasma stored energy,

however, is primarily gained by the increase in the electron density as plotted in Fig. 14(b). The L-mode plasmas with LHCD have almost the same electron density dependence as the Ohmic stored energy indicated by the broken curve presumably because the total input power does not greatly exceed the Ohmic input. Although the difference is small, the H-mode data points appear to have a little stronger n_e dependence than Ohmic.

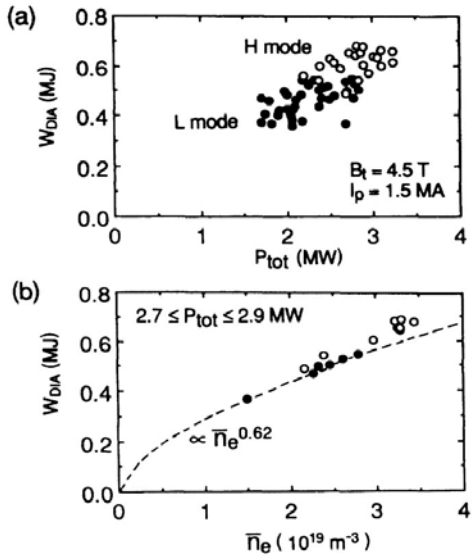

Fig. 14 (a) Plasma stored energy as a function of $P_{tot} = P_{OH} + P_{LH}$. Open and solid circles represent data from the H and L mode, respectively.
(b) Electron-density dependence of plasma stored energy when the total power is restricted.

The threshold power for the limiter H mode with LH is extremely low compared with that under NB heating even in divertor configurations which have an almost linear dependence on B_t as illustrated in Fig. 15. Although the mechanism for the isotopic dependence has not been understood, the power required for H mode in hydrogen plasmas is commonly observed to be higher than that in deuterium ones even in limiter configurations, where H mode transitions with NBI are hard to occur.

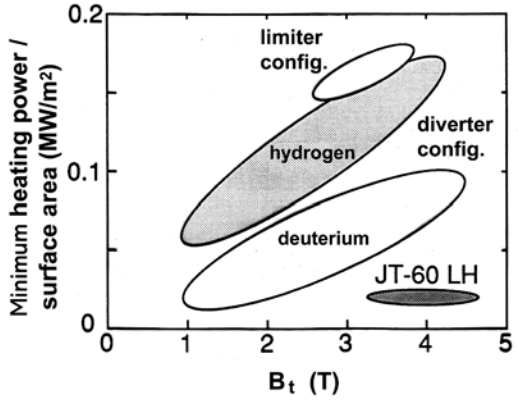

Fig. 15 Threshold heating power for H mode normalized to the plasma surface area in tokamaks as a function of toroidal magnetic field.

Figures 16 and 17 show that a transport barrier is formed near the edge, accompanied by a quench of density fluctuations. Changes of the temperature profile were little in the case of H-mode transition by LHCD [10].

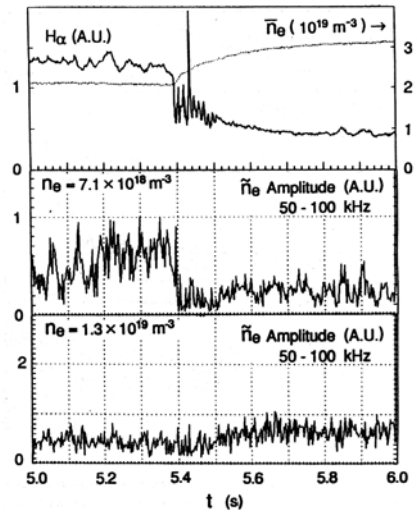

Fig. 16 Reduction in electron density fluctuations near the edge measured by reflectometry during the H mode with LHCD.

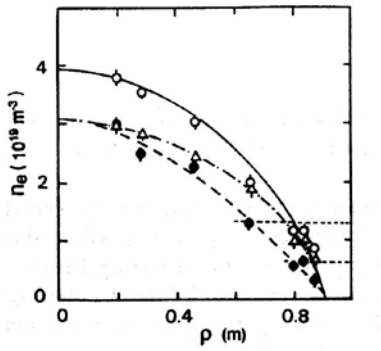

Fig. 17 Electron density profiles from Thomson scattering during the L mode (closed circles) and H mode (open circles). Triangles represent the n_e profile at 6.5 s of the shot shown with Fig. 13. Horizontal dotted lines indicate the location of the reflectometry measurement layers.

4.2. Presence of fast electrons for H mode

. Figure 18 shows an example shot where an H phase with LHCD was destroyed by NB injection. The trace of the electron cyclotron emission at 1.5 ω_{ce} multiplied by n_e, which is a measure of LH coupling to fast electrons, dropped at the L-mode transition. The hard X-ray emission measured with a 3-channel array viewing the plasma perpendicularly to the magnetic field as shown in Fig. 19 also dropped at the L-mode transition. The time resolution of the hard X-ray data is 0.2 s since they were recorded with pulse height analysers. The traces represent the time evolution of the total photon counts in the energy range from 70 keV to 1 MeV.

During the L phase with NBI, beam acceleration by the LH waves was observed in the neutral spectra shown in Fig.

20 beyond the injection energy at 65 keV. These facts suggest that the H mode could not be sustained when the LH power was absorbed by the beam ions.

The hard X-ray spectra were different depending on the frequency combination. Open and closed symbols in Fig. 21 show the distinction on the hard X-ray intensity during the L-mode phases which led to the H mode from those which remained in the L mode, respectively. The broken line indicates that the threshold intensity drops with increasing photon temperature. The effectiveness of applying LH power at two different frequencies may be explained by the effective generation of suprathermal electrons (> 100 keV). The reason why no H mode with LH has ever been obtained in divertor configurations may be explained by the fact that there are much more peaked hard X-ray profiles than in limiter discharges. Considering that the current drive efficiency is higher in divertor discharges, LH power may drive fast electrons more inside than the case in limiter discharges.

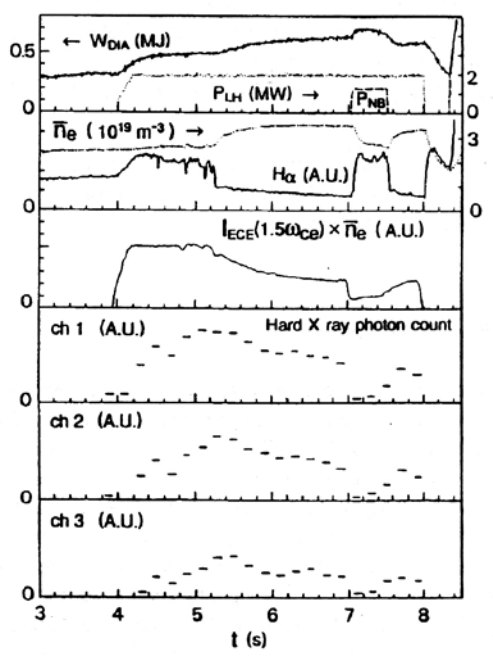

Fig. 18 Time evolution of a discharge where the H mode with LHCD was destroyed by NBI.

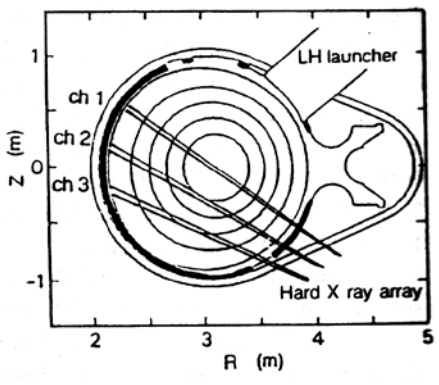

Fig. 19 Limiter plasma configuration for LHCD and three chords of hard X-ray diagnostics.

The H mode in tokamaks is theoretically interpretated as the bifurcation of the radial electric field at the plasma edge [11]. The electric field is determined by the balance of the non-ambipolar fluxes of ions and electrons at the edge. There was a controversy concerning whether the polarity of the radial electric field is a key to the H mode or not. The ion loss in the loss cone generates radially inward electric field in beam heated plasmas. In contrast, the loss of fast electrons causes outward electric field. Hence, the H mode with LHCD provided an evidence to settle the argument.

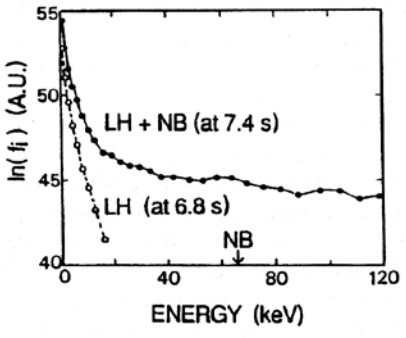

Fig. 20 Beam acceleration observe in neutral particle spectrum (closed circles) and no ion tail with LHCD alone.

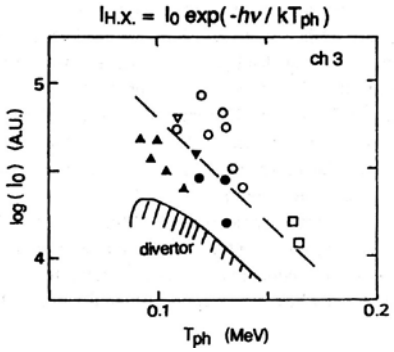

Fig. 21 Fitted photon temperature of hard X ray under LHCD with four frequency combinations; ○: (1.74 + 2.23), □: (1.74 + 2.00), △: (2.00 + 2.00) and ▽: (2.00 + 2.23) GHz. Open symbols indicate that the H mode was triggered.

References

1. S. Tsuji *et al*.; JAERI-M 91-196 (1991). (in Japanese)
2. M. Kikuchi, O. Naito, H. Yoshida, S. Tsuji, N. Hosogane; Kakuyugo Kenkyu Vol. **65**/Supplement, pp. 51-73 (1991).
3. S. Tsuji *et al*.; JAERI-M 90-066, pp. 152-155 (1990).
4. Shunji Tsuji; *Fusion Eng. Des*. **15** [4], 311-324 (1992).
5. K. Yamada, S. Tsuji, K. Shimizu, T. Nishitani, K. Nagashima, the JT-60 TEAM; *Nucl. Fusion* **27** [8], pp. 1203-1211 (1987).
6. H. Nakamura *et al*.; *Nucl. Fusion* **28**, pp. 43-52 (1988).
7. S. Tsuji *et al*.; *Nucl. Fusion* **32** [8], 1313-1330 (1992).
8. N. Asakura, K. Shimizu, N. Hosogane, K. Itami, S. Tsuji, M. Shimada; *Nucl. Fusion* **35** [4], 381-398 (1995).
9. S. Tsuji *et al*.; *Phys. Rev. Lett.* **64** [9], 1023-1026 (1990).
10. S. Tsuji *et al*.; *Proc. 13th Int. Conf. on Plasma Phys. Controll. Nucl. Fusion Res. 1990*, Vol. **1**, 659-668 (1991).
11. S.-I. Itoh, K. Itoh; *Nucl. Fusion* **29** [6], pp. 1031-1045 (1989).

II. Research Reports

A. Innovative Nuclear Energy System Division

A.1 Study on Innovative Nuclear Reactor Designs and Criticality Safety in Fukushima Daiichi NPS Decommissioning

Toru Obara

Studies on innovative nuclear reactor designs and criticality safety in Fukushima Daiichi Nuclear Power Station (NPS) decommissioning have been performed. The studies were focused on the stational wave Breed-and-Burn (B&B) reactors, CANDLE burning reactors, time-dependent criticality analysis during fuel debris falling down in water, and space dependent kinetic analysis method.

1. Study on stationary wave Breed-and-Burn reactor

The B&B reactor is once-through fuel cycle fast reactor. In the reactor, fertile material is converted into fissile material by neutron irradiation. The produced fissile material is consumed in the reactor. It dose not require reprocessing facility and is possible to achieve high utilization of natural uranium resources. In the previous study, the rotational fuel-shuffling scheme was proposed. In this study, a spiral fuel-shuffling scheme was proposed to establish an advantageous neutron-economy B&B operation mode, in which high-reactivity fuels are placed stably in a region of high neutron importance. To reduce the maximum displacements per atom (dpa) value without a fuel reconditioning process, B&B operation mode with smaller burnup core was also considered as a requirement. In this shuffling scheme, fresh fuel assemblies composed of natural uranium are loaded from the core periphery and moved toward the center along a spiral path, then discharged from the core center (**Figure 1**). Calculation results found that the core with spiral fuel shuffling achieved an equilibrium state at criticality [1].

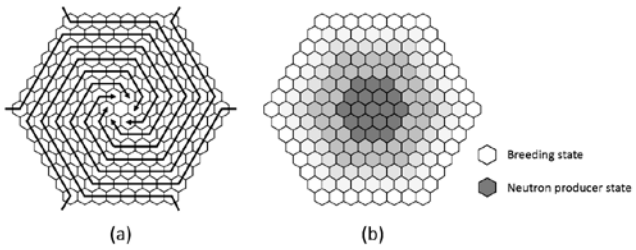

Figure 1. (a) Schematic diagram of spiral fuel shuffling; (b) The states in the core [1]

2. Study on CANDLE burning fast reactor

CANDLE burning reactor is one of the B&B fast reactor concepts. One of the issues to be solved in the concept is to establish a measure against irradiation damage of fuel cladding in high burnup. In the study, a melt-refining process was applied to the transition state of a CANDLE burning fast reactor in order to solve the fuel integrity problem at high burnup condition. The melt-refining process was applied before cladding damage exceeded 200 dpa of criteria. In the analysis, the effect of cooling, homogenization, FP removal, mass loss, and waiting were considered. The CANDLE burning analysis including the effect showed that the reactor was able to maintain criticality during the transition period. It was shown that the melt-refining process was able to solve the cladding damage problem and improve nuclear resource usability [2].

3. Criticality simulation of fuel debris falling in water

In the decommissioning process of Fukushima-Daiich NPS, the fuel debris removal is one of the important process. In the removal, the solid fuel debris must be bitten into small fragments. One of the possibilities of the accident is the fragmented fuel debris fall down in to water. It can be a possibility of criticality accidents during debris removal. Hence, accurate evaluations of criticality that consider the dynamic behavior of fuel debris in water are an essential part of the decommissioning process. In this study, a calculation system that combines the moving particle semi-implicit method and Monte Carlo neutron transport calculation code was developed. It is possible to evaluate criticality using the actual dynamic behavior of fuel debris in water. Some numerical simulations of fuel debris falling in water were performed after he validation of numerical simulation with experiments (**Figure 2**). It

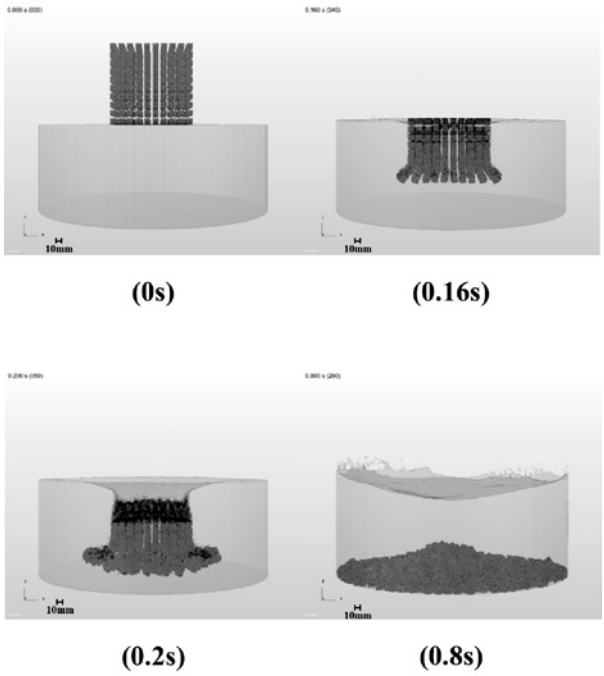

Figure 2. Snapshots of simulation of fuel debris falling down in water [3]

can also evaluate criticality during the sedimentation of cubic fuel debris. Moreover, in the case of fundamental conditions such as a large amount of cubic debris falling in water, it is possible to analyze that the effective multiplication factor can be maximized in the state of falling in water rather than with complete sedimentation [3].

4. Development space-dependent supercritical analysis method

It is important to establish measures for the safety in fuel debris removal. To evaluate fission energy in the case of criticality accidents is one of the key issues for that. The accident can be happened when the fuel debris are in water. In the case, the geometry of critical system can be very complicated. It is needed to perform space dependent kinetic analysis based on the neutron transport theory. Multiregion integral kinetic (MIK) code based on the integral kinetic model and a Monte Carlo neutron transport method has been developed with a new time-dependent feedback modeling capability. The current MIK code is applicable to the supercritical power transient following reactivity insertion in a fissile system of arbitrary geometry and composition, taking its feedback mechanisms into account. The new time-dependent feedback modeling capability allows a more direct and accurate treatment of complicated and nonlinear feedback mechanisms in a given system [4].

Reference

1. Kazuki Kuwagaki, Jun Nishiyama, and Toru Obara: Concept of breed and burn reactor with spiral fuel shuffling; *Annals of Nuclear Energy*, Vol **127**, pp. 130-138 (2019).
2. Hiroki Osato, Jun Nishiyama, Toru Obara: Application of Melt-refining Process to Transition State of CANDLE Burning Fast Reactor", *Annals of Nuclear Energy*, Vol. **128**, pp. 77-83 (2019).
3. Takeshi Muramoto, Jun Nishiyama, Toru Obara: Numerical analysis of criticality of fuel debris falling in water", *Annals of Nuclear Energy*; Vol. **131**, pp. 112-122 (2019).
4. Delgersaikhan Tuya, Toru Obara: Development of Monte Carlo Neutron Transport Method-Based Supercritical Transient Code with Time-Dependent Feedback Capability; *Nuclear Science and Engineering*, Vol. **193**, pp. 481-494 (2019).

A.2 High-Temperature Thermochemical Energy Storage using Calcium Hydroxide and Porous Ceramic Composite

Yukitaka Kato, Shigehiko Funayama, Hiroki Takasu

1. INTRODUCTION

An increase in the demand and utilization of primary energy requires the promotion of renewable energy sources, and an improvement in energy efficiency. Thermal energy storage can contribute to the cost-effective deployment of the gigawatt-hours scale storage of thermal energy or electricity generated intermittently by renewables, e.g. concentrated solar power (CSP) and wind power. Thermal energy storage is also an important technology in waste heat recovery, which can improve the energy efficiency of thermal processes. There are several types of thermal energy storage: sensible heat storage, latent heat storage, and thermochemical energy storage.

Thermochemical energy storage uses reversible gas-solid reactions to store thermal energy in the form of chemical energy. This system has a higher energy density than other types of thermal energy storage and has longer-term storage capability. As a reaction system for the thermochemical energy storage, a calcium oxide/water/calcium hydroxide ($CaO/H_2O/Ca(OH)_2$) reaction system has received intense attention from researchers because of its high reactivity, the low cost and environmentally friendly reaction materials. The gas-solid reaction the system uses is described in Eq. (1):

$$Ca(OH)_2(s) \rightleftharpoons CaO(s) + H_2O(g); \quad \Delta H_r = 104 \text{ kJ mol}^{-1} \quad (1)$$

The forward endothermic reaction is known as dehydration and the reverse exothermic reaction is hydration. The heat absorbed during dehydration is stored, with the energy storage density of 1.4 MJ/kg-$Ca(OH)_2$, as long as the calcium oxide and the water are separated from each other. The heat output occurs during hydration. A thermochemical energy storage system based on the $CaO/H_2O/Ca(OH)_2$ reaction, can be utilized at high temperatures with operating temperatures between 400 °C and 600 °C, depending on the water vapor pressure.

The reaction system has been studied experimentally by other researchers for thermal applications such as thermal energy storage systems in CSP plants, chemical heat pumps, waste heat recovery, and the reactivation of CaO materials as sorbents for CO_2 capture.

Practical packed bed reactors require fast thermal responses during the heat storage/output process and the durability for repetitive operations. In terms of the $CaO/H_2O/Ca(OH)_2$ reaction system, previous studies using laboratory-scale packed bed reactors have reported several problems of pure $CaO/Ca(OH)_2$ materials that need to be solved in order to meet the requirements: low thermal conductivity of the powder beds, the formation of centimeter-scale agglomerates inside the reactors and the change in the bulk volume during repetitive reactions. Therefore, the need to develop suitable materials for the $CaO/H_2O/Ca(OH)_2$ reaction system remains.

In the literature, previous studies employed ceramic honeycombs and foams for redox reaction systems. Kariya *et al*. focused on a composite material using a silicon carbide honeycomb for the $CaO/H_2O/Ca(OH)_2$ system [1]. However, a very few studies have focused on a composite material using a ceramic foam for thermochemical energy storage based on the $CaO/H_2O/Ca(OH)_2$ reaction system. This use of a ceramic foam is expected to facilitate solving the problems described previously.

The objectives of this study were to develop a novel composite material using a silicon-silicon carbide (SiSiC) ceramic foam support for the $CaO/H_2O/Ca(OH)_2$ reaction system, and to investigate whether the foam support enhance the heat transfer in a packed bed reactor and the cycle durability of the composite.

2. Composite material and experimental apparatus

2.1 Materials

Calcium hydroxide pellets ($Ca(OH)_2$ >99.9%, reagent grade) were used to provide the powdered $Ca(OH)_2$ for the preparation of the composite material.

The silicon-silicon carbide (SiSiC) ceramic foam used is shown in **Fig. 1** (a) (AIRSIC® PD 0.4, NGK Insulators, Ltd., Japan). **Fig. 1** (b) shows a scanning electron microscope (SM-200, Topcon, Japan) image of the surface of the ceramic foam. According to the datasheet provided by the company, the ceramic foams were composed of 58% silicon carbide and 42% silicon. The porosity was 92%, the average pore size was 400 μm and the flexural strength was 1 MPa. A cylindrical ceramic foam (mean diameter: 45 mm, height: 52 mm) consisting of disk-shapes cut into quarters, was used for the packed bed reactor experiment.

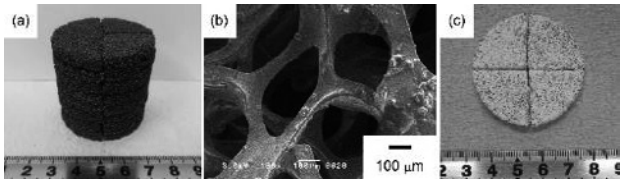

Fig. 1 SiSiC foam support and composite material: (a) the ceramic foam support; (b) reticulate structure of the foam; (c) the composite material combining the foam with calcium hydroxide.[2]

A composite material was prepared using a vacuum impregnation method in which a $Ca(OH)_2$ sample was

embedded inside the SiSiC foam support. A calcium hydroxide powder was prepared by crushing the pure pellets with a mortar and pestle. The powdered calcium hydroxide was dispersed in a 20% mixture of ethanol in deionized water. The solid content concentration of the prepared slurry was 61 wt%. The SiSiC foam support was desiccated under vacuum for at least 15 min. The foam sample was then impregnated by pouring the calcium hydroxide slurry into the foam support in the desiccator and kept under vacuum for another hour. The sample was dried at 120 °C for more than 12 hours. In order to make the volume of the composite the same as the SiSiC foam support, surplus deposits of $Ca(OH)_2$ on the surface of the samples were removed.

2.2 Experimental Apparatus

Packed bed experimental apparatus for composite material reactivity demonstration is shown in **Fig. 2**. Seven thermocouples (1.0 mm diameter, K-type) were used to measure the bed temperatures during the dehydration and hydration reactions. The target temperature at T_4 was preset on a temperature controller, then regulated and maintained using a 500 W sheath heater coiled around the reactor wall. The packed bed reactor was enveloped by reflectors to enhance the thermal insulation. Apertures located on the reflectors and the cover allowed water vapor to flow in and out of the reactor.

The packed bed reactor was installed inside of the reaction chamber that was connected to the water reservoir. In the reservoir, the water vapor was condensed (dehydration reaction) and generated (hydration reaction) during the experiment. The external surfaces of the reaction chamber and the connecting pipes between the chamber and reservoir were kept at a constant temperature (over 120 °C) by heaters and insulators to prevent condensation. The pressure in the system was measured by two pressure gauges (±0.2 kPa, PA-750-302R, Nidec Copal Electronics, Japan) denoted as P_1 and P_2 in **Fig. 2**. The mass change of the reaction chamber during the dehydration and hydration experiments was measured by an electronic balance (± 0.1 g, MS16001L/02, Mettler Toledo, U.S.).

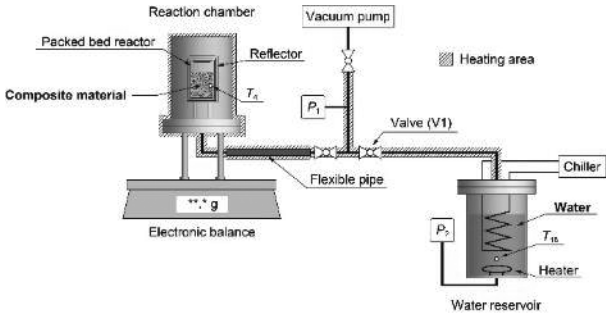

Fig. 2 Schematic diagram of experimental apparatus [3].

3. Experimental results and discussion

The heat output rates per unit volume of the composite bed under different hydration pressures are shown in **Fig. 3**. The heat output rate was enhanced by increasing hydration pressure.

The heat output rates per unit volume for 5 min under different hydration pressures are shown in Fig. 10. The heat output rate of the bed of the composite under 85 kPa was 1.3 kW L-bed^{-1}, which was 1.4 times higher than that of the pure pellet bed, which indicated that the heat transfer through the reaction bed was enhanced. The composite bed showed comparable heat output rates to that of the pure pellet bed with pressures of 39 and 58 kPa, and the heat output rates of the pure pellet bed exceeded the rates of the composite bed at 16 and 25 kPa. Further study should focus on heat transfer enhancement in the composite bed at higher hydration pressures, where the reaction rate is large enough and the heat transfer inside the bed can be the rate-determining process for the heat output process.

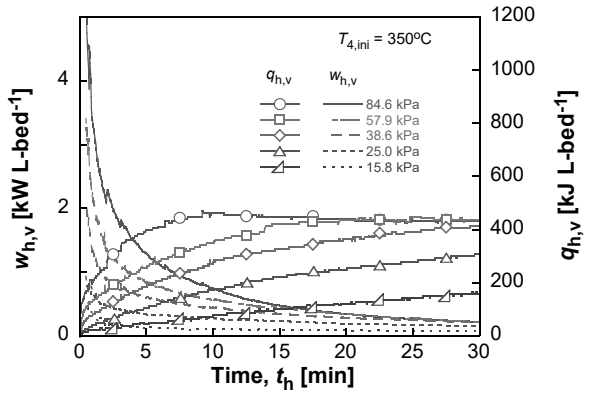

Fig. 3 Heat output rate, $w_{h,v}$, and heat output density, $q_{h,v}$, per unit volume of the beds of the composite (ASCH0.65) under a series of hydration pressures [2].

4. Conclusions

A novel composite material using calcium hydroxide and SiSiC ceramic foam support to overcome the limitations of pure $CaO/Ca(OH)_2$ powder or pellet beds reported in previous studies, such as: low thermal conductivity, the formation of centimeter-scale agglomerates and a change in the bulk volume. To evaluate the performance of the developed composite at a laboratory scale, a packed bed reactor was used. The storage energy density of the composite per unit volume and per unit mass was 440 kJ L-bed^{-1} and 550 kJ kg-material^{-1}, respectively. The heat output rate per unit volume of the bed for the first 5 min under a hydration pressure of 85 kPa was 1.3 kW L-bed^{-1}, which was 1.4 times higher than that of the bed of pure calcium hydroxide pellets studied previously, even though the heat storage density of the composite was only 43% of that of the pure pellet bed. This result suggested that the heat transfer through the packed bed was enhanced by the SiSiC foam support. The cycle stability and high reactivity of the composite during 10-cycle reactions were also confirmed. It was observed that the calcium hydroxide sample was kept subdivided inside the pores of the foam support and the bulk volume was remained. These results demonstrated that the developed composite has a high durability and scalability. The composite material was shown to be a practical material for high-temperature thermochemical energy storage.

References

1. J. Kariya, Y. Kato, "Development of thermal energy storage material using porous silicon carbide and calcium hydroxide", Energy Procedia 2017;131:395–406.
2. S. Funayama, H. Takasu, M. Zamengo, J.Kariya, Y. Kato, "Composite Material for High-Temperature Thermochemical Energy Storage using Calcium Hydroxide and Ceramic Foam", *Energy Storage*, pp. 1-12, 2019;1:e53.
3. S. Funayama, H. Takasu, M. Zamengo, J. Kariya, S. T. Kim, Y. Kato, "Performance of thermochemical energy storage of a packed bed of calcium hydroxide pellets", *Energy Storage,* pp. 1-11, 2019;e40.

A.3 Thermodynamic investigation on cesium oxide binary systems by chemical equilibrium techniques

Yoshinao Kobayashi

1. Introduction

After the severe accident of Fukushima Daiichi Nuclear Power Station (FDNPS), the release of radioactive materials to the environment due to the cladding failure and core meltdown is caused serious problem in Japan. Under high temperature environment and oxidation atmosphere, fission product cesium was formed several binary systems inside reactor. Such as Cs_2O-SiO_2[1] and Cs_2O-B_2O_3[2] binary system. Based on the findings regarding Cs-bearing particle by some researchers, the particles are mainly composed of silicate (SiO2) as major component as well as radioactive Cs in the form of oxide (Cs_2O). According to this knowledge, chemical properties of this radioactive particle should be clarified to elucidate the formation mechanism of how this particle could be formed. For the Cs_2O-B_2O_3 binary system, it was formed by fission product cesium oxide and control rod degradation product boron oxide. During the decommissioning of FDNPS, it is important to make clear that the distribution of cesium inside reactor. Thermodynamic properties such as activity and activity coefficient are necessary to solve this problem and thermodynamic characterization by chemical equilibrium technique has been employed to derive the thermodynamic properties of each components in Cs_2O-SiO_2 and Cs_2O-B_2O_3 binary system.

2. Experimental

2.1 Chemical Equilibrium Technique

An electric resistance furnace made by helical silicon carbide heating element is used for the high-temperature experiments. The maximum temperature of this furnace about 1600℃. An alumina reaction tube was positioned inside the furnace as furnace tube. The furnace was equipped with a proportional-integral-differential (PID) controller with a Pt/Pt-6%Rh thermocouple for controlling the furnace temperature. The temperature difference across the height of the melt was not more than 2°C.The powders were weighted by digital balance and mixed by pestle and porcelain mortal. Then put mixed powder in a graphite crucible with reference metal shot. A high flow rate o¥f argon gas was used for flushing out air from the electric furnace about 15mins. Then the graphite crucible was placed in the hot zone of the furnace and equilibrated under carbon monoxide atmosphere. The cesium carbonate powder will decomposition under high temperature (more than 600°C) to form cesium oxide. It will react with boron oxide powder. Their liquid phases will infiltrate into the reference metal. Graphite crucible and carbon monoxide gas will control the partial pressure of oxygen in the furnace. After keeping the sample in the furnace for a given period, it was quenched by withdrawing from the furnace and flushing with argon gas on a copper plate to cool it down. Those reference metal shots were melted and become on metal grain. The metal sample was polished by a micro grinder to remove the oxide layer, then cut into small pieces (about 0.1g). These small pieces were dissolved by nitric acid for elemental analysis.

2.2 Chemical Analysis

For Cs_2O-SiO_2 binary system, we use ICP-OES as the elemental analysis method to measure silicon and copper concentration in copper sample. Copper sample obtained from the chemical equilibrium experiment was separated from the slag and was ground to remove the oxide on the surface and cut into 0.1 g. To analyze Si in copper sample, firstly, 0.1 g copper sample was dissolved by 10 ml nitric acid (1.5 M) at around 95oC for several hours until solid copper fully dissolved into blue liquid ($Cu(NO_3)_2$)[3]. Then, 1 ml of liquid copper and 9 ml of 2 M NaOH was heated at high temperature (~200oC) by magnetic stirrer hotplate for around 1 h[4]. During the reaction, the solution was stirred to prevent the evaporation of liquid sodium silicate. Black colored CuO solid will be formed by this reaction. Liquid was separated from solid by filtering using filter paper. One milliliter of liquid then diluted 10 times by adding distilled water and subjected to be analyzed by ICP-OES. Standard solution containing 1.5 ppm and 6 ppm as well as blank solution were prepared to perform quantitative analysis. To analyze copper concentration, $Cu(NO_3)_2$ solution was used and diluted 100 times by adding distilled water and subjected to be analyzed by ICP-OES. Standard solution containing 100 ppm and 200 ppm as well as blank solution were prepared to perform quantitative analysis.

For Cs2O-B2O3 binary system, we use ICP-MS as the primary elemental analysis method to measure cesium concentration in the reference metal samples. After cutting the metal sample to 0.1gram small piece, it will be dissolved in 10mL nitric acid solution (32wt%). Because the cesium concentration in the metal sample is very low, we assume that all the solutes of this solution is reference metal. The metal concentration in this solution is about 10,000 ppm. According to the ICP-MS instrument sample pass upper limit (about 10ppm). We need to dilute the sample solution 1000x.

3. Result and Conclusion

3.1 Determination of Equilibrium Time and Cesium Molar Fraction in Equilibrium State.

The most important part of high-temperature equilibrium experiment is to make sure that the experimental system reaches the equilibrium state. The experimental system reaches the equilibrium state when reactant concentration shows no significant change. Here we use cesium concentration as a maker, and the cesium molar fraction in equilibrium state will be used for calculating the

thermodynamic activity of cesium oxide. Table 1 shown the cesium molar fraction of different holding time in 1150 and 1250℃. The cesium molar fraction was derived by analyzing cesium and reference metal concentration. From these results, we can conclude that after holding on high temperature for 48 hours, the experimental system becomes an equilibrium state. The cesium molar fraction at equilibrium state are about 0.00013 in 1150℃ and 0.000118 in 1250℃.

Table 1. Cesium molar fraction change with the holding time

No.	Temperature/℃	Holding Time/h	Reference Metal	Cesium Molar Fraction
1	1150	24	Ag	0.0001091
2		48	Ag	0.0001305
3		72	Ag	0.0001290
4	1250	24	Cu	0.0000821
5		36	Cu	0.0001105
6		48	Cu	0.0001183
7		60	Cu	0.0001009
8		72	Cu	0.0000982

3.2 Activity and Activity Coefficient of Components in Binary Alkali System

The activity and activity coefficient of cesium oxide and boron oxide in the Cs_2O-B_2O_3 binary system was derived by thermodynamic calculation and Gibbs-Duhem equation. Results shown in Table 2.

Table 2 Thermodynamic functions of different compositions in Cs_2O-B_2O_3 system

Temp/℃	X_{Cs_2O}	$X_{B_2O_3}$	a_{Cs_2O}	$a_{B_2O_3}$	γ_{Cs_2O}	$\gamma_{B_2O_3}$
1150	1.0	0	1.000	0	1	/
	0.9	0.1	0.931	0.018	1.035	0.184
	0.8	0.2	0.805	0.037	1.006	0.183
	0.7	0.3	0.674	0.055	0.963	0.183
	0.6	0.4	0.544	0.075	0.906	0.187
	0.5	0.5	0.381	0.100	0.761	0.199
	0.4	0.6	0.313	0.136	0.784	0.226
	0.3	0.7	0.239	0.194	0.796	0.278
1250	1.0	0	1.000	0	1	/
	0.9	0.1	0.945	0.013	1.050	0.132
	0.8	0.2	0.678	0.026	0.847	0.131
	0.7	0.3	0.575	0.040	0.821	0.132
	0.6	0.4	0.513	0.055	0.856	0.137
	0.5	0.5	0.408	0.074	0.816	0.149
	0.4	0.6	0.363	0.104	0.906	0.174
	0.3	0.7	0.305	0.156	1.017	0.223

From the cesium oxide activity result, the activity curve of cesium oxide in binary system at 1150 and 1250℃ were shown in Figs. 1 and 2. The activity curves in both temperatures show negative deviation from ideal solution, it indicates the strong affinity between cesium oxide and boron oxide in this binary system. From experimental result, activity coefficient of Si in liquid copper at 1350℃ is 0.006.

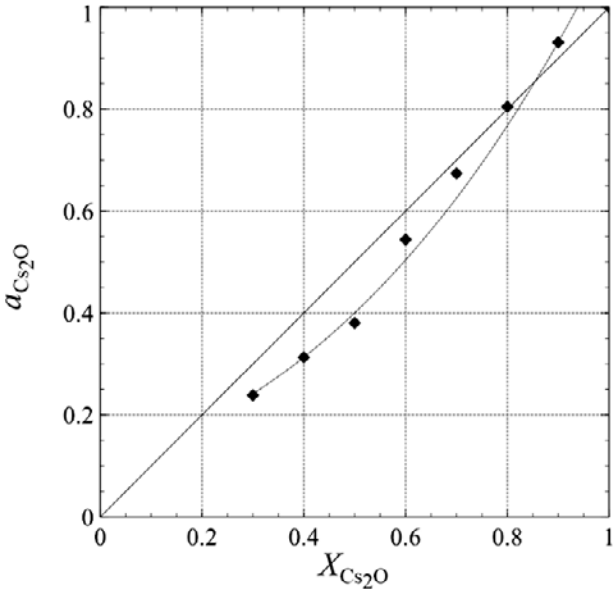

Figure 1. a_{Cs_2O} in Cs_2O-B_2O_3 binary system in 1150℃

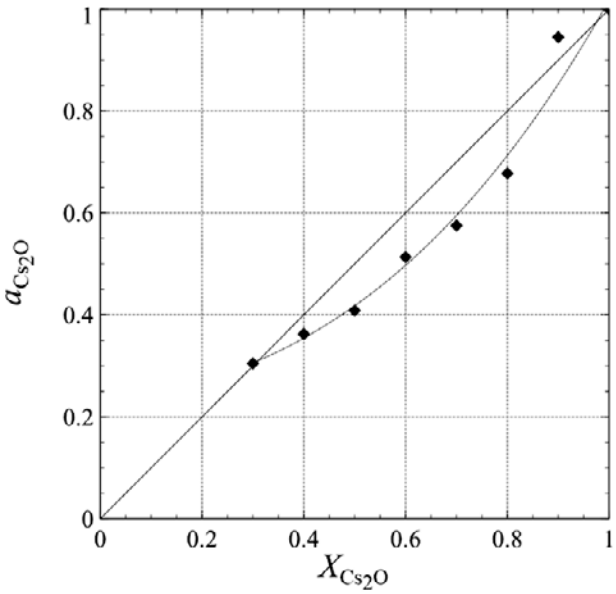

Figure 2. a_{Cs_2O} in Cs_2O-B_2O_3 binary system in 1150℃

The result of □Si in this present study shows quite good agreement with the value reported by Kato et.al.[5], which is 0.0071, while Kato et al. determined the □Si by using Cu-Si-Fe alloy with SiO_2 pellet to make the activity of SiO_2 to be unity, but in present study the composition with SiO_2 saturated phase (95% SiO_2-5%Cs_2O) is used to make the activity of SiO_2 to be unity. From the SiO_2 activity data in Table 3, activity curve of SiO_2 could be established. Activity curve of SiO_2 is established with abscissa is molar fraction of SiO_2 and ordinate is activity of SiO_2. The curve shows negative deviation from ideal solution, which means the strong affinity between SiO_2 and Cs_2O in this system.

3.3 Enthalpy Change of Mixing and Partial Molar Enthalpy of SiO_2 in Binary Alkali System

The enthalpy of mixing change between two

compositions (SiO_2 and Cs_2O; B_2O_3 and Cs_2O) can be determined by using following equation:

$$\Delta H_{mix} = \sum x_i \overline{\Delta H_i} = X_{Cs_2O}\overline{\Delta H_{Cs_2O}} + X_{B_2O_3}\overline{\Delta H_{B_2O_3}} \quad (17)$$

$$\Delta H_{mix} = \sum x_i \overline{\Delta H_i} = X_{Cs_2O}\overline{\Delta H_{Cs_2O}} + X_{SiO_2}\overline{\Delta H_{SiO_2}} \quad (18)$$

Table 4 shows the value of enthalpy change of mixing with Cs_2O compositions at 1150 and 1250℃. From the results shown in table 5, all value of enthalpy change of mixing is negative. When the enthalpy of mixing is negative, mixing is signifying exothermic mixing.

Table 4. Enthalpy change of mixing in the Cs_2O-B_2O_3 at 1150 and 1250℃

Cesium oxide molar fraction	Enthalpy change of mixing(kJ/mol)	
	1150℃	1250℃
0.9	-16.36	-20.08
0.8	-39.62	-68.29
0.7	-63.40	-94.40
0.6	-86.35	-112.49
0.5	-111.66	-133.41
0.4	-117.09	-137.85
0.3	-114.11	-132.36

Acknowledgment

xaThis study is financially supported by the project of "Thermodynamic characterization of fuel debris and fission products in Fukushima Daiichi Nuclear Power Plant" launched in the plat form of OECD-NEA

Reference

1. Takehiro Sumita, Kentaro Urata, Yuya Morita, Yoshinao Kobayashi: Dissolution behavior of core structure materials by molten corium in boiling water reactor plants during severe accidents; *Journal of Nuclear Science and Technology*, Vol. **55**, pp. 267-275(2018).

Reference

[1] Adachi K, Kajino M, Zaizen Y, et al. Emission of spherical cesium-bearing particles from an early stage of the Fukushima nuclear accident. Sci. Rep. 2013;3:12–15.

[2] Pshenichnikov A, Yamazaki S, Bottomley D, et al. Features of a control blade degradation observed in situ during severe accident conditions in boiling water reactors. J. Nucl. Sci. Technol. [Internet]. 2019;56:440–453. Available from: https://doi.org/10.1080/00223131.2019.1592724.

[3] ELMER TH, NORDBERG ME. Solubility of Silica in Nitric Acid Solutions. J. Am. Ceram. Soc. 1958;

[4] Shi Y, Broome C, Collins R. Determination of radiogenic silicon and its isotopes in neutron irradiated aluminum alloys by ICP-MS. J. Anal. At. Spectrom. 2016.

[5] Kato Y, Yoshikawa T, Kagawa Y, et al. Effect of Fe addition on the activity coefficient of Si in Cu-Fe-Si melt at 1 623 K. ISIJ Int. 2013;

A.4 Improvement of Velocity Vector Measurement System with UVP

Hiroshige Kikura and Hideharu Takahashi

1. Introduction

Recently, an ultrasonic velocity profiler (UVP) is utilized on various flow, e.g. industrial piping flows, flows in food processing and two-phase (three-phase) flows. In our research group, the UVP method has been applied to Fukushima-daiichi nuclear power plant to detect a leakage point of contaminated water. the UVP method, however, has a measurable velocity limit; it is limited to utilize the UVP depending on flow conditions. Therefore, an extension of the measurable velocity limit in the UVP is contribute for a diffusion and a development of the UVP. We developed a velocity limit extension method, wideband phase difference method (WPD), as a novel flow velocity estimation method [1-2].

2. Development of Measurement System

2.1. Detectable Velocity Limit in UVP

An ultrasonic velocity profiler (UVP) can measure instantaneous velocity profiles by detecting Doppler frequencies on an ultrasonic beam path. To detect the Doppler frequency, the UVP method uses the pulse repetition method. The velocity information can be obtained from following equation.

$$v = \frac{f_{PRF}\, c}{4\pi f_c \sin\alpha}\cdot\Delta\theta\,, \tag{1}$$

where c is the speed of sound in the medium, f_c is the ultrasonic basic frequency, and f_{PRF} is the pulse repetition frequency. The phase shift, $\Delta\theta$, is limited from $-\pi$ to π by Nyquist theorem. Thus, the maximum measurable velocity along the flow direction, v_{limit}, is expressed as

$$v_{limit} = \frac{f_{PRF}\, c}{4 f_c \sin\alpha}\,. \tag{2}$$

Therefore, a velocity aliasing is occurred when velocities over the v_{limit}.

2.2. Wideband Phase Difference Method

To measure higher velocities, the wideband phase difference method (WPD) was developed as a de-aliasing method. This method employs the phase difference pattern within the signal bandwidth to modify the phase folding by the Nyquist theorem. Here, we consider the consecutive two echo signals, $f_1(t)$ and $f_2(t)$, from the reflector. The second echo signal, $f_2(t)$, can be expressed as $f_2(t) = f_1(t + \Delta t)$ due to the Doppler shift. Furthermore, the Fourier transforms of each echo signal are expressed as $F_1(\omega)$ and $F_2(\omega)$, respectively. $F_2(\omega)$ can be expressed as following equation using the relationship of $f_2(t) = f_1(t + \Delta t)$.

$$F_2(\omega) = e^{j\omega\Delta t}\cdot F_1(\omega). \tag{3}$$

Namely, the time shift of the echo signal in the time domain reflect to the phase shift in the frequency domain. The phase difference, $\Delta\theta(\omega)$, between the two echo signals is expressed as

$$\Delta\theta(\omega) = \arg.\left[F_2(\omega)\cdot F_1^{*}(\omega)\right] = \omega\Delta t \tag{4}$$

where the mark of * means the complex conjugate. As Eq. (4), the phase differences in the frequency domain are proportional to ω with Δt as a coefficient. The gradient coefficient, Δt, is preserved even if the aliasing is occurred. Therefore, we can get a higher velocity information from a phase difference pattern within the signal bandwidth.

3. Demonstration of WPD Method

To verify the performance of WPD method, a piping flow measurement was carried out. Figure 1 shows the results of velocity profiler measurement in the horizontal pipe by WPD method. The velocity profiles over the conventional v_{limit} were obtained. In addition, water leakage detection was conducted with the WPD and phased array sensor for the application. Figure 2 shows the results of the velocity vector measurement around the simulated water leakage.

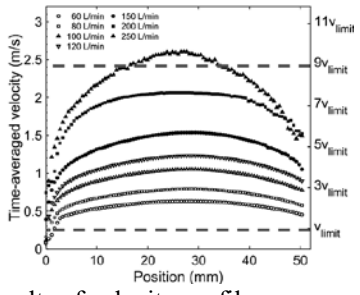

Fig. 1 Results of velocity profile measurement in the horizontal pipe.

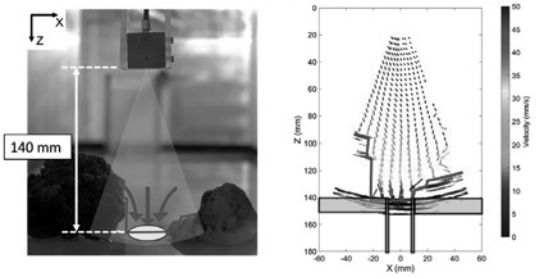

Fig. 2 Simulated leakage detection with WPD method.

4. Conclusion

To develop the wide velocity range flow measurement system, UVP system implemented the WPD method was constructed and the flow measurement was demonstrated. As the result, the velocities over the conventional v_{limit} were obtained by WPD method.

References

1. N. Shoji, H. Takahashi, H. Kikura: 15th International Conference on Fluid Control, Measurement and Visualization (FLUCOME2019), May 27-30, Naples, Italy, FLUCOME2019-298 (2019).

2. N. Shoji, H. Takahashi, H. Kikura: The 15th Asian Symposium on Visualization (ASV15), September 25-28, Busan, Korea, ASV-0173 (2019).

A.5 Application of UVP for 2D Velocity Vector Profile Measurement on Bubbly Flow

Hiroshige Kikura, Takao Ishizuka, Kazumi Kitayama and Hideharu Takahashi

1. Introduction

Two-phase bubbly flow is a fundamental phenomenon occurred in the coolant of Boiling Water Reactor (BWR). For the designing of BWR, the boiling two phase bubbly flow occurs on the coolant; gas and liquid phases. In order to optimize the reactor design according to the safety aspect, the multi-scale models have utilized to analyze and predict the flow characteristics which affected by the coolant in multi-dimensional pattern on the nuclear fuel assembly. The model employs numerous empirical correlations and consecutive equation. To validate and confirm analyzed data, the experimental data by conducting experimental work is needed for the validation. Indispensably, phase distribution of the gas and liquid phase and momentum transfer in the coolant affect to the design criteria. It directly related to multi-dimensional velocity distribution or velocity vector of the both phases in the bubbly flow. Consequently, experimental data of this parameter is needed to be obtained. The Ultrasonic Velocity Profiler (UVP) method was utilized in this study. It is a nonintrusive measurement. It can be applied to do the measurement even in the complex test section or less of optical access as the nuclear fuel assembly structure. This method uses a pulsed echography of an ultrasonic wave reflected from moving reflector such as particles dispersed in a liquid to obtain the velocity profile of the liquid. In bubbly flow, the multi-dimensional velocity vector of bubble and liquid can be measured simultaneously if the multiple transducers is applied to reconstruct the velocity vector and the information of both phases can be classified. This study proposes the development of UVP method for obtaining the multi-dimensional velocity vector profile of bubbly flow [1-2]. It is called Developed-UVP in this study. The development is focused on the two-dimensional velocity vector profile measurement.

2. Methodology and experiment

The schematic of Developed-UVP and experimental apparatus is shown in Figure 1. The multiple transducers consists of one transmitter and two receivers was employed. The Doppler signal that reflected from the moving reflector is obtained by two receivers. Hence, the 2D velocity vector profile can be reconstructed. Secondly, in the bubbly flow, the frequency and amplitude of the Doppler signal reflected by bubble and particle inform the velocity and the identity of each reflector. Therefore, the velocity information of bubble and particle (liquid) can be classified by phase separation algorithm which is the integration of time-frequency analysis and Doppler amplitude classification. By applying the multiple transducers and the phase separation technique into the UVP system, the 2D velocity vector profile of both phases can be obtained separately. To confirm the applicability of Developed-UVP, the experiment was conducted on a rectangular bubble column flow loop. The 2D velocity vector profile measurement in bubbly flow was demonstrated. In the experiment, the flow loop was set at 14L/min. The bubble was generated by bubble generator. The performance evaluation was done by comparing with the PIV method. Then, the measurement was executed in there difference locations.

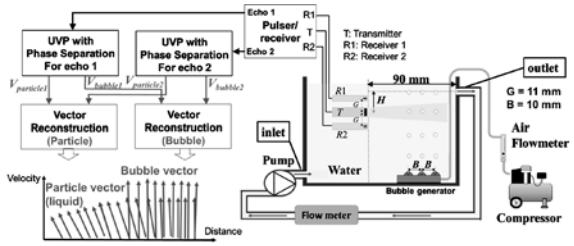

Fig 1. Experimental apparatus and measurement system

3. Result and discussion

The measurement comparison with the PIV was done with the discrepancy ±15% [2]. Figure 2 shows the result of the average velocity vector profile (5000 instantaneous profiles) on bubbly flow obtained by Developed-UVP. The velocity vector profiles obtained at three difference levels was reasonable. It informs that the bubbles motion was mostly in a vertical direction and the liquid moved to the outlet of the loop.

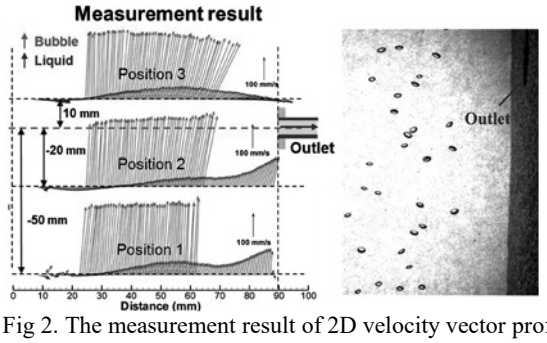

Fig 2. The measurement result of 2D velocity vector profile

4. Conclusion

The UVP method with the integration of multiple transducers and phase separation technique was developed can obtain 2D velocity vector profiles of bubbles and liquid in the two-phase bubbly flow.

References

1. W. Wongsaroj, H. Takahashi, N. Thong-un, H. Kikura: ASME-JSME-KSME 2019 8th Joint Fluids Engineering Conference (AJKFluids2019), July 28–August 1, San Francisco, CA, USA, AJKFluids2019-5636 (2019).
2. W. Wongsaroj, J. T. Owen, N. Thong-un, H. Takahashi, H. Kikura; The 27th International Conference on Nuclear Engineering (ICONE27), May 19-24, Tsukuba, Japan, ICONE27-2257(2019).

A.6 Measurement of Two-phase Flow Behavior in the Wet-type Filtered Containment Venting System

Hiroshige Kikura, Tadashi Narabayashi and Hideharu Takahashi

1. Introduction

In this study, the two-phase flow pattern in the the Wet-type scrubbing filter of the Filtered Containment Venting System (FCVS) was visualized using a High-Speed Camera (HSC) [1]. The important parameters of the flow were measured such as the interfacial area concentration, the bubble velocity, and the bubble diameter distribution, etc. These are the key parameters that directly affect the efficiency of the wet-type aerosol filter.

2. Measurement

2.1. Experimental Apparatus

For the experiment, a test facility that simulated a FCVS was constructed in the Tokyo Institute of Technology. The schematic of the test facility is shown in Fig. 1. It simulated as the combination of multi-layer filtration including a wet-type aerosol filter and a multi-stage dry-type filter. The wet-type filter is the vertical cylindrical scrubbing pool with an inner diameter of 20 cm, the wall thickness of 1 cm and the total length of 2 m. The working liquid that was used in the wet-type filter is water. The square cross-section Venturi Scrubber Nozzle was installed at the bottom of pool to generate bubbles. At the downstream of the scrubbing pool, a metallic vane mist eliminator was installed to remove the water entrainment droplets in the airflow before it enters the second filter layer.

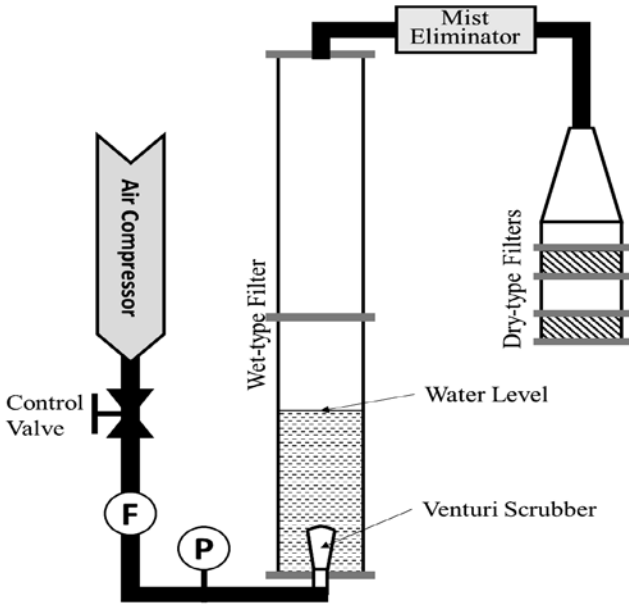

Fig. 1 Schematic diagram of the test facility.

2.2. Measurement Method

The flow pattern in the scrubbing pool of the wet-type filter was visualized using a high-speed camera. The backlight illumination was applied for visualization.

The recorded images of the High-Speed camera were processed using MATLAB R2018b programming software. By analyses, the parameters of each bubble such as the cross-section areas, boundaries, and centroid positions were derived. Using a tracking algorithm, the bubble diameter, bubble velocity and the average interfacial area concentration of the air-water interphase were calculated.

2.3. Measurement Results

Figure 2 shows that the interfacial area concentration increased as the increasing of the air injection flow rate. This increasing of the interfacial area concentration is expected for the increasing of the decontamination factor of the wet-type filter because it means that the probability that aerosol particles in the gas-phase come to contact with the gas-liquid interfacial surface will be increased, and; the aerosol particles will easier to be absorbed into the liquid-phase.

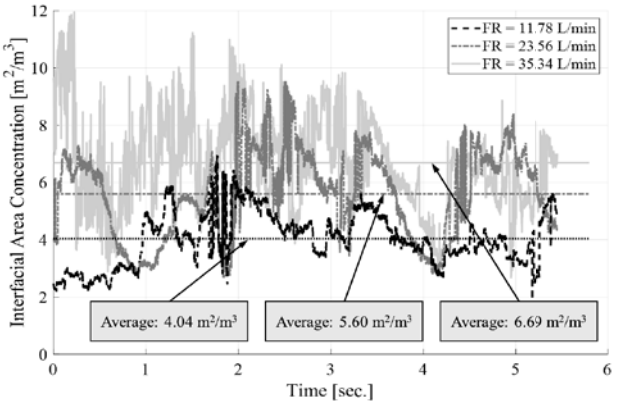

Fig. 2 Interfacial area concentration at different conditions of the air injection flow rate.

3. Conclusions

The behavior of the two-phase flow in the scrubbing pool of the wet-type filter was visualized at low conditions of air injection flow rate. The important parameters that able to affect the decontamination factor were measured such as the bubble size distribution, the gas-phasic velocity, and the gas-liquid interfacial area concentration.

Reference

1. T.V. Tran, H. Takahashi, T. Narabayashi, H. Kikura: 14th International Symposium on Advanced Science and Technology in Experimental Mechanics (14th ISEM'19-Tsukuba), November 1-4, Tsukuba, Japan, (2019).

A.7 Microscopic hydrodynamic bubble behaviour in suppression pool during wetwell venting

Hideharu Takahashi, Hideo Nagasaka and Hiroshige Kikura

1. Introduction

The severe accident in Fukushima Daiichi NPP increased the need for better understanding of an accident progression. A lot of attention has been paid on the integrity of Primary Containment Vessel (PCV) and minimization of fission products (FPs) release to the environment. However, the monitoring post radiation measurements showed increase after wetwell venting used to minimize the release of FPs to the environment as the efficiency pool scrubbing was deteriorated. Pool scrubbing codes combining bubble hydrodynamics and aerosol transport models are used to determine the pool scrubbing efficiency. However, the effect of bubble parameters, diameter and bubble rising velocity, on retention efficiency was not yet analysed much in detail. Therefore, data base is needed for hydrodynamic models in pool scrubbing codes under prototypical W/W venting conditions in Fukushima Daiichi accident to evaluate correlations for aerosol retention mechanisms in pool scrubbing codes from hydrodynamic point of view. In this study, we investigated the microscopic hydrodynamic bubble behaviour in suppression pool during wetwell venting [1-2].

2. Bubble parameters for pool scrubbing codes

Pool scrubbing codes adopted single bubble model based on average bubble diameter (BUSCA) or volume mean diameter (SPARC). In SUPRA, bubble diameter is depended on gas Re number and outlet diameter. In this study, bubble diameter distribution is represented using Sauter mean diameter (SMD), also called the surface–volume mean diameter. SMD is proportional to the ratio of total volume and total surface area calculated. For pool scrubbing phenomenon, the total bubble volume is proportional to the number of FP aerosols contained inside the bubble, and total bubble surface area is proportional to the removal rate of FPs aerosol. Therefore, SMD could be more appropriate than average bubble diameter, volume mean diameter or used correlation. However, SMD data for pool scrubbing are not available thus far.

3. Results and discussion

In this experimental study, the effects of air content, S/P temperature, submergence, and downcomer diameter on bubble parameters at the pool surface are evaluated under wetwell venting conditions applying the backlit shadowgraphy technique observing bubbles at the surface of the suppression pool in the test facility.

Results show that air content had small effect on SMD while rising velocity decreased with increasing air content. Under the lower submergence, SMD values were scattered more widely, and rising velocity showed dependency on temperature. SMD was not strongly affected by downcomer size, while bubble rising velocity tended to increase with increasing downcomer diameter. While thermal stratification did not have significant effect under tested range of conditions, with increasing S/P temperature SMD and bubble rising velocity decreased as a result of bubble break-up due to surface tension.

Bubble parameter effect on deposition velocity of aerosol retention mechanisms under atmospheric pressure was investigated (Fig. 1). Measured SMD and the corresponding v_b have a fair agreement with the values adopted in the pool scrubbing codes; thus, calculated values of several deposition velocities demonstrate fair agreement with those based on the measured data. Steam condensation is the dominant retention mechanisms except for low subcooling conditions. However, actual steam condensation driving force is not uniform. Therefore, modelling of steam condensation retention mechanism should be further carefully examined.

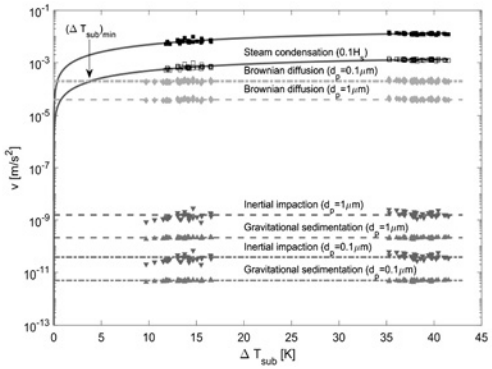

Fig. 1 Comparison of deposition velocities magnitudes based on measured SMD and v_b

4. Conclusion

Experimental results of bubble diameter represented by SMD and bubble rising velocity corresponding to SMD were obtained. The effects of varied parameters (air content, submergence, D_0, $T_{S/P}$) on SMD and bubble rising velocity were investigated. Furthermore, bubble parameter effect on deposition velocity of aerosol retention mechanisms was investigated. The collected database on SMD and bubble rising velocity and the physical explanation of varied parameters effect could be used for the update of pool scrubbing codes.

Reference

1. G. Zablackaite, H. Nagasaka, H. Takahashi, H. Kikura: 27th International Conference on Nuclear Engineering (ICONE27), May 19-24, Tsukuba, Ibaraki, Japan, ICONE-27-2300 (2019).
2. G. Zablackaite, H. Nagasaka, H. Kikura: The 14th International Symposium on Advanced Science and Technology in Experimental Mechanics (ISEM'19), November 1-4, Tsukuba, Ibaraki, Japan, A051 (2019).

A.8 Development of Advanced FMEA and Risk Visualization Method

Hideharu Takahashi and Hiroshige Kikura

1. Introduction

Stakeholders of nuclear power plant are aiming to strengthen risk communication through visualization of safety improvements of their equipments. The nuclear regulation authority incorporates risk-informed and performance-based ideas into their regulatory inspections. In this report, an advanced failure mode effect analysis method was developed that evaluates the priority of maintenance management for the risk of equipment repairability by combining failure mode effect analysis and probabilistic fracture mechanics in order to contribute to improving the safety of nuclear power plant equipments [1].

2. Advanced failure mode effect analysis

An trial analysis was performed for a failure mode of stress corrosion cracking in primary loop recirculation piping welds which was frequently reported to regulatory authority in Japan. The conditions of ultrasonic testing examiners capability, piping material, piping nominal diameter, operation period after stress corrosion cracking occurrence, and inspection interval were changed in the analysis. The effectiveness and usefulness of the advanced failure mode effect analysis method was demonstrated in the trial analysis. The evaluation results shown that the maintenance risk can be reduced by improving the capability of ultrasonic testing examiners and the inspection interval even when the potential risks related to piping repairability are high. Fig. 1 shows the result of potential risk. Fig. 2 shows one of the results of risk priority number.

3. Risk visualization of equipment

An evaluation method based on risk visualization of the equipment was developed in order to promote risk communication among stakeholders. It was shown that a radar chart for risk are the best visualization method. The results of the developed visualization method were compared with the results of the advanced failure mode effect analysis method. In addition, the results between the section 2 and the visualizetion of risk are compared. Fig. 3 shows one of the visualization results of the risk.

4. Conclusion

The developed risk visualization method enabled evaluation based on a comprehensive observation of safety and risk. In addition, it was clarified that the visualization method facilitates risk communication for reducing risk of equipments.

Reference

1. M. Kojima, H. Takahashi, H. Kikura: E-Journal of Advanced Maintenance, Vol. 11, No. 2, pp. 65-78 (2019).

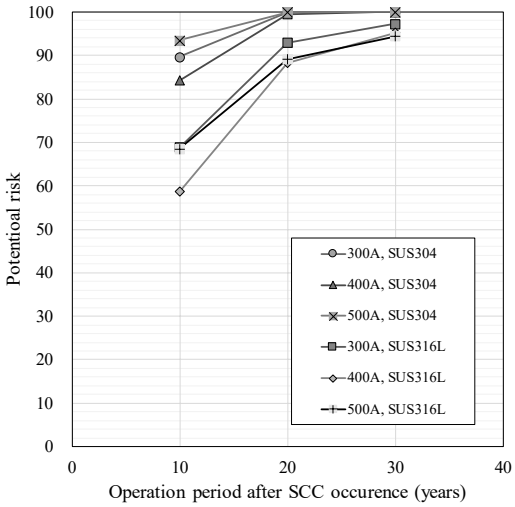

Fig. 1 Potential risk of the failure mode

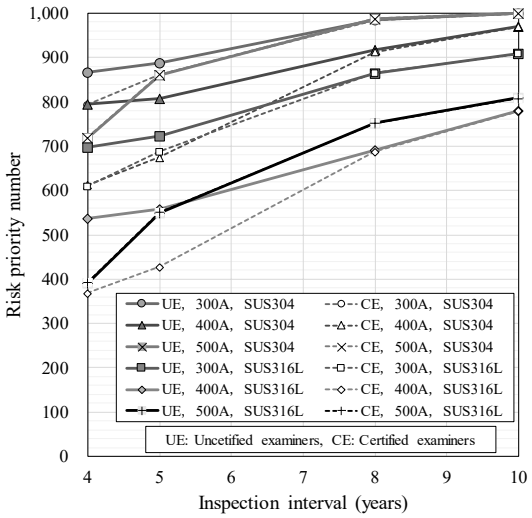

Fig. 2 Risk priority number of the maintenance

Inspection Interval (years)	10 years (operation period)						20 years (operation period)					
	Uncertified examiners			Certified examiners			Uncertified examiners			Certified examiners		
	R_O	R_S	R_D	R_O	R_S	R_D	R_O	R_S	R_D	R_O	R_S	R_D
5	 RA = 64.4 R = 58.7, RPN = 344			 RA = 55.3 R = 58.7, RPN = 263			 RA = 86 R = 88.3, RPN = 518			 RA = 74.8 R = 88.3, RPN = 396		
	8.16	7.20	5.86	8.16	7.20	4.49	9.55	9.25	5.86	9.55	9.25	4.49
10	 RA = 79.8 R = 58.7, RPN = 480			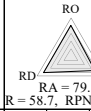 RA = 79.8 R = 58.7, RPN = 480			 RA = 104.9 R = 88.3, RPN = 723			 RA = 104.9 R = 88.3, RPN = 723		
	8.16	7.20	8.18	8.16	7.20	8.18	9.55	9.25	8.19	9.55	9.25	8.18

RA: Area of risk, R: Potential risk, RPN: Risk priority number
R_O: Occurrence, R_S: Severity, R_D: Detectability

Fig. 3 Visualization result of the risk (SUS316L)

A.9 Fundamental Study and Application on Stone Heat Storage System

Hideharu Takahashi, Susumu Ozaki and Hiroshige Kikura

1. Introduction

Since the Great East Japan Earthquake, Japan's energy problems have becoming a social problem that deeply affected people's living and businesses due to damage to nuclear power plants. Securing core energy, such as nuclear power generation and thermal power generation and reconstruction of the living energy for the local area is desirable.

For one of the methods to secure living energy, an TES (thermal energy storage) system which using air as HTF (heat transfer fluid) and stone as the storage material have been developed. By constructing a stone heat storage system, it gives a possibility of securing the basic living energy of disaster area residents.

In this study, the influencing factors of TES, which affect the thermal stratification, related to the performance of a stone heat storage tank, such as the porosity and mass flow rate, were investigated [1].

2. Numerical method and TES geometry

Geometry of the pilot-scale experiment TES (shown in Fig.1) was used for the numerical simulation. The TES tank is cylindrical shape and was made from stainless steel, with a diameter of 260mm and a height of 850mm. As it is shown in Fig.1, region number is the upper air zone, region number 2 is the porous zone and region number 3 is the lower air zone. In this study, the CFD simulation results will be focus only on the porous zone.

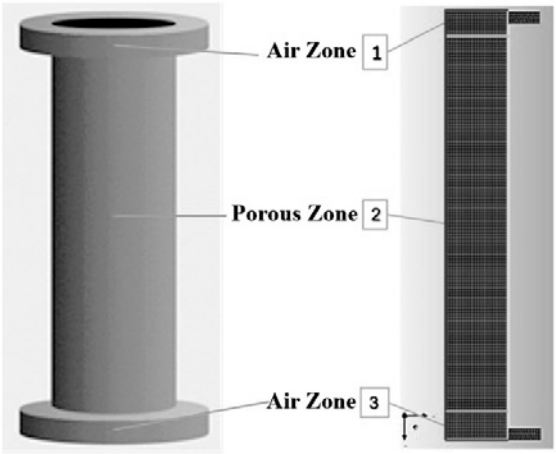

Fig. 1 Experimental tank and its 2D axisymmetric geometry

3. Results and Discussions

Fig. 2 presents the CFD simulation results during 8 hours charging and discharging process. The CFD simulation results were presented by the solid line. X axis shows the packed bed height in dimensionless form and Y axis shows the temperature in dimensionless form. The changing of thermal stratification for charging process seems moderate and for the discharging process is high. The mass flow rate seems too low for the charging process.

From the result of discharging process, we found that the thermocline zone is located in a part of the length of the heat store which indicates that the mass flow rate for the discharging process is suitable. The reason of trend difference of thermocline thickness between charging and discharging process is that smaller mass flow rate is more suitable for the discharging process and large mass flow rate is more suitable for the charging process.

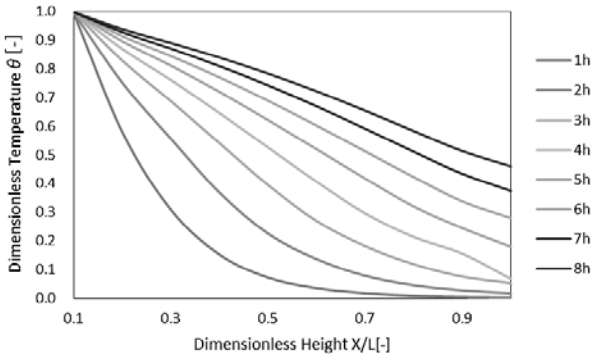

(a) Charging process

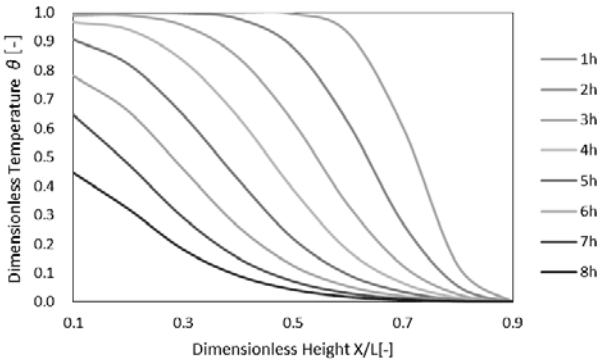

(b) Discharging process

Fig. 2 Numerical simulation result at the beginning of charging and discharging process

4. Conclusion

In this study, as one of the methods to secure living energy, an TES operating parameters, using stone as the storage material, during both charging and discharging cycle, was investigated using CFD simulations. An analytical evaluation for the thickness of the thermocline was discussed based on the CFD result. The changing of thermal stratification for charging shows moderate and discharging process shows high. From the result we found that the mass flow rate seems too low for the charging process and the mass flow rate for the discharging process is suitable.

Reference

1. Z. Weichen, R. N. Pratama, H. Takahashi, Y. Tamaura, H. Kikura: Advanced Experimental Mechanics, Vol.4, pp. 61-66 (2019).

A.10 Innovative liquid metal technology for fusion reactors

Masatoshi Kondo

1. Liquid tin (Sn) technology

Liquid tin (Sn) is a promising coolant for liquid surface divertor of fusion reactors due to its extremely low vapor pressure. The chemical compatibility of liquid Sn with structural materials is one of the important issues. Corrosion behaviors of candidate structural and/or functional materials such as reduced activation ferritic martensitic (RAFM) steels, austenitic steels, Al-bearing steels (Fe-18Cr-3.3Al-1Si and Fe-15Cr-7Al-0.4Zr-0.21Ex.O), tungsten (W) alloys (pure W, W-4Ni-2Cu, and W-5Ni-2Fe), silicon carbide (SiC), and oxide ceramic materials (e.g. Al2O3, Fe2O3, and Cr2O3) in liquid Sn were investigated by means of corrosion tests in various ways at 773K and 873K. In addition to conventional corrosion tests such as static pot tests and flowing tests, corrosion tests under electron irradiation (8MeV, 100Hz) were also performed in the test facility of KURNS-LINAK. The corrosion characteristics of these materials were metallurgically analyzed by SEM/EDS, EPMA, XRD, and STEM/EDS. The corrosion mitigation measures by surface modification technologies (such as Al rich oxide layer and surface carbonization treatment) were also investigated. The corrosion was mainly caused through an alloying reaction in liquid Sn and was strongly influenced by the temperature. Al-rich and Cr-rich oxide layers of steels revealed an excellent corrosion resistance. Pure W and W alloys with surface carbonization treatment also revealed a corrosion resistance. The corrosion was promoted by the electron irradiation because of electron migration of steel alloying elements in liquid Sn. However, the electrically insulating layer such as Al_2O_3 layer can suppress the electro migration corrosion.

2. Liquid alkali metal (NaK, Na, Li) technology

Advanced fusion neutron source (A-FNS) is a key facility to investigate the irradiation effect of high-energy neutron on the material properties of F82H steel. The temperature condition of F82H specimens during the irradiation tests is one of the important parameters. The specimens are installed in the irradiation capsules with a thermal bonding fluid. Liquid lithium (Li), sodium (Na), and sodium-potassium alloy (NaK) are the candidate thermal bonding fluids. Their thermal properties are summarized in Table 1. The corrosion of the specimens by the thermal bonding fluids must be minimized in order to clarify the change of material properties due to the effect of neutron irradiation. The experimental study was performed to make clear the corrosion characteristics of F82H in the candidate thermal bonding fluids.

F82H steel corroded in liquid NaK due to the surface oxidation. Fe oxide was formed on the steel surface during the exposure to liquid NaK. The steel formed Fe-Cr-O in liquid Na. These different oxidation behaviors were based on the different chemical potential of oxygen dissolved in the liquid metals. The steel corroded in liquid Li mainly by the depletion of Cr. The carbides precipitated in its matrix also dissolved in liquid Li.

3. Liquid lead alloy technology

Liquid lead-lithium alloy (Pb-16Li) is a promising tritium breeder of fusion reactors. However, its chemical compatibility with structural and functional materials is one of the important issues. The compatibility study was performed to investigate the corrosion characteristics of various materials in high-purity liquid Pb-16Li alloy. The corrosion test was performed at 873K for 750 hours. The test materials are FeCrAl-ODS alloy, RAFM steel, and alumina forming steel (APMT). The preoxidation treatment on the Al bearing steels was performed at 1073K for 100 hours in air atmosphere before the corrosion test. Al bearing steels revealed corrosion resistance in liquid Pb-Li, since they were protected by Al-rich oxide layer which was formed by the preoxidation treatment.

Table 1 Thermal properties of thermal bonding fluids

	Melting point (°C)	Boiling point (°C)	Thermal conductivity (W/(m·K)) at 800K
NaK(22Na-78K)	-11	784	28.7
Na	98	881	62.9
Li	180	1342	53.7

B. Actinide Management Division

B.1 Cross-disciplinary nuclear system research for load reduction of radioactive waste management

Hidekazu Asano, Tomohiro Okamura, Eriko Minari, Masahiko Nakase, Hiroshi Sagara and Kenji Takeshita

1. Introduction

The geological disposal of high-level radioactive waste, in which radioactive waste is buried deep underground and the long-term radiation safety is ensured after the disposal site is closed by the isolation and containment of radionuclides, is a topic that has been discussed and recognized internationally[1,2], and the most advanced country, Finland, has reached the stage of construction of disposal site[3]. In Japan, activities to select candidate sites are currently underway[4]. On the other hand, research on partitioning and transmutation of nuclides is underway from the viewpoint of volume reducing and mitigation of the harmfulness of radioactive wastes. From the research on recovery of 99-99.9% of minor actinides (MA) such as Am and transmutation using fast reactor or accelerator drive system (ADS), possibility of reducing the radiological toxicity of the waste and downsizing the disposal area has been shown [5].

As can be seen from the term of back-end, the treatment and disposal of radioactive wastes are located at the most downstream side of the use of nuclear power. On the other hand, the characteristics of the radioactive waste to be disposed of are determined by burn-up of nuclear fuel, that is, the front-end process, which is the upstream side of the utilization of nuclear power. Therefore, in order to present effective and rational measures for reducing waste volume and mitigating harmfulness, it is desirable to take a bird's-eye view of the entire nuclear system from upstream to downstream. It can be said that this is a perspective that leads to overall optimization of waste management. However, since there are various processes and parameters in the fuel cycle, it is expected that the answer will change depending on the selection, that is, the combination of conditions, and where the viewpoint is taken from the overall perspective. Through such research, it is possible to present effective, rational, and highly feasible measures for reduction of volume and toxicity of vitrified waste, as an option. Radioactive waste management is the issues of the basis of nuclear power use. Therefore, it is necessary to establish the path leading to this option as a research method for overall optimization from the viewpoint of waste disposal located at the most downstream of the nuclear system.

2.Joint research program between Tokyo Tech and RWMC

A joint research program between Tokyo Tech and Radioactive Waste Management Funding and Research Center(RWMC), which started in fiscal year of 2015, evaluates the effect of reducing the waste-occupied area in the geological disposal of high-level radioactive waste (vitrified waste) considering various fuel cycle conditions(fuel type, fuel burn-up, spent fuel cooling period, nuclide separation ratio, waste loading of vitrified waste, etc.) in nuclear power use. Introducing an evaluation indexes that comprehensively consider the fuel cycle conditions, including separation of MA, Cs/Sr, Mo, and platinum group metals(PGM), the relationship with the maximum temperature of the buffer material in contact with the vitrified waste at the repository was evaluated. From the results for the vitrified waste derived from UO_2 fuel, it is possible to reduce the waste occupied area (in other words, the amount of waste) by combining various process conditions such as the cooling period of spent fuel, nuclide separation ratio and waste loading of vitrified waste. And it has been confirmed that the waste occupied area can be reduced to about 1/2 due to the relatively low nuclide separation ratio of 70 to 90% [6].

Since then, this joint research program has expanded the scope of the works to the evaluation of burn-up calculation of fast reactor incorporating MA separation, and the geological disposal evaluation of vitrified waste derived from MOX fuel [7-14].

3. Nuclear system research based on the environmental impact of waste disposal

3.1 Start of a new research program and its outline

Based on the results of the joint research in 1. above, overlooking the entire nuclear system and assuming the introduction of a simplified MA separation process with 70% to 90% MA(Am) separation, a new research program regarding an environmental load in waste disposal, evaluation of various quantities of the entire fuel cycle, engineering feasibility of separation technology, and advancement of fast reactor burn-up mode was started in this fiscal year of 2019. As a result of this new research, a cycle condition combination that contributes to reduce the environmental impact caused by heat generation and radiation in waste disposal will be presented as an option for nuclear power systems. At the same time, the research method for presenting this option will be established as a basis for the global optimization research of the nuclear system.

This research is carried out as a nuclear system research and development project, which is a publicly recruited in the first year of Reiwa by the Ministry of Education, Culture, Sports, Science and Technology. And it belongs to the latter of the two application fields for safety-basis technology and volume reduction and mitigation of harmfulness of radioactive waste, which will carry out the

research for four years from this fiscal year of 2019.

Tokyo Tech is in charge of research on quantity evaluation of entire nuclear fuel cycle and MA separation mechanism, while RWMC, which is mainly responsible for research and development of radioactive waste disposal, as the research institute for this program. In addition, JAEA and Hokkaido University are participating in the research on engineering feasibility of MA separation process and improvement of burn-up model of fast reactor, respectively.

3.2 Research items and results in fiscal year 2019

(1) Environmental impact assessment research on waste disposal

① Evaluation and derivation of evaluation index

The environmental impacts of waste disposal were categorized into two categories: environmental load focusing on the amount of wastes and radiation effects, and contribution of nuclear power use, and the research results of past studies were investigated and analyzed. Radiation effects are divided into two categories: a dynamic evaluation that evaluates long-term safety after closure of repository on the premise of nuclide migration, and a static evaluation that is the radiotoxicity itself of the radioactive waste to be disposed.

② Quantitative evaluation of nuclear fuel cycle

In order to calculate fuel cycle quantities with consideration for the separation of MA nuclides, survey on the calculation conditions and calculation functions of the Nuclear Fuel Cycle Simulation System (NFCSS) code of the International Atomic Energy Agency (IAEA), and trial calculations were performed.

(2) Engineering design study of Am separation process

①Verification of separation mechanism

In order to evaluate the simplified MA separation process, we investigated published papers and research institute reports on batch recovery of MA-RE (rare earth elements) and extractant for MA isolation and flow sheet of extraction. The engineering feasibility of simplified separation and the flow sheet in that case were examined.

② Engineering feasibility of separation process corresponding to the separation ratio based on various quantity evaluations

Using the existing calculation code for solvent extraction, process simulation was performed on the basic configuration of the simplified MA separation process, and the number of separation stages of the MA/RE mutual separation process under low Am recovery rate conditions was compared to the case of conventional high recovery rate conditions.

(3) Advancement of fast reactor burn-up model corresponding to various preconditions

Input data on fuel burn-up, cooling of spent fuel, reprocessing, etc. were prepared for the core setting of the fast reactor for the evaluation of MA nuclide recycling and the burn-up calculation.

From the viewpoint of simplified MA separation, deepened discussion and information exchange on the interface between the concept of long-term safety of geological disposal and reduction of harmfulness of radio toxicity, the evaluation of the balance of various quantities of the entire nuclear fuel cycle, the method of rationalizing the MA separation process, and advancement of fast reactor burn-up model are discussed.

3.3 Works in fiscal year of 2020

From the viewpoint of rational integration of nuclear systems, it is necessary to keep in mind the following items and deepen mutual cooperation among research items.

- Mitigation effect of radiological toxicity in simplified MA separation
- Presentation of environmental impact assessment index
- Cooperation of Simplified MA separation and fast reactor burn-up conditions
- Expansion of calculation functions based on NFCSS for MA separation ratio, vitrified waste specifications, and geological repository area[15]
- Concept of transition period, introduction period, and equilibrium period in fast reactor core design

4. Towards the integration of nuclear systems

In order to further advance cross-disciplinary nuclear system research, it is necessary to pay attention to the following points.

(1) Spent MOX fuel management

Evaluation of geological disposal of MOX fuel-derived vitrified materials considering related process conditions such as fuel specifications, reprocessing, and vitrification conditions.

(2) Effect of harmfulness reduction in waste disposal

It is necessary to evaluate the effect of nuclear system options presented under various cycle conditions for harmfulness reduction. At that time, attention should be paid to the long-term safety assessment by nuclide migration at the repository system and the selection of the scenario in the assessment.

(3) Nuclear utilization scenario

It is required to investigate and create nuclear power utilization scenarios they are closely related to the qualitative and quantitative conditions such as process configuration, conditions/parameters, and quantity from front to back-end systems.

References

[1] OECD/NEA（1995）：The Environmental and Ethical Basis of Geological Disposal of Long-Lived Radioactive Wastes, A Collective Opinion of the Radioactive Waste Management Committee of the OECD Nuclear Energy Agency.

[2] IAEA（1989）: Safety Principles and Technical Criteria for the Underground Disposal of High-Level Radioactive Wastes, IAEA Safety Series No. 99.

[3] Nuclear Waste Management at Olkiluoto and Loviisa Power Plants: Review of Current Status and Future Plans

for 2019-2021, Summary, YJH-2018, Posiva Oy, December 2019
[4] Literature Survey for Geological Disposal, NUMO, 2020
https://www.numo.or.jp/chisoushobun/ (in Japanese)
https://www.numo.or.jp/government/oubo/pdf/literature_survey_20200117.pdf (in Japanese)
https://www.numo.or.jp/en/about_numo/new_eng_tab05.html (in English)
https://www.numo.or.jp/en/about_numo/new_eng_tab06.html (in English)
[5] Current Status of Partitioning and Transmutation Technology, Atomic Energy Society of Japan, 2016, ISBN-978-4-89047-163-8 (in Japanese)
[6] S. Sato, et al., Technical Options of Radioactive Waste Management for the second half of the 21st century, in consideration of Pu utilization and less environmentally impacted geological disposal, 3O11-3O16, Proceedings of AESJ Annual Meeting 2018, Osaka University, March 26-28, 2018 (in Japanese)
[7] G. Chiba, et al., Technical Options of Radioactive Waste Management for the second half of the 21st century, in consideration of Pu utilization and less environmentally impacted geological disposal, 1B07-1B08, Proceedings of AESJ Annual Meeting 2019, Ibaraki University, March 20-22, 2019 (in Japanese)
[8] H. Asano, et al., Technical Options of Radioactive Waste Management for the second half of the 21st century, in consideration of Pu utilization and less environmentally impacted geological disposal, 1C17-1C19, Proceedings of AESJ Annual Meeting 2019, Ibaraki University, March 20-22, 2019 (in Japanese)
[9] H. Asano et al., Cross-sectoral study on nuclear energy system for less-impacted radioactive waste management; Effect of various spent nuclear fuel properties and reprocessing conditions on geological disposal, Proc. International Conference on the Management of Spent Fuel from Nuclear Power Reactors: Learning from the Past, Enabling the Future(SFM-19), IAEA Headquarters, Vienna, Austria, 24−28 June 2019
[10] T. Okamura et al., Reduction of geological disposal area by introducing partitioning technologies under conditions of high burn-up operation and high content vitrified waste, Proc. SFM-19, IAEA Headquarters, Vienna, Austria, 24−28 June 2019
[11] E. Minari et al., Environmental load reduction of geological repository by minor actinide separation: Utilization of MOX fuel in future fuel cycle system, Proc. SFM-19, IAEA Headquarters, Vienna, Austria, 24−28 June 2019
[12] Y. Kobayashi,et al., Nuclear waste inventory calculations from fuel cycle with fast reactors by a reactor physics code system CBZ, Proc. Reactor Physics Asia Conference 2019(RPHA19), Dec. 2-3, 2019, Osaka International House Foundation, Osaka, Japan
[13] T. Okamura, et al., Reduction of the waste occupied area by nuclide separation and horizontal emplacement of waste package, Proc. Waste Management 2020 Conference, March 8-12, 2020, Phoenix, Arizona, USA
[14] G. Chiba, et al., Technical Options of Radioactive Waste Management for the second half of the 21st century, in consideration of Pu utilization and less environmentally impacted geological disposal, 2D01-2D04, Proceedings of AESJ Annual Meeting 2020 (in Japanese)
[15] Nuclear Fuel Cycle Simulation System: Improvements and Applications, IAEA-TECDOC-1864, 2019-

B.2 Study on Degradation of Fuel Debris by Radiation, Chemical, and Biological Damage

Toshihiko Ohnuki, Masahiko Nakase, Satoshi Chiba, Yoshiyuki Oguri, Takehiko Tsukahara, Koichiro Takao, and Kenji Takeshita

1. Background

Weathering is known to alter a primary mineral to secondary ones, being occurred in the environments[1]. Even though the fuel debris produced during sever accident at Fukushima Daiichi Nuclear Power Plant (FDNPP) are hard, the fuel debris may be degraded by weathering. One of the fastest weathering of the fuel debris is observed at Chernobyl Nuclear Power Plant (CNPP), where so called elephant foot was degraded in the period from 1986 to 1996, and fuel dusts containing U and Pu have produced.

Environmental condition of the reactor zone, defined as the zone accumulating fuel debris, between FDNPP and CNPP is very different. In the reactor zone of FDNPP, most of the fuel debris are soaked with cooling water which is mixture of groundwater and the circulated water treated by ALPS system to remove radionuclides. On the contrary, in the reactor zone of CNPP, they are contacting with air. This discrepancy may result in different degradation processes in FDNPP from in CNPP. However, we have no information of degradation of fuel debris under such condition as in FDNPP.

Weathering of minerals is divided into two processes[2]. One is congruent dissolution of minerals, in which minerals are completely dissolved in water. The other is incongruent dissolution of minerals, in which part or all of the dissolved minerals are precipitated to form secondary minerals. Weathering of uranium bearing minerals is reported to be formed secondary minerals even it is present as tetra-valent and/or hexa-valent.

The fuel debris is mainly composed of U, Zr, and Fe. It also contains fission products including ^{137}Cs and ^{90}Sr. If the fuel debris is congruently dissolved, some components are detected in the contaminated water circulating between the reactor zone and the treatment system of ALPS. TEPCO reported that concentration of U in the contaminated water is very low[3]. Low solubility of actinides suppresses leaching of actinides from the simulants of fuel debris[4,5]. These indicate that the fuel debris may be incongruently dissolved, if some part of the debris is dissolved in the circulating water.

It is well known that inorganic and organic chelating substances are associated with the dissolved actinides. Microorganisms exudate organic materials to associate transient elements for metabolism. Corroding materials accumulated in the reactor zone may sorb the dissolved actinides. So, chemical[2] and biological effects[6,7] may affect the degradation of the fuel debris. Therefore, chemical and biological effects on the degradation of the fuel debris should be studied under irradiation condition proceeding in the reactor zone.

2. Outline of research project

Research scientists in LANE and JAEA including the experts in radiochemistry, nuclear chemistry, nuclear physics, and fuel materials science, as well as the experts in environmental microbiology, conducts the project to clarify the effects of irradiation, and chemical and biological effects on the fuel debris in the reactor zone (Fig. 1). In the project, dissolution experiments of simulants of fuel debris are planned. The samples obtained by the experiments are analyzed by the advanced analytical equipment of JAEA in the international collaborative research building in Tomioka Town, Fukushima. In the experiments and the following analyses, the changes in debris properties and element elution behavior, and use the combined effects of radiation damage and chemical and biological damage under oxidizing environment are analyzed. For the purpose of elucidating the mechanism of debris deterioration, the final goal is to express the deterioration due to the combined functions in the presence of oxygen as a function of time.

Reference

1. TY. Goddereria, et al.,Elements, 15 (No. 2), pp. 103-106 (2019).
2. C. V. Putnis and E. Ruiz-Agudo, Elements, 9 (No. 3), pp177-182 (2013).
3. B. Grambow and C. Poinssot, Elements, 8 (No. 3), pp213-219, (2013).
4. A. Nakayoshi, et al., Nuclear Engineering and Design, 360, 110522, (2020).
5. T. Sasaki, et al., J. Nuclear Sci. Tech., 53 (No. 3), 303-311, (2016).
6. G. Southam, Elements, 8 (No. 2), pp. 101-106, (2012).
7. Q. Yu, et al., Geochimica Cosmochimica Acta, 174, 1-12(2016).

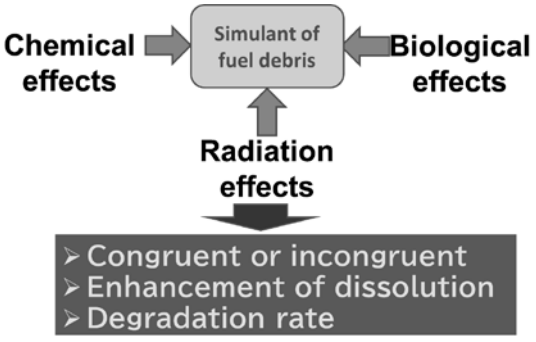

Fig. 1 Outline of research Project

B.3 Development of mass balance analysis code for various waste management scenario

Tomohiro Okamura[1], Akito Ohizumi[2], Kenji Nishihara[2], Masahiko Nakase[1] and Kenji Takeshita[1]
1. Tokyo Institute of Technology, 2. Japan Atomic Energy Agency

1. Introduction

In recent nuclear technology development, the research and development (R&D) in the field of waste management such as reprocessing, vitrification and geological disposal have remarkably promoted. Furthermore, the R&D of partitioning and transmutation technologies for the purpose of the less-impacted waste disposal. Therefore, it is important to evaluate the impact of those technical options on the waste management. It is additionally significant to consider the combinations of technical options that will contribute to establish the rational waste management and nuclear fuel cycle.

The Japan Atomic Energy Agency (JAEA) has developed the Nuclear Material Balance (NMB) code [1] for the mass balance analysis in nuclear fuel cycle. The some of the functions of NMB code were shown in below:

(1) Running on Microsoft Excel®
(2) Analysis of various mass balances in the nuclear fuel cycle from uranium mining amount to geological disposal area
(3) Handling 26 actinides and 2 fission products (FP)
(4) The burn-up and decay calculation are as accurate as ORIGEN-2 code.
(5) Possible to calculate the various reactor types and fuels

Since the NMB code was developed specifically for the mass balance analysis of actinides, the function of waste management scenario analysis was not sufficient. The Takeshita Lab., which has studied the waste management scenario, started to improve the NMB code in collaboration with Research group for Nuclear Transmutation System in JAEA from 2019. This research activities were presented at the 15th reprocessing and recycle division seminar of AESJ, and the presenter received the award of excellence. This report summarized the research by Takeshita Lab. and JAEA in 2019.

2. Improvement of NMB code

2.1 Selection of FP nuclides

In order to improve the waste management scenario analysis system in NMB code, it was necessary to be able to explicitly calculate FP nuclides in the code. However, ORIGEN code, which widely used for burn-up and decay calculation, handled about 1200 FP nuclides, and it was necessary to select the FP nuclides required for NMB code. In this study, the selection of FP nuclides was conducted under 4 burn-up conditions and 5 criteria such as mass, heat generation rate, radioactivity, exposure dose, vitrification inhibitor and using the index of "recall ratio of ORIGEN calculation".

As a result, the FP data set with recall ratios of 99.9%, 95% and 90% was created. Furthermore, we created a FP data set (cross section, decay chain, etc.) that can be implemented in the NMB code

2.2 Preparation of nuclear data library in NMB code

In order to implement the mass balance analysis of FP nuclides in NMB code, it was necessary to update the nuclear data library. The nuclear data library in NMB code is constructed by specially converting from the nuclear data such as JENDL4.0 and ORLIBJ40. Therefore, we have developed a tool that quickly converts various nuclear data into a nuclear data library for NMB code. A schematic function of this tool is shown in the Fig.1. This tool works in Microsoft Excel®. Given any nuclides and library name as input, it outputs nuclear data for NMB code. This tool has a function of automatically constructing a burn-up and decay chain correcting loss of neglected FPs. With the development of this tool, it has become possible to implement the burn-up conditions calculated by various core calculation codes such as SRAC and MARBLE into NMB.

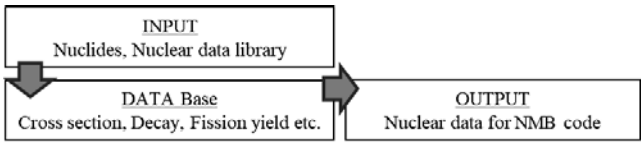

Fig.1 A schematic function of the tool

2.3 Update of the waste management scenario analysis system in NMB code

The back-end scenario analysis system in NMB code was updated for more flexible analysis of nuclear fuel cycle scenarios. In particular, it became possible to flexibly study the conditions of immobilization and disposal of waste. We will continue to update the back-end scenario analysis system.

3. Future Work

The NMB code will be updated and the nuclear fuel cycle scenario analysis will be carried out by the collaboration research between Takeshita Lab. and JAEA in 2020. The main items to be implemented in 2020 are as follows:

(1) Implementation of FP data set on NMB code
(2) Error evaluation and correction of burn-up calculation by NMB code and ORIGEN
(3) Update of waste management scenario analysis system in NMB code
(4) Analysis the various nuclear fuel cycle scenarios

Reference

[1] K. Nishihara et. al., "Utilization of rock-like oxide fuel in the phase-out scenario", J. Nucl.. Scie. Technol., 2014, 51: 150-165

Presentation and Award

・T. Okamura et. al., "Development of mass balance analysis code for various back-end scenario", 15th reprocessing and recycle division seminar, 2019

B.4 Investigation of adsorption mechanism of PGMs by Alminium Hexaferrocyanide

Masahiko Nakase, Ria Mishima, Sotaro Tachioka, Koji Kato, Miki Harigai and Kenji Takeshita

1. Introduction

In nuclear fuel cycle, spent nuclear fuels (SNFs) are reprocessed to recover U and Pu after a cooling period. During the reprocessing, high-level liquid waste (HLLW), which contains various kinds of radioactive nuclei such as minor actinide (MA), lanthanides (Ln), and platinum group elements (PGM; Pd, Ru, and Rh), is generated. The HLLW is planned to be vitrified in borosilicate glasses and disposed in deep underground. To guarantee the quality of the vitrified objects, amount of PGMs and Mo are limited. Separation of Pd is not a difficult task, but other PGM, Ru and Rh are known as difficult. Also, simultaneous separation of PGM and Mo is challenging. To enable such separations, we study the Aluminum hexacyanoferrate (AlHCF) as a candidate sorbent. The adsorption and calculation studies of Pd with various metal HCFs were done at our lab and Nagoya university supported by MEXT. In addition, some attempts were made to understand the adsorption mechanism of other PGMs in FY2019. AlHCF has different properties from other HCFs; instability against acid and capability of simultaneous Ru, Rh and Mo removal. We noticed that without Pd, AlHCF is eluted by nitric acid of wide concentration range, but when Pd is existed, elution of structure is minimized and Ru, Rh, and Mo were removed from solution. Therefore, we anticipated that quick Pd adsorption to AlHCF triggers the unique separation performance of AlHCF. To prove this hypothesis, adsorption experiments with single PGMs and competitive adsorption of Ru and Rh respectively with existence of Pd were implemented. Extended X-ray Adsorption Fine Structure (EXAFS) and synchrotron XRD and Pair Distribution Function (PDF) analysis were also done at SPring-8 and Photon Factory. In this manuscript, several new insights obtained in FY2019 are summarized.

2. Preparation of AlHCF and characterization

The synthetic procedure is summarized in Figure 1 and its XRD pattern and photograph is shown in Figure 2 [1]. The diffraction pattern was not sharp due to the defective synthesized AlHCF. The color was initially whitish blue but gradually turned into pale blue. This is due to the moisture or bulk water inside AlHCF even after dryness.

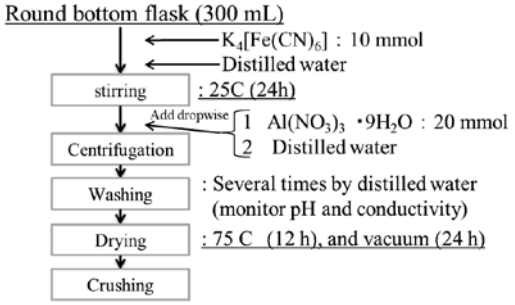

Figure 1 Synthetic scheme of AlHCF [1]

However, this slight color change has no big impact on the chemical composition and adsorption behavior of PGMs greatly, though big change in UV-Vis spectrum was seen.

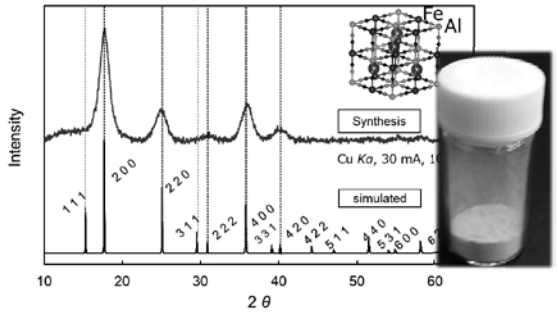

Figure 2 XRD patterns and picture of synthesized AlHCF

3. Result and discussion

3.1. Robustness against HNO_3

The elution against the different concentration of HNO_3 was implemented as compiled in Figure 3. With increase in HNO_3 concentration, the amount of remained solid became less and total dissolution was observed with 2.5 M HNO_3. With further increase in HNO_3 concentration, dissolution turned into less. This may be explained that the higher concentration of HNO_3 can elute AlHCF more but higher concentration allows to form protective film such as oxide layer which hinders the elution of AlHCF. To prove this hypothesis, soft x-ray experiments such as XPS and soft X-ray XAFS (and XANES) are effective, hence, we proposed PAC to Photon Factory and the proposal was accepted. These new experiments will be done in FY2020.

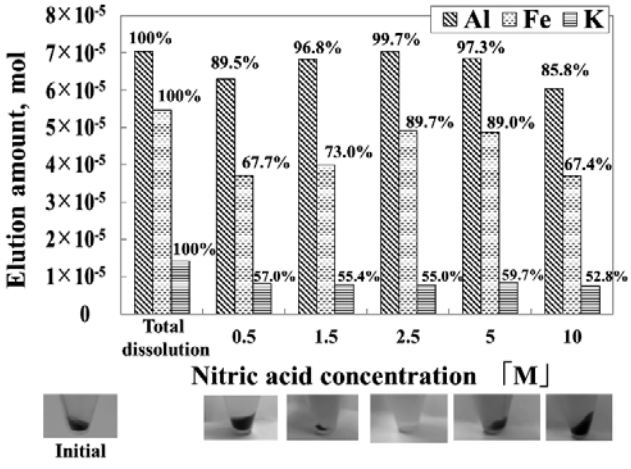

Figure 3 Effect of HNO_3 concentration on AlHCF dilution [1]

3.1. Adsorption of PGMs

The adsorption of single Pd, Ru, Rh (5 mM each), and

competitive adsorption of Ru, Rh (3 mM each) with Pd (2 mM) were compared in Table 1 and 2. In both the cases, 20 mg AlHCF were added into 10 mL of 1.5 M HNO_3 and contacted for up to almost one month. Adsorption of Ru and Rh were enhanced from single adsorption cases. The XRD patterns before and after the adsorption of Pd, Pd + Ru and Pd + Rh are summarized in Figure 4. Initial AlHCF and AlHCF + Pd show similar diffraction patterns. Pd^{2+} is replaced into Fe^{2+} of the AlHCF and the structure is stable. On the other hand, when Ru or Rh exist, XRD diffraction drastically changed and the both the spectra are similar. The radial structural function (RSF) obtained by EXAFS experiments after the competitive adsorption of PGMs clearly indicated that Ru and Rh are not the same chemical forms as HCF. Ru and Rh may adsorbed by the formed structure by Pd and AlHCF, or precipitated with eluted component of AlHCF. The detailed analysis and identification will be done.

Table 1 Sorption percentage of single Pd, Ru and Rh [1]

Time (d)	Pd	Ru	Rh
5.2	99.9	72.2	-
11.2	100.2	85.7	17.6
19.2	100.2	90.3	37.9
26.2	100.2	93.4	51.2

Table 2 Sorption percentage of Ru and Rh with Pd [1]

Contact time (d)	Pd-Ru		Pd-Rh	
-	Pd	Ru	Pd	Rh
5.2	100.0	97.5	99.9	48.3
11.2	101.8	100.0	102.0	54.8
19.2	101.1	100.4	101.6	63.9
26.2	100.6	100.4	101.6	65.4

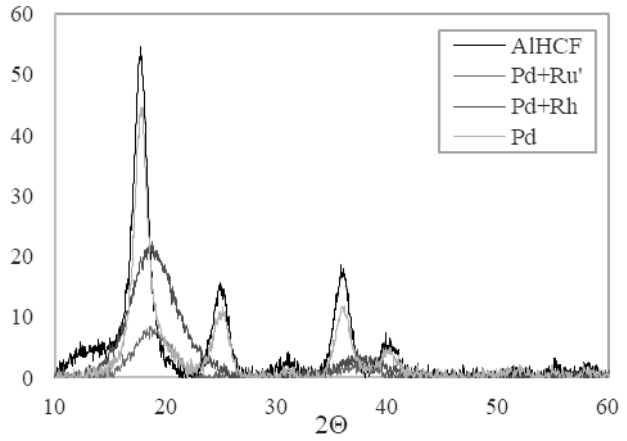

Figure 4 XRD patterns of PGM adsorbed AlHCF samples

4. Conclusion and plan

To understand the adsorption mechanism of not only Pd which have been intensively studied already, but also other PGMs, Ru and Rh, by AlHCF from HLLW, elution behavior of AlHCF by HNO_3 and adsorption behavior of PGMs were done in FY2019. Some of the important results are obtained by XRD and its PDF analysis, XAFS data by both hard and soft x-ray. Detailed discussion based on the experimental results will be continued in FY2020.

Acknowledgment

The research was supported by the The R&D program for advanced nuclear power systems, MEXT. EXAFS, sychrotron XRD and its PDF analysis were done at SPring-8 (2019A3740, 2019B1650, 2019B3737) and Photon Factory (2018G573, 2018G574).

Reference

(1) R. Mishima et al., Sorption properties of aluminum hexacyanoferrate for platinum group elements, Chemistry Letter, Vol.48, issue 8, 881-884, 2019

B.5 Study of Cs desorption from vermiculite by in-situ observation of soil in subcritical condition

Masahiko Nakase, Tatsuya Fukuda, Ryo Takahashi and Kenji Takeshita

1. Introduction

We have been studying the decontamination process of radioactive Cs from soil by hydrothermal treatment (HTT). By utilizing the rapid cation exchange in subcritical water condition created by HTT, more efficient removal of Cs is possible. The HTT technique in batchwise system was updated to continuous column system to enable the decontamination process more efficient and applicable to the actual field. This study is successful supported by some funds. On the other hand, the mechanism study is still needed to fully understand the HTT process. Therefore, we firstly tested the in-situ X-ray diffraction (in-situ XRD) and Pair Distribution Function (PDF) analysis, and Extended X-ray Adsorption Fine Structure (EXAFS) under subcritical water condition at Super Photon-ring 8 GeV.

2. Experimental Setups

Fig.1 and Fig.2 illustrate the schematics of experimental setup and pictures of detectors equipped at SPring-8 BL4B2. Cs-loaded vermiculite was packed into the small container made of stainless with sight glasses. The synchrotron light is penetrated through the glasses which enables to the in-situ experiments. Firstly, the pressurized water is pumped in the column and then, the solution is switched to water with 0.5 M of $MgCl_2$. The Cs desorption is occurred gradually and before the total desorption of Cs, XRD and XAFS spectra are collected. The EXAFS spectra are also obtained with the same container using Cs-K adsorption edge at BL1 of SPring-8.

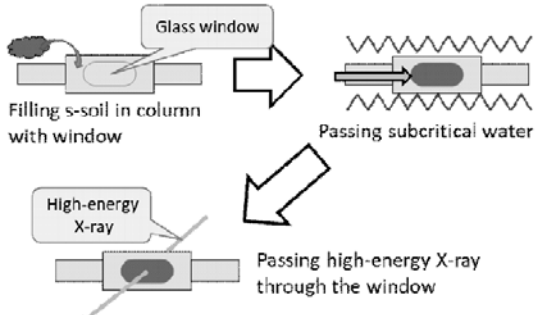

Figure 1 Experimental setup of in-situ experiment

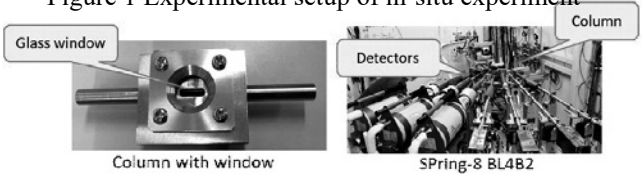

Figure 2 Pictures of experimental setup

3. Result and Discussions

The XRD patterns of Cs-loaded vermiculite at 150C before and after flowing $MgCl_2$ solution in time course are summarized in Fig 3. The Cs layer is gradually shifted to Mg layer, indicating the ion-exchange of Cs and Mg. Then PDF analysis is done based on the XRD data with chemical composition and density of vermiculite as shown in Fig.4. The broadening of the peak around 3-6 Å is attributed to the increased distance and distortion of the interlayers. Both the structural changes are triggered by the ion exchange reactions of Mg^{2+} and Cs^{+}. The EXAFS experiments reveals that the ratio of hydrated Cs in interlayer is increased which enables the diffusion of Cs ions efficient at 150 C. Our theoratica calculation also supported this phenomena. The detailed discussion is compiled our upcoming paper (1).

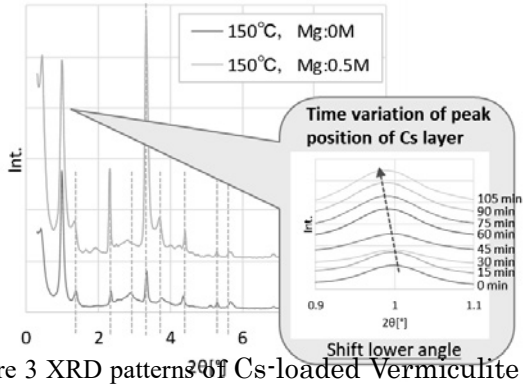

Figure 3 XRD patterns of Cs-loaded Vermiculite during the pressurized water flow at 150 C with and without $MgCl_2$ solution

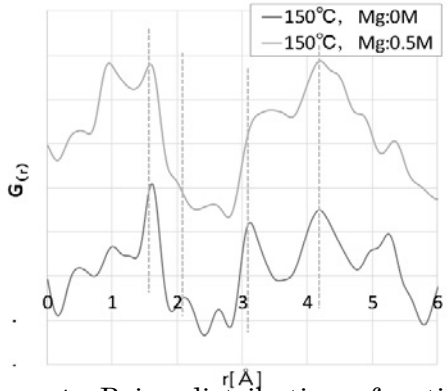

Figure 4 Pair distribution function of Verm-Cs at 150 C with and without $MgCl_2$ solution

Acknowledgment

The synchrotron experiments were accomplished at SPring-8 (2019A1682, 2019A1683, 2019B1767).

Reference

(1) T.Fukuda et al., Mechanistic study on the removal of Cs from contaminated soil by rapid ion exchange in subcritical water, J Nucl Sci Technol (accepted)

B.6 Separation of f-block elements by extractant-immobilized hydrogel - Relation between complexation and polymeric characteristics -

Masahiko Nakase[1], Miki Harigai[1], Daiju Matsumura[2], Takashi Kajitani[1], Tomoo Yamamura[3], Kenji Shirasaki[4] and Kenji Takeshita[1]
[1]Toyko Tech, [2]JAEA, [3]Kyoto Univ., [4]Tohoku Univ.

1. Introduction

We are studying many separation technique and the target elements are wide; Minor Actinide(MA), Lanthanide (Ln), Platinum Group Metal(PGM; Pd, Ru, Rh (important in nuclear reprocessing), Ir, Pt (important in a general industry)), fission products (FPs; Cs, Sr) and other metals such as Zr, Mo and Ag. Especially, MA/Ln separation is important in advanced nuclear fuel cycle, hence, we put more effort to enable this separation by applying gel/liquid extraction as well as development of extractants for conventional solvent extraction. Not only understanding of coordination chemistry of f-block elements (MA and Ln) in solution, but also the polymeric characteristics is important to upgrade the separation. Recently, general adsorption behavior of UO_2^{2+}, Th^{4+} and Ln^{3+} by extractant -immobilized hydrogels were implemented. In FY2019, we newly started some experiments to understand more about the polymeric characteristics of hydrogel adsorbents.

2. Concept of gel/liquid extraction

The most reliable separation technique of metal ions should be solvent extraction and is widely used in industry. However, the separation is based on thermodynamics and not much parameters can be tuned. Under such restriction, recognition of slight difference between MA and Ln is difficult. By introducing extractant into stimuli-sensitive hydrogel, more parameters can be tuned and the new concept, “Control of Coordination Field” is applied as shown in Fig.1 [1,2]. However, too complicated chemistry makes the understanding of the coordination field difficult, and reproducibility is sometimes worse than conventional solvent extraction. To solve this problem, the gels were thin-coated onto porous silica as shown in Fig.2. Due to application of this technique, reproducibility of adsorption experiments was greatly enhanced and in some cases, adsorption performance was beyond the performance by bulk gel may be attributed the increased surface area and kinetics.

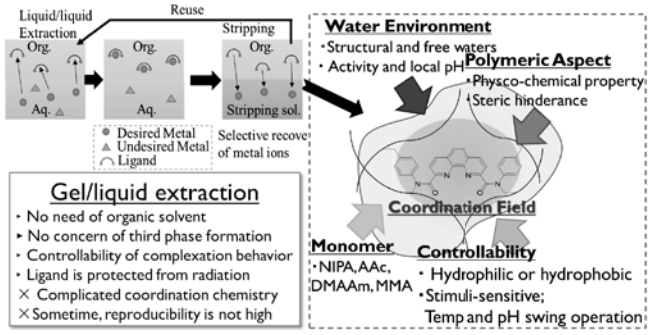

Figure 1 Concept of gel/liquid extraction.

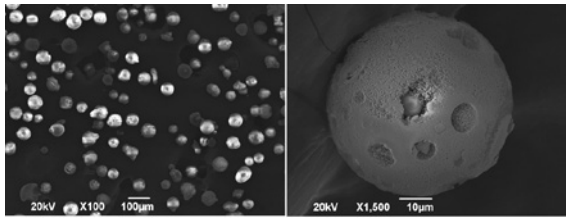

Figure 2 SEM images of gel thin-coated on porous silica.

3. Polymeric characterization

We have been studying the difference between solvent extraction and gel/liquid extraction and the results were reported elsewhere [1,2]. We have already started the time-dispersive X-ray Adsorption Fine Structure (DXAFS). DXAFS can provide the changing of the local structure of the metal ions in hydrogel when the external stimuli is induced. In FY2019, investigation of polymeric characteristics was started. Small Angle X-ray Scattering (SAXS) and Wide Angle X-ray Diffraction (WAXD), where SAXS can provide the conformational information of polymer chains and WAXD can provide information such as orientation of polymers and crystallinity, namely, shorter order structure than SAXS were started. By our first experiment, the conformational change of polymer was detected and there was a correlation between the change of the metal ion in the gel obtained by DXAFS for the first time. The obtained data was now under analysing. Figure 4 illustrates the experimental setups of SAXS at PF BL6A and Suzukake-dai campus of Tokyo Tech.

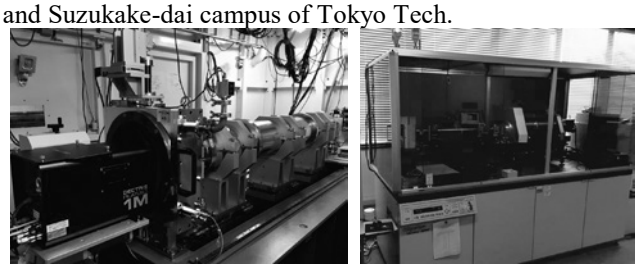
Figure 3 Experimental setup of SAXS; (1) Photon Factory BL6C and (2) Lab-SAXS at Suzukake-dai Campus.

4. Conclusion and plan

We started new approach to understand the mechanism of gel/liquid extraction and upgraded the materials and this activity will be continues for several years.

Acknowledgment

The activities were supported by JSPS grant-in-aid (18K19043), The PF(2019G687) and SPring-8 (2019B3737, 2019A3740, 2016B3508).

Reference

(1) M.Nakase et al., Prog Nucl Sci Technol,Vol.5,pp.56-60 (2018).
(2) M.Nakase et al., Separ Sci Technol, Vol.54, No12, pp.1952 -1959 (2019).

B.7 Development of stable solidification technique of ALPS sediment wastes by apatite ceramics

Masahiko Nakase, Shun Kanagawa, Ayumu Masuda, Miki Harigai, Kazuo Utsumi and Kenji Takeshita

1. Introduction

In FY 2019, we got a grant-in-aid from MEXT and started collaborative research with CREIPI, JAEA, Hitachi-GE and Nanyang Technological University (Singapore) for development of solidification method of ALPS sediment wastes into apatite ceramics. ALPS process can decontaminate the contaminated water from Fukushima Daiichi nuclear power plant but it generates sediment wastes which are difficult to deal with. In FY 2019, we started some basic studies.

2. Preparation of Simulated ALPS sediment waste

In FY2019, we began with synthesizing two kinds of simulated ALPS sediment wastes; Iron co-precipitation and Calcium carbonate wastes. Iron co-precipitation was synthesized by adding NaOH solution into $FeCl_3$ solution containing small amount of Cs and Sr, and Calcium carbonate waste are synthesized by adding Na_2CO_3 solution into $CaCO_3$ and $Mg(OH)_2$ solution containing small amount of Cs and Sr, as well. The synthesized wastes are shown in Fig.1. Both the wastes were vacuum-dried and SEM images were collected (Fig.2). The structures were quite similar to the actual wastes reported by TEPCO. Both the wastes were analyzed by some methods such as XRD, FT-IR and XAFS. Next year, the apatite ceramics will be synthesized by using these synthesized wastes.

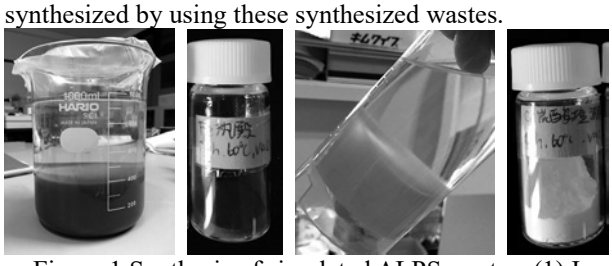

Figure 1 Synthesis of simulated ALPS wastes; (1) Iron co-precipitation and (2) Calcium carbonate

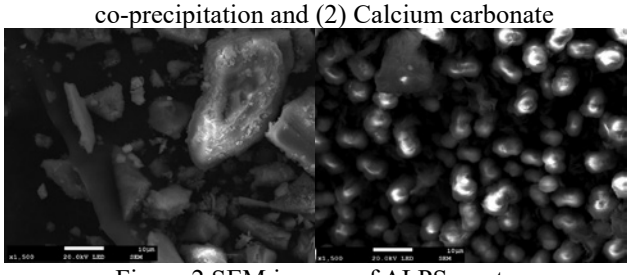

Figure 2 SEM images of ALPS wastes; (1) Iron co-precipitation and (2) Calcium carbonate

3. Synthesis and characterization of apatite waste forms

Synthesis of apatite ceramics containing Fe, Ca, Mg and FPs(Cs and Sr) were implemented with three methods; solid method, sol/gel method and hydrothermal method. Frist of all, $FeSr_8Cs(PO_4)_6(OH)_2$ and $Fe_2Sr_6Cs_2(PO_4)_6(OH)_2$ were synthesized by solid method with nitric acid and methanol by following our previous study [1]. The synthesis was successful and pure products were obtained. The SEM image of $Fe_2Sr_6Cs_2(PO_4)_6(OH)_2$ is shown in Fig 3. On the other hand, Mg and Ca were difficult to be immobilized into apatite structure may be due to the inappropriate ionic radii of Mg and Ca. Therefore, sol/gel method and hydrothermal method (both methods are done in basic solution) were tested. The synthetic procedure and result of characterization will be reports elsewhere in detailed, but the synthesis was rather successful and better phosphate compounds suitable for ALPS sediment wastes were determined.

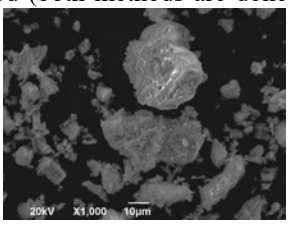

Figure 3 SEM image of $Fe_2Sr_6Cs_2(PO_4)_6(OH)_2$

Elution tests of the synthesized apatite was also done with different pH water. As a result, elution behavior of each element was different indicating that bond strengths affect greatly on the stability of apatite; Sr was quite stable in apatite, but the stability of Cs was relatively weaker compared with Fe. The compression experiments of apatite were also carried out with varying the pressure and temperature to find the appropriate condition to mold the apatite ceramixs.

4. Conclusion and plan

In FY2019, we have successfully launched the new project of ALPS sediment wastes disposal. The preliminary attempts to synthesize apatite ceramics were done with some methods and characterization study were started. Next year, we are planning to carry out DFT calculation to understand the chemical property of synthesized apatite and its stability. The engineering-scale apparatus will be designed and large-scale synthesis will be done to enhance the applicability of the proposed solidification method.

Acknowledgment

The research is undergoing by the supported of Advanced Research and Education Program for Nuclear Decommissioning, MEXT.

Reference

(1) S. Kanagawa et al., Synthesis and Characterization of Apatite Waste forms Using Simulated Radioactive Liquid Waste, Chemistry Letter, Vol.48, issue 8, 881-884, 2019

B.8 Crystal Structure of Regularly T_h-Symmetric $[U(NO_3)_6]^{2-}$ Salts with Hydrogen Bond Polymers of Diamide Building Blocks

Koichiro Takao, Hiroyuki Kazama, Yasuhisa Ikeda, and Satoru Tsushima

1. Introduction

A tetravalent actinide (An^{4+}) shows complicated complexation behaviour arising from its spherical shape that may allow accepting coordination interactions from any orientations unlike the typical equatorial coordination commonly observed in actinyl species (AnO_2^{2+}, An = U, Np, Pu).[1] In the reprocessing process for the spent nuclear fuels, the chemical behaviour of An^{4+} in HNO_3 aq is highly relevant,[2] however NO_3^- is not always strong enough to give a single predominant species. As a result, the coordination chemistry of An^{4+} in such a system is further complicated despite the importance in the nuclear engineering.

A limiting complex of An^{4+} with NO_3^- is known to be $[An(NO_3)_6]^{2-}$ (An = Th,[3-7] U,[8, 9] Np,[10, 11] Pu[12-14]), which shows 12 coordination number to fully occupy the coordination sphere of the centre An^{4+}.[15] According to Jin *et al.*,[3] formation of this hexanitrato complex, at least for Th^{4+}, is mainly governed by hydration enthalpy of a counter cation. Indeed, the reported $[An(NO_3)_6]^{2-}$ structures were usually isolated as salts of heavy alkali metals (*e.g.*, Rb^+ Cs^+) or NR_4^+ (R = H, alkyl), which exhibit lower hydration enthalpies than lighter cations like Li^+ and Na^+.

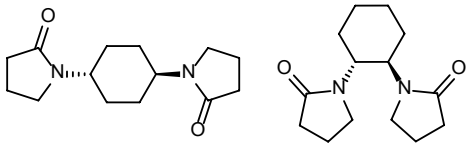

Fig. 1. Schematic structures of diamide building blocks employed in this study (L1, L2). An (*R*,*R*)-enantiomer of L2 is only displayed in this figure, while its racemate has been used in this work.

In contrast, H^+ has not been employed as a counter cation for $[An(NO_3)_6]^{2-}$ so far. This smallest cation shows the highest charge density in monovalent cations. Therefore, it should exclusively tend to form strong electrostatic interactions with anions. On the other hand, hydration of H^+ is the most exothermic,[3] and therefore, usually occurs to give an oxonium ion (H_3O^+), moderating the ionic interactions significantly. As a result, an acidic salt involving H_3O^+ is often fragile and hygroscopic unless somehow being stabilized.[4, 5] If dehydration of H^+ is successfully achieved, an avenue to prepare novel crystalline materials will be explored. In this communication, we demonstrate quantitative preparation of a regularly T_h-symmetric $[U(NO_3)_6]^{2-}$, which shows intrinsic colour of U^{4+} never reported before. The most critical point here is selection of appropriate diamide building blocks (**L1** and **L2**, Fig. 1),[16-18] which form hydrogen bond polymers to successfully liberate H^+ from its strongest hydration tendency.

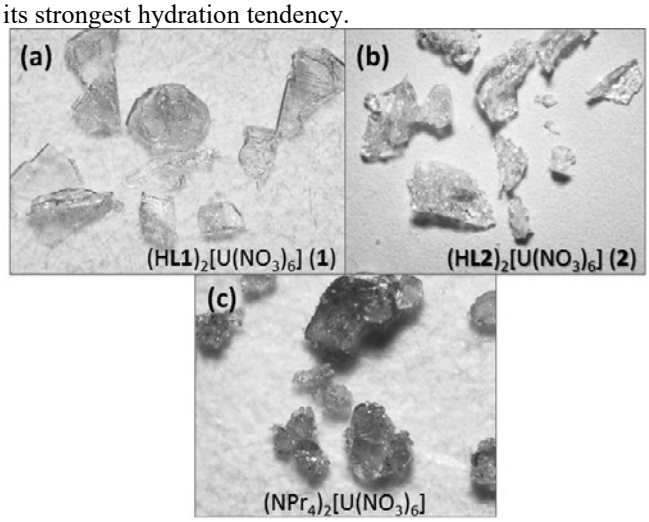

Fig. 2. Photomicrographs of (a) (H**L1**)$_2$[U(NO$_3$)$_6$] (1), (b) (H**L2**)$_2$[U(NO$_3$)$_6$] (2), and (c) (NPr$_4$)$_2$[U(NO$_3$)$_6$] under illumination of white LED light.

2. Results & Discussion

A U^{4+} stock solution (0.15 M, 100 μL) containing 3 M HNO_3 and 0.15 M N_2H_4 was layered with 3 M HNO_3 aq (30 μL) and 3 M HNO_3 solution of the diamide building block (**L1** or **L2**, 0.30 M, 100 μL) in a ϕ5 mm glass tube. Slow diffusion of U^{4+} and the diamide resulted in crystals with remarkably diminished colour (Fig. 2) in nearly quantitative yields (> 98%) as well as fading the green colour of the solution part. The green colour of the initial solution is believed to be a typical nature of U^{4+} arising from its $5f^2$ configuration. Nevertheless, the elemental analysis determined the chemical formulae of these compounds to be (H**L**)$_2$[U(NO$_3$)$_6$] (**L** = **L1** (**1**), **L2** (**2**)), where U^{4+} is actually present. Furthermore, both compound **1** and **2** clearly exhibit the characteristic absorption bands of U(IV) in the solid state UV-vis-NIR absorption spectra. Crawford *et al.* reported that $[U(NO_3)_6]^{2-}$ crystallizes with tetrapropylammonium (NPr_4^+) cations to give $(NPr_4)_2[U(NO_3)_6]$,[9] which has typical green colour as shown in Fig. 2. Although the absorption bands of **1** and **2** have been actually detected, it is difficult to quantitatively discuss differences in the absorption intensities of the solid samples. Anyway, as clearly demonstrated in Fig. 2, **1** and **2** are not green at all despite being U(IV) compounds.

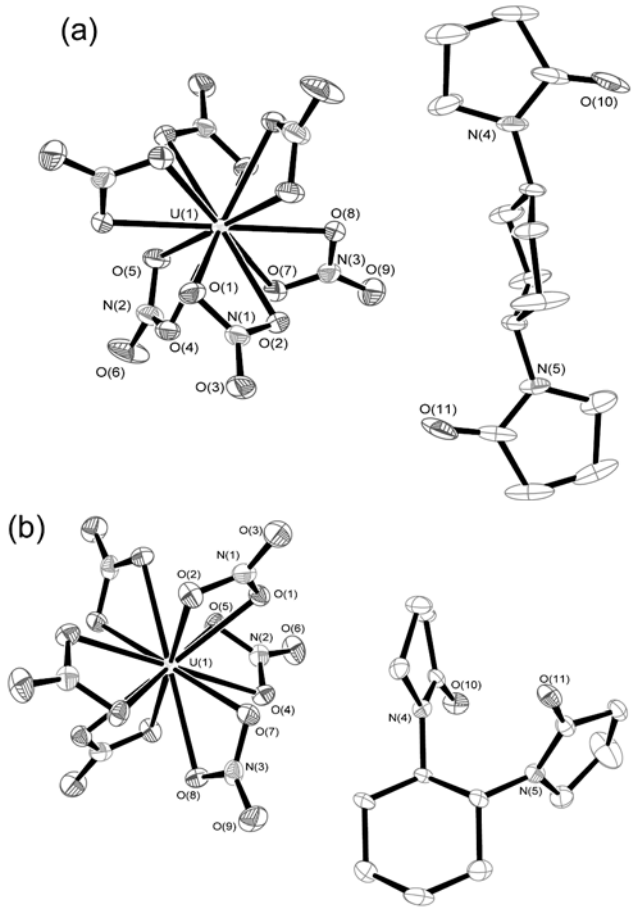

Fig. 3. ORTEP views of (a) (H**L1**)$_2$[U(NO$_3$)$_6$] (**1**) and (b) (H**L2**)$_2$[U(NO$_3$)$_6$] (**2**) at the 50% probability level. H and disordering C atoms are omitted for clarity. Both (*R*, *R*)- and (*S*, *S*)-enantiomers of **L2** are present in the crystal structure of **2** to make it racemic, although only the (*R*, *R*)-form is displayed here.

Molecular and crystal structures of **1** and **2** have been determined by single crystal X-ray diffraction.[19, 20] The ORTEP drawings of them are displayed in Fig. 3. Consequently, these compounds were found to consist of hexanitratouranate(IV), $[U(NO_3)_6]^{2-}$, together with two H^+ and two **L** molecules in agreement with the formulae determined by the elemental analysis. The selected structural parameters are summarized in Table 1. The centre U^{4+} is dodecacoordinated by 6 bidentate NO_3^- to form a regularly T_h-symmetric $[U(NO_3)_6]^{2-}$ with a centre of inversion. The interatomic distances between U and O of NO_3^- ligands are 2.51-2.53 Å in **1** and 2.50-2.53 Å in **2**, which are similar to those found in the other $[M(NO_3)_6]^{2-}$ (M = Ce, Th, U, Np, Pu)[3-15] species reported so far. There are no other possible counter cations except for H^+ in accordance with the experimental conditions. Any isolated O atoms implying either H_3O^+ or hydrated water molecules were not found in the Fourier maps through the structure refinement process for each compounds despite its deposition from the aqueous solutions.

Location of H^+ in these crystal structures is of great interest at this stage. In the structure refinement process for each compound, a residual electron density has been found near to the carbonyl O atom, implying H^+. The final least-squares refinement after the H^+ attachment was successfully converged in both **1** and **2**. We may also make a discussion for the occurrence of H^+ in these compounds from a viewpoint of other structure-related data. In each compound, the coordination sphere of U^{4+} is fully occupied by bidentate NO_3^- to offer 12 coordination bonds in total. Accordingly, **L1** and **L2** are free from any direct coordination interactions with U^{4+} in **1** and **2**, respectively. Nevertheless, the C=O bond distances in the 2-pyrrolidone rings (1.26 Å in **1**, 1.27 Å in **2**) are slightly longer than those of free **L1** (1.23 Å) and **L2** (1.23 Å). Furthermore, the C=O stretching frequencies (1518 cm^{-1} in **1** and 1528 cm^{-1} in **2**) are clearly lower than those of free **L1** (1659 cm^{-1}) and **L2** (1675 cm^{-1}). These results indicate that the C=O moieties of **L** suffered from additional non-covalent bonds in compound **1** and **2**. It is most plausible to consider

Table 1. Structural Parameters of (H**L**)$_2$[U(NO$_3$)$_6$] (**L** = **L1** (**1**), **L2** (**2**))

	(H**L1**)$_2$[U(NO$_3$)$_6$] (**1**)	(H**L2**)$_2$[U(NO$_3$)$_6$] (**2**)
interatomic distances /Å		
U−O$_{NO3}$	2.514(2), 2.515(2), 2.518(2), 2.521(2), 2.523(2), 2.525(2)	2.499(3), 2.511(4), 2.516(4), 2.524(4), 2.525(4), 2.531(4)
C=O	C(1)−O(11) 1.261(5) C(14)−O(10) 1.255(5)	C(1)−O(10) 1.268(6) C(14)−O(11) 1.270(6)
C−N	C(1)−N(5) 1.323(4) C(14)−N(4) 1.303(5)	C(1)−N(4) 1.314(6) C(14)−N(5) 1.313(6)
H-bond parameters		
D−H dist. /Å	O(10)−H(1) 1.13	O(10)−H(1) 0.94
H···*A* dist. /Å	H(1)···O(11) 1.28	H(11)···O(10) 1.48
D···*A* dist. /Å	O(10)···O(11) 2.41	O(11)···O(10) 2.41
D−H···*A* angle /°	O(11)−H(1)···O(10) 178.3	O(11)−H(11)···O(10) 167.9

that H^+ in **1** and **2** interact with a negatively polarized O atom of the C=O moiety of **L** to afford weakening of the C=O bonds compared with the free ones. In connection with this, the C−N bonds in the amide moieties (1.30-1.32 Å in **1**, 1.31 Å in **2**) are slightly shorter than those of free **L1** (1.35 Å) and **L2** (1.35-1.36 Å). This situation is ascribed to an increase in its bond order through the induced electron delocalization.

In compound **1**, the C(1)−O(11) bond (1.261(5) Å) is not largely different from C(14)−O(10) (1.255(5) Å), implying that H^+ stays between O(10) and O(11). As a result, a 1-dimensional hydrogen bond polymer $[H^+\cdots\mathbf{L1}]_n$ is formed in **1**. In compound **2**, both C=O bond distances (C(1)−O(10), C(14)−O(11)) are close to each other. The C−N bonds in the amide groups (C(1)−N(4), C(11)−N(5)) of **2** are also quite similar to each other. These results suggest that H^+ interacts with both C=O moieties in nearly equal extents to give the 1-D hydrogen bond polymer like

$[H^{+}\cdots\mathbf{L2}]_n$ in **2**. All the related parameters in **1** and **2** (Table 1) indicate that the hydrogen bonds formed in the current compounds are *strongly covalent* (15-40 kJ·mol^{-1}) in accordance with the criteria summarized in a review by Steiner.[21] The C=O bond distances in **1** and **2** are actually longer than those in free **L1** and **L2**, but clearly indicate that these moieties still show double bonding characters rather than that of a single bond arising from the protonation to give a C−OH unit on the basis of covalent radii (C=O: 1.24 Å, C−O: 1.43 Å).[22] Indeed, any O−H stretching modes have not been detected around 3200-3500 cm^{-1} in the IR spectra of **1** and **2**.[23] Consequently, H^+ in **1** and **2** are dehydrated and stabilized by formation of the hydrogen bond polymers $[H^{+}\cdots\mathbf{L}]_n$ through crystallization of these compounds as schematically displayed in Fig. 4.

The closest contact between the U^{4+} centre and H^+ in **1** and **2** are 5.85 Å and 6.14 Å, respectively. These distances are much longer than those found in reported alkali and NH_4^+ salts of $[M(NO_3)_6]^{2-}$ (M = U, Th, Rb^+ salt: 4.66 Å, Cs^+ salt: 4.86 Å, NH_4^+ salt: 4.71 Å).[3, 9] The longer distance remarkably weakens the electrostatic attraction between $[U(NO_3)_6]^{2-}$ and counter cations. Furthermore, the positive charge of H^+ is exclusively moderated through the hydrogen bonds with **L1** and **L2**. As a result, the molecular structure of $[U(NO_3)_6]^{2-}$ remains regularly T_h-symmetric even in the crystallization driven by the ionic interactions.

Despite having the same $[U(NO_3)_6]^{2-}$ anion complex, colour of U(IV) is remarkably diminished in both **1** and **2**, while $(NPr_4)_2[U(NO_3)_6]$ are clearly green-coloured as shown in Fig. 2. Essentially, the f-f transitions in $5f^2$ electronic configuration of U^{4+} is forbidden by Laporte selection rule, which is still applicable in a centrosymmetric system like the regularly T_h-symmetric $[U(NO_3)_6]^{2-}$. This is the reason why the typical green colour of U^{4+} disappears in **1** and **2**. In contrast, the molecular structure of $[U(NO_3)_6]^{2-}$ is somewhat distorted in the NPr_4^+ salt, where the Laporte selection rule is no longer strictly applicable. Therefore, $(NPr_4)_2[U(NO_3)_6]$ shows the usual green colour of U^{4+}.

In order to theoretically estimate the sensitivity of the U(IV) absorption spectra related to the ligand field transitions, the electronic absorption spectra stemming from the formally Laporte forbidden f-f transitions were calculated by CASSCF/sc-NEVPT2 approach using ORCA program.[24] Four complexes have been selected; $[U(H_2O)_8]^{4+}$,[25] $[U(H_2O)_9]^{4+}$,[25] $[U(NO_3)_6]^{2-}$ (from Crawford et al.,[9] referred as **C**) and $[U(NO_3)_6]^{2-}$ (from **1** obtained in this work, referred as **K**). The first two complexes were included as references since the absorption spectra of U^{4+} hydrates are widely available. For U^{4+} hydrates, the experimental absorption spectrum[26] is nicely reproduced by CASSCF calculations, although transition energies are overall somewhat overestimated, *i.e.*, blue-shifted. This is presumably because of using an isolated highly charged cation and thereby overestimating the effective positive charge on the uranium centre. Closer look into the CASSCF results reveals that the electronic transitions to $^3P_2$, $^1I_6$ states show up at around 350 to 450 nm, whereas $^3P_1$, $^3P_0$, $^1D_2$, and $^1G_4$ states are observed at around 550 to 600 nm. These absorption bands contribute to the greenish colour of aqueous U(IV) solution. Remind that only the states stemming from $5f^2$ configuration are included in the calculations and neither 5f → 6d transition nor the LMCT states are included here. By contrast, there is by far much weaker absorption in $[U(NO_3)_6]^{2-}$ complexes. Especially, in the case of the regularly T_h-symmetric $[U(NO_3)_6]^{2-}$ complex (**K**) synthesized in this work, there is no absorption at all throughout the whole spectral range. This situation is exclusively related to the strict preservation of the centrosymmetry of $[U(NO_3)_6]^{2-}$, and is the reason why compound **1** and **2** do not show the typical green colour of U^{4+} as shown in Fig. 2. The intensities experimentally observed in the solid state absorption spectra of **1** and **2** should be ascribed to perturbation from the centrosymmetry of $[U(NO_3)_6]^{2-}$ through thermal vibrations.

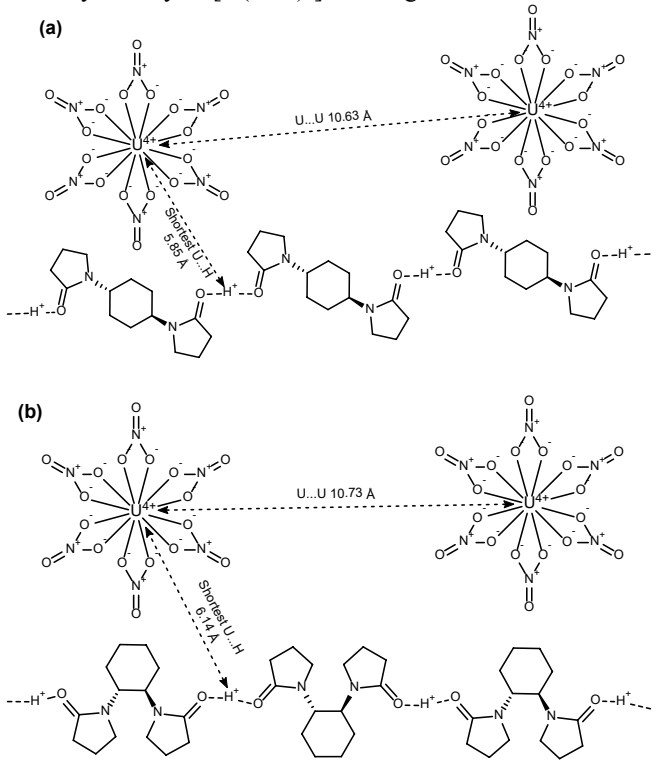

Fig. 4. Schematic structures of $[U(NO_3)_6]^{2-}$ and $[H^{+}\cdots\mathbf{L}]_n$ hydrogen bond polymer in **1** (a) and **2** (b).

In conclusion, the regularly T_h-symmetric $[U(NO_3)_6]^{2-}$ was successfully crystallized together with the anhydrous H^+-involving hydrogen bond polymers even in the aqueous systems. The diamide building blocks, **L1** and **L2**, employed here have been originally designed by our group to develop precipitation-based simple reprocessing processes for the spent nuclear fuels.[16-18, 27, 28] As described above, compound **1** and **2** have been obtained from the HNO_3 aq in nearly quantitative yields, so that the current findings can also be applied to the efficient recovery of An^{4+} from the feed HNO_3 solution in the spent nuclear fuel reprocessing.

3. Experimental

Caution! *^{238}U is an alpha emitter, and therefore standard precautions for handling radioactive materials should be followed.*

Characterization of (H**L1**)$_2$[U(NO$_3$)$_6$] (**1**). Anal. Calcd for $C_{28}H_{46}N_{10}O_{22}U$: C 30.22, H 4.17, N 12.59. Found: C 29.87, H 4.19, N 12.30. Crystallographic data for **1**: fw = 1112.75, 0.414 × 0.300 × 0.286 mm^3, monoclinic, *C*2/c (No.15), a = 18.1738(6) Å, b = 11.0137(3) Å, c = 21.8047(7) Å, β = 109.958(8)°, V = 4102.3(3) Å^3, Z = 4, T = 123 K, D_{calcd} = 1.802 g·cm^{-3}, μ = 40.54 cm^{-1}, GOF = 1.082, R ($I > 2\sigma$) = 0.0228, wR (all) = 0.0549. IR (ATR, cm^{-1}) 1518 ($\nu_{C=O}$), 1286 (NO$_3^-$).

Characterization of (H**L2**)$_2$[U(NO$_3$)$_6$] (**2**). Anal. Calcd for $C_{28}H_{46}N_{10}O_{22}U$: C 30.22, H 4.17, N 12.59. Found: C 30.12, H 4.10, N 12.27. Crystallographic data for **2**: fw = 1112.75, 0.335 × 0.276 × 0.266 mm^3, monoclinic, $P2_1/n$ (No.14), a = 9.8222(4) Å, b = 10.7334(4) Å, c = 19.5516(8) Å, β = 103.185(7)°, V = 2006.89(15) Å^3, Z = 2, T = 123 K, D_{calcd} = 1.841 g·cm^{-3}, μ = 41.43 cm^{-1}, GOF = 1.078, R ($I > 2\sigma$) = 0.0433, wR (all) = 0.0821. IR (ATR, cm^{-1}) 1512 ($\nu_{C=O}$), 1288 (NO$_3^-$).

Acknowledgements

This work is the result of "Fundamental Study on Simple Reprocessing Method for Spent Thorium Fuels by Using Uranium-Selective Precipitant" (Project ID: 271501) entrusted to Tokyo Institute of Technology by MEXT, Japan. Quantum-chemical calculations were performed at the Center for Information Services and High Performance Computing (ZIH) at the Technische Universität Dresden, Germany, using the library program ORCA.

Reference

1 L. R. Morss, N. M. Edelstein, J. Fuger, *The Chemistry of the Actinide and Transactinide Elements*. 4th ed., Springer, Dordrecht, The Netherlands, **2011**.
2 M. Benedict, T. H. Pigford, H. W. Levi, *Nuclear Chemical Engineering*. 2nd ed., McGraw-Hill, United States, **1981**.
3 G. B. Jin, J. Lin, S. L. Estes, S. Skanthakumar, L. Soderholm, *J. Am. Chem. Soc.* **2017**, *139*, 18003.
4 M. Wang, B. Wang, P. Zheng, W. Wang, J. Lin, *Acta Crystallogr.* **1988**, *C44*, 1913.
5 N. N. Rammo, K. R. Hamid, B. A. Khaleel, *J. Less Common Met.* **1990**, *162*, 1.
6 M. R. Spirlet, J. Rebizant, C. Apostolidis, B. Kanellakopulos, E. Dornberger, *Acta Crystallogr.* **1992**, *C48*, 1161.
7 G. E. Sigmon, P. C. Burns, *J. Solid State Chem.* **2010**, *183*, 1604.
8 J. Rebizant, C. Apostolidis, M. R. Spirlet, G. D. Andreetti, B. Kanellakopulos, *Acta Crystallogr.* **1988**, *C44*, 2098.
9 M. J. Crawford, A. Ellern, K. Karaghiosoff, P. Mayer, *Inorg. Chem.* **2009**, *48*, 10877.
10 M. S. Grigor'ev, B. F. Gulev, N. N. Krot, *Radiokhimiya,* **1986**, *28*, 685.
11 M. S. Grigor'ev, A. I. Yanovskii, N. N. Krot, Y. Y. Struchkov, *Radiokhimiya,* **1987**, *29*, 574.
12 P. G. Allen, D. K. Veirs, S. D. Conradson, C. A. Smith, S. F. Marsh, *Inorg. Chem.* **1996**, *35*, 2841.
13 S. D. Reilly, B. L. Scott, A. J. Gaunt, *Inorg. Chem.* **2012**, *51*, 9165.
14 S. D. Conradson, K. D. Abney, B. D. Begg, E. D. Brady, D. L. Clark, C. den Auwer, M. Ding, P. K. Dorhout, F. J. Espinosa-Faller, P. L. Gordon, R. G. Haire, N. J. Hess, R. F. Hess, D. W. Keogh, G. H. Lander, A. J. Lupinetti, L. A. Morales, M. P. Neu, P. D. Palmer, P. Paviet-Hartmann, S. D. Reilly, W. H. Runde, C. D. Tait, D. K. Veirs, F. Wastin, *Inorg. Chem.* **2004**, *43*, 116.
15 U. Casellato, P. A. Vigato, M. Vidali, *Coord. Chem. Rev.* **1981**, *36*, 183.
16 K. Takao, K. Noda, Y. Morita, K. Nishimura, Y. Ikeda, *Cryst. Growth Des.* **2008**, *8*, 2364.
17 K. Takao, Y. Ikeda, H. Kazama, *Ener. Proc.* **2017**, *131*, 157.
18 H. Kazama, S. Tsushima, Y. Ikeda, K. Takao, *Inorg. Chem.* **2017**, *56*, 13530.
19 CrystalStructure 4.2.7, Crystal Structure Analysis Package; Rigaku Corporation, Tokyo, Japan, **2017**.
20 G. M. Sheldrick, *Acta Crystallogr.* **2015**, *A71*, 3.
21 T. Steiner, *Angew. Chem. Int. Ed.* **2002**, *41*, 48.
22 P. Atkins, T. Overton, J. Rourke, M. Weller, F. Armstrong, *Shriver & Atkins' Inorganic Chemistry*. 5th ed., Oxford University Press, Oxford New York, **2010**.
23 K. Nakamoto, *Infrared and Raman Spectr of Inorganic and Coordination Compounds, Part B: Applications in Coordination, Organometallic, and Bioinorganic Chemistry*. 6th ed., John Wiley & Sons, Inc., Hoboken, New Jersey, USA, **2008**.
24 F. Neese, *WIREs Comput. Mol. Sci.* **2018**, *8*, e1327.
25 N. Koshino, Y. Kachi, T. R. Varga, A. C. Benyei, M. Shiro, K. Takao, Y. Ikeda, *Inorg. Chim. Acta* **2009**, *362*, 3433.
26 A. Kirishima, T. Kimura, O. Tochiyama, Z. Yoshida, *Chem. Commun.* **2003**, 910.
27 N. Koshino, M. Harada, Y. Morita, T. Kiikuchi, Y. Ikeda, *Prog. Nucl. Energy,* **2005**, *47*, 406.
28 Y. Morita, K. Takao, S.-Y. Kim, Y. Kawata, M. Harada, M. Nogami, K. Nishimura, Y. Ikeda, *J. Nucl. Sci. Technol.* **2009**, *46*, 1129.

C. Global Nuclear Security Division

C.1 An innovative fast reactor core design for rapid reduction of separated Pu and its proliferation concerns

Shigeki Shiba and Hiroshi Sagara

1. Overview

Continuous research and development (R&D) efforts in prospering new verification tools are essential to improve verification capacity in safeguards. The International Atomic Energy Agency (IAEA) Safety Department Long-Term R&D Plan 2012–2023 focused on more delicate and few intrusive solutions to current nondestructive assay (NDA) tools to conduct a partial defect test on a spent fuel assembly. Currently, as a promising candidate for a solution, passive gamma emission tomography (PGET) has been developed to detect the substitute of a single fuel rod in a light-water reactor and is being studied to check the number of fuel pins in a spent nuclear fuel assembly (**Fig.1**). Fuel pins appear as bright spots in a reconstructed image using PGET, and missing-pin positions appear as dark regions.

Median root prior expectation maximization (MRPEM) algorithm that belongs to the Bayesian iterative approximation is used in PGET to reconstruct passive gamma emitter distribution. The algorithm converges slowly and may involve iterations of 50–200. Fast processing of the algorithm was integrated into MRPEM to accelerate the convergence. Then, the integrated MRPEM reconstructed a passive distribution of gamma emissions within a mock-up boiling water reactor (BWR)-type 10 × 10 fuel assembly. It was found that the reconstructions in GET using the integrated MRPEM could result in a 20% reduction in the mean absolute error (MAE) compared to the standard MRPEM.

As results, fast reconstruction algorithm was successfully integrated into MRPEM, and then the passive gamma emitter distribution was rebuilt using sinogram data of 10 × 10 BWR mock-up fuel assembly. Compared to standard MRPEM, the integrated MRPEM made it possible to achieve 20% reduced MAE spatial distributions of passive gamma-ray intensity. With $W(\eta_j)$, the fast reconstruction processing led to reduce of iteration number for the GET using MRPEM, which also suppressed noise components except for ^{60}Co pin regions. However, it was found that MAEs in reconstructed distributions might increase slightly after 30 iterations due to η_j in $W(\eta_j)$ (**Fig. 2**). Thus, passive gamma-ray distributions could be recreated within 10 iterations after using $W(\eta_j)$ was introduced into the MRPEM algorithm.

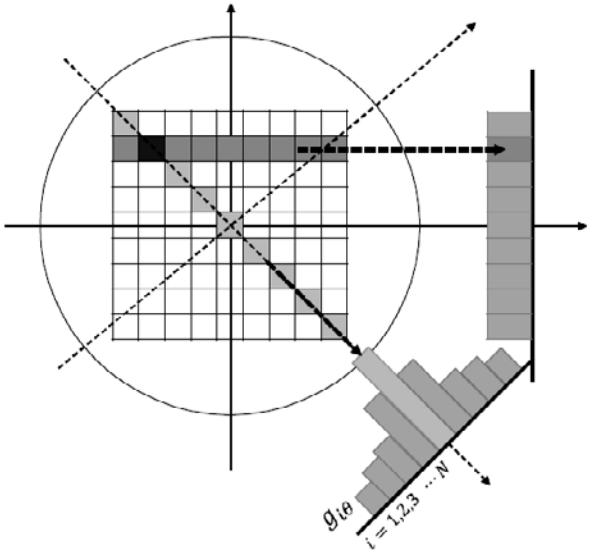

Fig. 1 Principle of tomographic acquisition and geometric considerations [1]

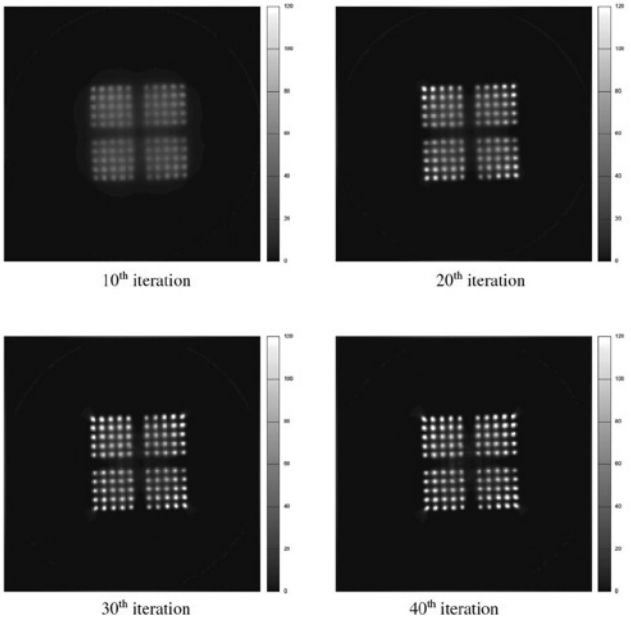

Fig. 2 The relative intensity distribution of ^{60}Co using the integrated MRPEM. (Iteration number:10, 20, 30 and 40) [1]

Reference

1. Shigeki Shiba and Hiroshi Sagara, Fast reconstruction of Bayesian iterative approximation in passive gamma-ray tomography, Volume 57, No. 5, Pages 546-552, 2019.

C.2 Material attractiveness evaluation of inert matrix fuel for nuclear security and non-proliferation

Takeshi Aoki, Hiroshi Sagara and Chi Young Han

1. Overview

The material attractiveness of inert matrix fuel (IMF) was evaluated for states and non-state actors aiming for a nuclear explosive device manufacturing in the High Temperature Gas-cooled Reactor (HTGR) system using Trans-Uranium (TRU) oxide target to reveal the impact of its chemical stability.

The methodology for material attractiveness evaluation was developed to assess material attractiveness for states and treat IMF which is chemically inert for nitric acid solution (**Fig.1**). For the material attractiveness evaluation for non-state actors revealed that non-irradiated TRISO fuel particles and IMF kernels in the fuel cycle using IMF in the HTGR, and the non-irradiated Mixed Oxide (MOX) powder in the fuel cycle using MOX fuel in Light Water Reactor (LWR) (**Fig. 2**) were the most vulnerable targets. The TRISO fuel particle and the IMF kernel had less material attractiveness than the MOX powder for use because of their greater processing time and complexity due to their chemical stability (**Fig. 3**). Even assuming a 10 wt% of plutonium extraction from the chemically stable IMF kernel, these still have less material attractiveness because approximately 10 times more net weight would be required in the acquisition phase. The irradiated fuel in HTGR had lower material attractiveness than unirradiated one because of higher decay heat hindering Nuclear Explosive Device (NED) manufacturing in the utilization phase.

The evaluation of material attractiveness for states assuming the concealed diversion of declared material reveal that nonirradiated TRISO fuel particles and IMF kernels, the nonirradiated MOX powder were the most vulnerable targets in each fuel cycle. The TRISO fuel particle and the IMF kernel had less material attractiveness as a target than the MOX powder because of their greater conversion time due to their chemical stability, and were regarded as irradiated uranium fuel grade in material attractiveness. The irradiated fuel in the HTGR had lower material attractiveness than unirradiated one because of high decay heat generation hindering NED manufacturing and its nominal yield generation in the utilization phase.

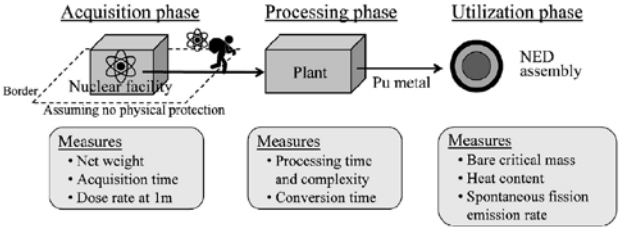

Fig. 1 Discrete phases in NED development and relevant measures applied in each phase[1].

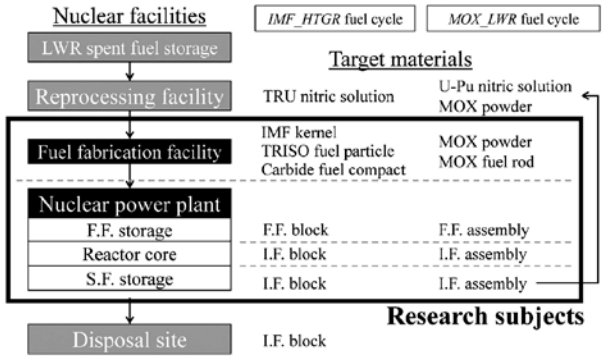

Fig. 2 Target materials in the nuclear fuel cycle for two process flows: the IMF use in a HTGR and the MOX fuel use in a LWR [1].

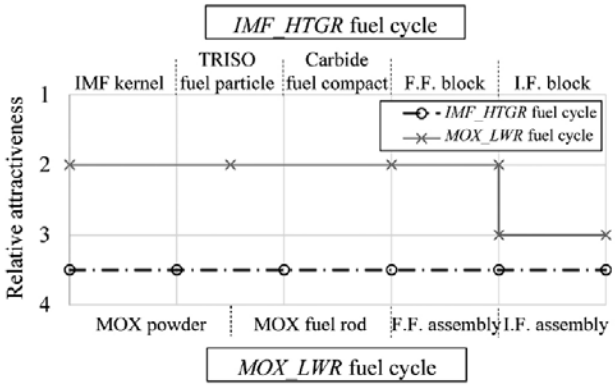

Fig. 3 Relative attractiveness for the processing phase [1]

Reference

1.Takeshi Aoki, Hiroshi Sagara, Chi Young Han: Material attractiveness evaluation of inert matrix fuel for nuclear security and non-proliferation; Annals of Nuclear Energy, Volume 126, 2019, Pages 427-433.

C.3 Densification of Yttrium Oxyfluoride Ceramics by Rate Controlled Sintering and Their Mechanical Properties

Katsumi Yoshida, Riku Akatsu, Toru Tsunoura, Anna Gubarevich

1. Introduction

Semiconductor manufacturers are improving yields and operating time of manufacturing to reduce the cost of large scale integrated (LSI) chip. If the yields are reduced, a semiconductor manufacturer cannot keep manufacturing or start to manufacture new semiconductor devices. However, the yields have recently decreased as semiconductor devices have been higher integrated. There are many causes of yield reduction. Particulate contamination on a wafer in the etching process is currently the most important issue among them. Fluorocarbon plasmas have been extensively used in the semiconductor industry to etch silicon wafers. However, chamber walls are also eroded by the fluorocarbon plasmas. Particles are generated from the surfaces of the plasma chamber in the manufacturing equipment. Therefore, the chamber walls need to be coated with corrosion-resistant materials such as silicon, silica, alumina (Al_2O_3) and yttria (Y_2O_3). They are conventional corrosion-resistant materials for the plasma processing equipments. The Y_2O_3 and Al_2O_3 coatings exposed to CF_4 plasma form fluorinated layer such as AlF_3 and YF_3. These AlF_3 and YF_3 act as the protective layer to prevent the surface from further erosion with fluorocarbon plasma. Therefore yttrium fluoride (YF_3) coating with high chemical stability under fluorocarbon plasma was proposed as a new candidate material for plasma processing equipments. Our previous study showed that YOF ceramics sintered by hot-pressing had superior resistance against fluorine-plasma exposure as compared with the Y_2O_3 ceramics.[1] Therefore yttrium oxyfluoride ($Y_xO_yF_z$) ceramics can be considered as a next-generation corrosion-resistant material. However, YOF ceramics are difficult to handle industrially, because YOF ceramics have a high sintering temperature of around 1600°C and a phase transition between the rhombohedral and tetragonal phases at around 560°C.[2] On the other hand, $Y_5O_4F_7$ and YF_3 ceramics have low sintering temperatures and no phase transition under 1000°C.[2] Moreover, $Y_5O_4F_7$ + YF_3 ceramics show approximately equivalent mechanical properties to YOF ceramics due to the dispersion strengthening.[2] Therefore, we have paid attention to the $Y_5O_4F_7$ + YF_3 ceramics.

There are several sintering methods for ceramics. Pressureless-sintering is conventional method to fabricate ceramic parts of complicated shapes, compared with hot-pressing. However, it is difficult to densify ceramics by pressureless-sintering. It was found that, for many ceramic materials, the high rate of shrinkage and densification can be realized by using a low heating rate. On the other hand, for industrial applications, fast heating programs for sintering processes are required to save time and energy. As a method to solve this problem, a rate controlled sintering (RCS) is known. RCS is defined as a sintering method with a controlled heating rate in this study. In RCS, fast heating rates when no shrinkage occurs and low heating rates when shrinkage and densification are facilitated are combined. Ceramics show densification behavior with a constant shrinkage rate by RCS. It is reported that grain growth of ceramics is suppressed by RCS. It is also possible that size and number of pores are reduced by RCS, compared with a constant heating rate sintering (CHRS). From these reports the improvement of mechanical properties of ceramics sintered by RCS method can be expected.

In this study, densification behavior of the $Y_5O_4F_7$ + YF_3 ceramics by pressureless-sintering was evaluated with a dilatometer and a RCS temperature program was determined based on the thermal measurements. The $Y_5O_4F_7$ + YF_3 ceramics were pressureless-sintered according to the heating program and their mechanical properties were evaluated.

2. Experimental Procedures

2.1. Shrinkage Behavior of $Y_5O_4F_7$ + YF_3 Ceramics and Thermokinetic Analysis

Mixture of $Y_5O_4F_7$ + YF_3 powder (Nippon Yttrium Co. Ltd., Japan, oxygen content: 6 wt%, median particle size: 0.7 μm) was used as starting materials. Green bodies were prepared under a uniaxial pressure of 10 MPa, and then they were pressed under cold isostatic pressing (CIP) of 200 MPa for 1 min. The size of the green bodies was 5 × 5 × 15 mm^3. The shrinkage behavior of the ceramics was measured with a dilatometer. Green bodies were put between thin graphite plates on graphite sample carrier. Shrinkage measurements were carried out at different heating rates of 5 °C/min, 10 °C/min and 20 °C/min under He flow. Thermokinetic analysis to obtain a RCS temperature program was conducted using a software (ThermoKinetics3.1, NETZSCH). Sintering of ceramics contains several different reactions and each reaction is independent, subsequent or parallel to other reactions. Reaction model of ceramics samples can be estimated from the results of dilatometry. Based on the reaction model, the parameters of the reaction model can be optimized using the thermokinetic software by multivariate nonlinear regression. RCS temperature program can be calculated using the reaction model and kinetic parameters.

The best reaction model and kinetic parameters were determined with the software based on the shrinkage behavior of $Y_5O_4F_7$ + YF_3 ceramics at different heating rates. Then RCS temperature program for $Y_5O_4F_7$ + YF_3 ceramics was calculated and the shrinkage behavior of $Y_5O_4F_7$ + YF_3 ceramics was actually measured with a dilatometer according to the RCS temperature program.

2.2. Fabrication of $Y_5O_4F_7$ + YF_3 Ceramics

Green bodies were prepared in the same way described in Section 2.1. The diameter of the green bodies was 60 mm. The green bodies were sintered under Ar flow using two different temperature programs, shown in Fig. 1. One temperature program was RCS temperature program calculated in Section 2.1. Another program was the temperature program with a constant heating rate. The temperature was raised to 930 °C at the rate of 30 °C/min and kept at 930 °C for 1 h.

2.3 Mechanical Properties

The specimens ($3^t \times 4^w \times 35^l$ mm^3) were mirror-polished with diamond slurry. Their bulk density and open porosity were measured by Archimedes method according to JIS-R1634. To measure the grain size of samples, the mirror-polished specimens were thermally etched in Ar flow. The temperature was raised to 830 °C at the rate of 30 °C/min and kept at 830 °C for 1 h. The surface of $Y_5O_4F_7$ + YF_3 ceramics after thermal etching was observed by scanning electron microscopy (SEM) after they were coated with a thin Pt–Pd layer with a sputtering apparatus. The grain size was measured from SEM images. The three-point bending strength of specimens fabricated by CHRS and RCS was measured at room temperature using a testing machine according to JIS-R1601. Observation of fracture surface of bended specimens was conducted using SEM after they were coated with a thin Pt–Pd layer. Micro-Vickers hardness tests were carried out at room temperature with an applied load of 4.904 N for 15 s according to JIS-R1610.

3. Results and Discussion

3.1. Shrinkage Behavior of $Y_5O_4F_7$ + YF_3 Ceramics

Figure 2 shows shrinkage behavior of $Y_5O_4F_7$ + YF_3 ceramics under the heating rates of 5 °C/min, 10 °C/min and 20 °C/min. From the results, fittings were attempted using nonlinear regression with several kinetic models, and the best reaction model with four competing reactions was chosen. The RCS temperature program was calculated based on the reaction model and parameters, shown by the solid line in Fig. 1. Figure 3 shows the comparison between calculated and experimental shrinkage behavior, and the RCS temperature program of $Y_5O_4F_7$ + YF_3 ceramics. The experimental shrinkage behavior almost agreed with the calculated shrinkage behavior.

3.2. Mechanical Properties of $Y_5O_4F_7$ + YF_3 Ceramics

The theoretical densities of $Y_5O_4F_7$ and YF_3 are 5.14 and 5.06 g/cm^3 from ICDD 00-025-1012 and ICDD 01-070-1935, respectively. Thus, theoretical density of $Y_5O_4F_7$ + YF_3 ceramics was calculated as 5.11 g/cm^3, and their relative density was calculated. Every relative density was more than 95 % and open porosity was less than 1 %. These results show that $Y_5O_4F_7$ + YF_3 ceramics were enough densified by CHRS and RCS. The closed porosity of $Y_5O_4F_7$ + YF_3 ceramics obtained by RCS was approximately three times smaller than that obtained by CHRS and approached to that sintered by hot-pressing. That is, RCS, in spite of pressureless-sintering, enabled $Y_5O_4F_7$ + YF_3 ceramics to be densified almost equivalently to hot-pressing. This result implies that pores of ceramics bulk might be confined inside during CHRS when ceramics are densified. On the other hand, pores might be released outside during RCS due to slower densification.

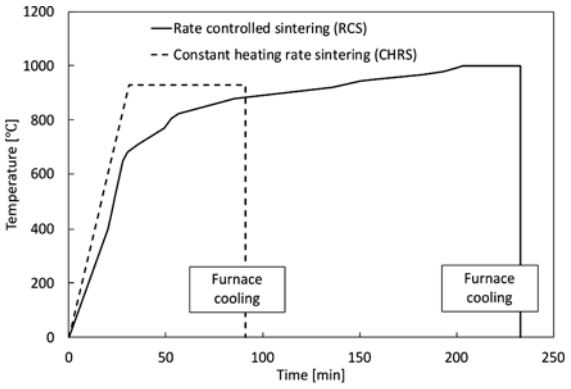

Fig. 1 Two kinds of temperature programs of $Y_5O_4F_7$ + YF_3 ceramics used in this study.

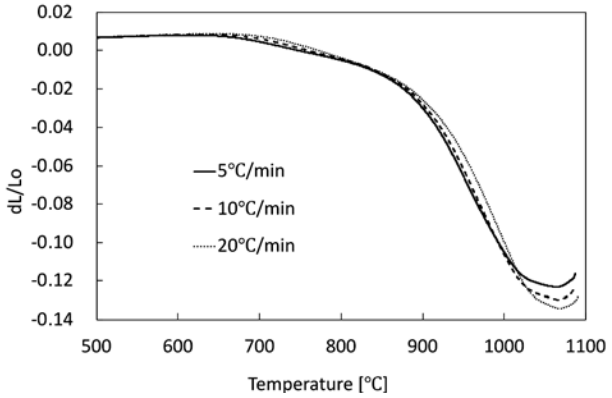

Fig. 2 Shrinkage behavior of $Y_5O_4F_7$ + YF_3 ceramics with the heating rates of 5 °C/min, 10 °C/min and 20 °C/min.

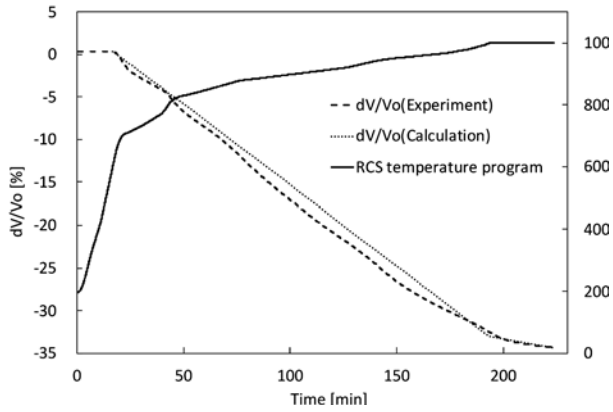

Fig. 3 The comparison between calculated and experimental shrinkage behavior, and the RCS temperature program of $Y_5O_4F_7$ + YF_3 ceramics.

Figure 4 shows SEM images of surface of $Y_5O_4F_7$ + YF_3 ceramics after thermal etching. The median grain size of CHRS and RCS samples was 0.85 μm and 0.89 μm, respectively. In other words, the grain size of CHRS sample

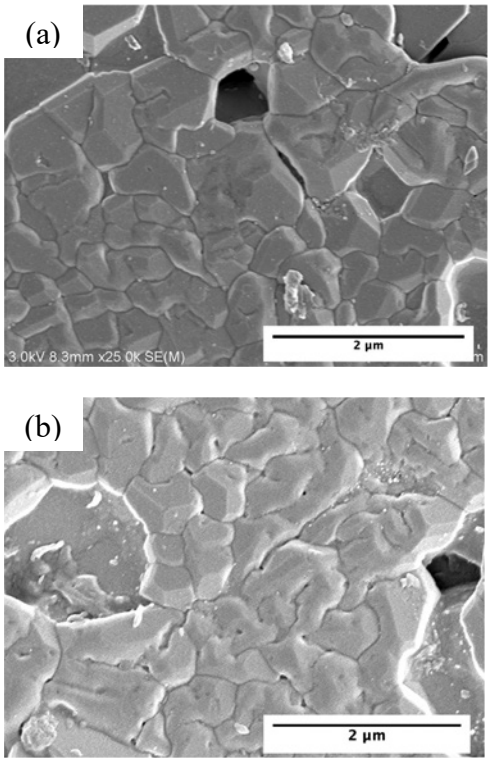

Fig. 4 SEM images of surface of $Y_5O_4F_7 + YF_3$ ceramics sintered by (a) CHRS and (b) RCS after thermal etching.

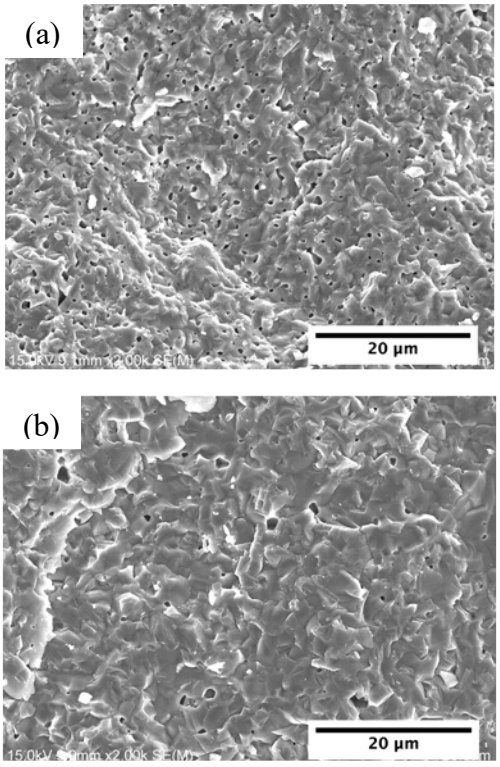

Fig.5 SEM images of fracture surface of $Y_5O_4F_7 + YF_3$ ceramics sintered by (a) CHRS and (b) RCS after three-point bending test.

was smaller than that of RCS sample. This result indicates that grain growth was caused by prolonged heating under RCS.

$Y_5O_4F_7 + YF_3$ ceramics prepared by RCS showed better mechanical properties than those sintered by CHRS. Moreover, $Y_5O_4F_7 + YF_3$ ceramics sintered by RCS showed superior bending strength compared to the ceramics prepared by CHRS and hot-pressing. $Y_5O_4F_7 + YF_3$ ceramics sintered by RCS showed lower Vickers hardness than that densified by hot-pressing. However, as a result, through application of RCS, Vickers hardness of presureless-sintered $Y_5O_4F_7 + YF_3$ ceramics can approach the value of the samples sintered by hot-pressing.

Figure 5 shows SEM images of fracture surface of the $Y_5O_4F_7 + YF_3$ ceramics after three-point bending test. As seen in Fig. 6, the grain size of CHRS samples seems to be smaller than that of RCS sample. On the other hand, a larger number of pores was observed on the cross-section of $Y_5O_4F_7 + YF_3$ ceramics prepared by CHRS, compared with RCS sample. Existence of a large number of these pores in the CHRS sample agrees with the value of porosity. It is known that the strength of ceramics decreases as the porosity increases. It can be the reason why $Y_5O_4F_7 + YF_3$ ceramics prepared by RCS were superior in bending strength to that sintered under CHRS.

The results show that mechanical properties of $Y_5O_4F_7 + YF_3$ ceramics are greatly influenced by pores in their bulk. It is considered that lower heating rate at temperature higher than 650 °C led to decreased porosity in RCS samples compared with CHRS samples. It means that $Y_5O_4F_7 + YF_3$ ceramics sintered at lower heating rate may have smaller porosity. However, setting low heating rate from room temperature means time and energy-consuming process. Thermokinetic analysis permits to define optimal heating rate and perform efficient sintering.

4. Conclusion

The $Y_5O_4F_7 + YF_3$ ceramics were sintered at an almost constant shrinkage rate by application of RCS temperature program. The experimental shrinkage behavior was consistent with the shrinkage behavior simulated by thermokinetic analysis in advance. The three-point bending strength of $Y_5O_4F_7 + YF_3$ ceramics densified by pressureless-sintering was higher than that sintered by hot-pressing. Sintered by RCS, $Y_5O_4F_7 + YF_3$ ceramics showed much higher bending strength than that sintered by hot-pressing. Then, $Y_5O_4F_7 + YF_3$ ceramics by RCS showed high Vickers hardness approaching to that measured for hot-pressed samples. It is concluded that the RCS represents a simple and effective method to manufacture corrosion-resistant materials with high strength.

References

1. T. Tsunoura, K. Yoshida, T. Yano, and Y. Kishi; Jpn. J. Appl. Phys., Vol. 56, 06HC02 (2017).
2. R. Tahara, T. Tsunoura, K. Yoshida, T. Yano, and Y. Kishi; Jpn. J. Appl. Phys., Vol. 57, 06JF04 (2018).

C.4 Combustion Synthesis of Ceramic Powders with Induction Heating Assistance

Anna Gubarevich, Tsubasa Watanabe, Katsumi Yoshida

1. Introduction

Current applications of ceramics in nuclear reactor systems include oxide fuels, ceramic-glassy waste compacts, graphite moderators, and B_4C control rods. Future nuclear ceramics will potentially include non-oxide fuels, fuel cladding (metal carbides, MAX phases), SiC/SiC composites, inert matrix fuel systems, ceramic superconductors and so on.

Combustion synthesis (or self-propagating high-temperature synthesis) method is well known method of synthesis of high-temperature ceramic materials. It has been applied to fabricate numerous carbides, nitrides, borides, oxides, intermetallics and so on. Combustion synthesis is based on utilization of highly exothermic chemical reactions, when the heat released during the reaction is used to promote the reaction further. In a self-propagating mode, the reaction is initiated by a high-energy pulse, such as a short-duration heating by passing electric current through tungsten filament. After ignition the reaction propagates without any additional supply of energy from outside. Calculation of the adiabatic temperature, which represents a maximum value of temperature possible to reach when all the heat released during the reaction is kept inside, can give approximate estimation of possibility of reaction propagation. When value of adiabatic temperature is not high enough (lower than 1800 K as a rule), and propagation of reaction cannot be achieved, techniques of volume combustion (or thermal explosion), chemical oven or combustion under elevated temperatures can be applied. From the other side, it is known that preheating for a long time can inhibit ignition due to partial chemical conversion of the reactants, therefore choice of the method of preheating is important. In the present research we put our attention on induction heating (IH) technique.

IH provides fast, contactless and efficient heating of conductive materials, moreover the power applied by the IH system can be carefully controlled and speed of heating can be easily varied in a wide range. The experimental set up is simple and permits to reduce time, temperature and energy necessary for synthesis.

2. Examples of synthesis

2.1. Aluminum silicon carbide Al_4SiC_4[1)]

Aluminum silicon carbide (Al_4SiC_4) has been attracting an increasing attention not only in the field of refractory and high-temperature materials due to its low density, high melting temperature, high compressive stress, good thermal conductivity, ductility and excellent oxidation resistance, but also in the fields of photocatalysis, power and optoelectronics as a new wide-gap semiconductor material. Al_4SiC_4 can be synthesized by various methods; elemental powders of Al, Si, and C or oxide powders such as Al_2O_3 and SiO_2, and C are often used as starting materials. Despite very attractive properties of Al_4SiC_4, its application is still restricted by the difficulty to fabricate single phase. Therefore, a new and effective method is highly required.

The heat of formation of Al_4SiC_4 at room temperature is relatively low (Δ_fH^0 =-203 kJ/mol), and as a result adiabatic temperature T_{ad} (300K) is only 1320 K; this value is too low to achieve self-propagation of the reaction. To the best of our knowledge, there are no reports in the literature regarding combustion synthesis of pure Al_4SiC_4 either in self-propagating or volume combustion mode. Calculations using thermodynamic data show that preheating of the starting mixture to temperatures higher than melting point of aluminum makes possible synthesis of Al_4SiC_4 from elemental powders by combustion synthesis method.

In our work, we show for the first time that single-phase Al_4SiC_4 powders can be synthesized from elemental Al, Si, and C by combustion synthesis method with IH assistance. Commercially available powders of Al, Si, and carbon black were used as starting materials. The powders were mixed by ball milling for 24 hours using silicon carbide balls as milling media and ethanol as the dispersive medium. After mixing ethanol was removed using a rotary evaporator, and the powder was dried at 60℃ for 12 hours. After drying, powders were formed into pellets by uniaxial pressing and then by cold isostatic pressing. The pellet was placed into a graphite crucible and covered with a graphite lid. The crucible was set in high-frequency induction heating (HF IH) apparatus (MU-αIV, SK Medical Electron, Japan) and heated under Ar flow. Basic set-up is shown in Fig. 1. The heating program, expressed as power of HF IH vs time, has three steps. Finally, the sample is cooled down naturally under Ar flow. To measure temperature of the samples, an infrared optical pyrometer (working range 600~3000^{0}C) focused on the top surface of the samples was used. In that case, the graphite lid was taken off. After cooling down to room temperature under Ar flow, the yellow product was obtained. Synthesized product was hand-milled in an agate mortar with pestle for the further characterization. Crystal phases of the powder were identified using X-ray diffraction (XRD). The morphology and composition of the synthesized Al_4SiC_4 powder was examined after Pt coating using scanning electron microscopy (SEM).

XRD analysis of the synthesized powders showed that a single-phase product of Al_4SiC_4 was obtained. SEM observation revealed formation of particles with size less

than 1 micron.

2.2. Boron carbide B_4C[2)]

Boron carbide has outstanding properties such as high hardness, low density, high melting point, high temperature stability, and high neutron absorption. It is commonly used in nuclear applications as a neutron absorber. Boron carbide is commercially produced by carbo-thermic reduction of boric acid or magnesiothermy in the presence of carbon. For specialized applications boron carbide is synthesized from elements. High temperatures and long duration of heating are required, and as a result, course products are formed, which are then ground to get fine particles suitable for processing and sintering. The direct reaction between boron and carbon is exothermic, but enthalpy is low, therefore combustion synthesis from elements is not self-sustainable.

In our research, we applied induction heating to develop a new facile, energy-saving and environmentally friendly method for synthesis of fine boron carbide powders.

Experimental procedure includes mixing of amorphous boron and carbon black powders in stoichiometric proportion, pressing of mixture into pellet, and then heating in HFIH furnace under Ar flow. Sintered porous bodies obtained after heating were crushed into powders and analyzed by XRD, SEM, N_2 gas adsorption and TG-DTA.

As a result, combustion reaction between B and C with formation of B_4C was confirmed. Depending of post-heating conditions B_4C powders ranging from sub-micron (0.4~0.5 micron, BET specific surface area (SSA) 5.4 m^2/g) to several microns (1~3 microns, BET SSA 1.1 m^2/g) were obtained (Fig. 2). Thermogravimetry study in air showed that the synthesized boron carbide powders showed higher onset temperature of oxidation than commercial B_4C powders.

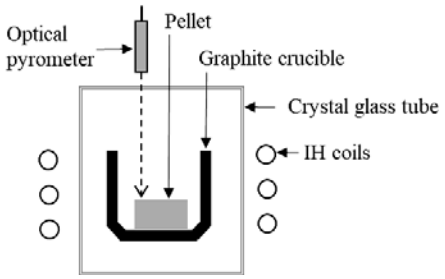

Fig. 1 Experimental setup.

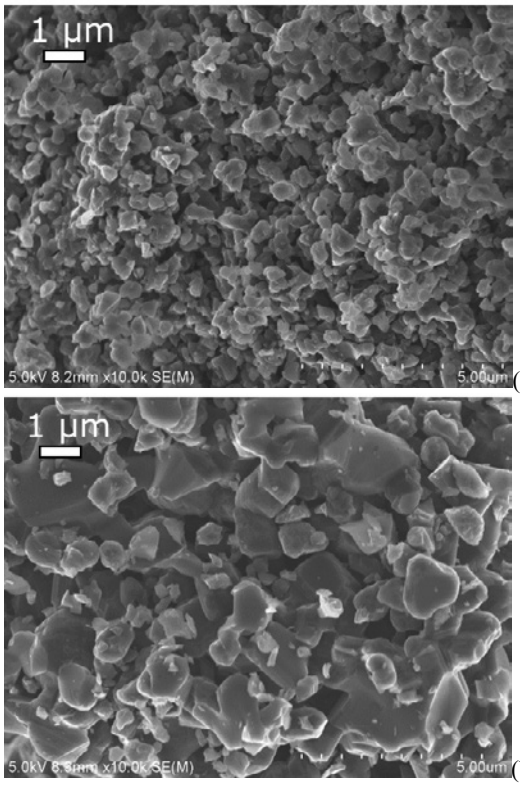

Fig. 2 SEM images of synthesized B_4C powders: (a) post-heating at 1900^0C, (b) post-heating at 1950^0C.

3. Conclusions

Combination of combustion synthesis with induction heating technique can be successfully applied for synthesis of ceramic powders with low enthalpies such as Al_4SiC_4 and B_4C. Despite the time of heating is very short (5~10 min), single-phase powders with high crystallinity can be synthesized. By varying post-heating conditions, particle size of the powders can be tuned. It is expected, that induction heating assisted combustion synthesis technique can be developed further as a promising method to synthesize various ceramic powders.

Reference

1. T. Watanabe, A. Gubarevich, K.Yoshida: The 13th Pacific Rim Conference of Ceramic Societies (PACRIM13), October 27-November 1, Okinawa, Japan, (2019).
2. A. Gubarevich, K. Yoshida: Materials Research Meeting 2019 (MRM2019), December 10-14, 2019, Yokohama, Japan (2019).

D. Advanced Medical Application Division

D.1 Time-of-Flight Laser Velocimetry for an Electromagnetically Driven Shock Tube

Yoshiyuki Oguri and Hiroki Kawada

1. Introduction

An electromagnetically driven shock tube is being developed to produce fully dissociated atomic hydrogen gas[1]. The dissociation degree is uniquely determined by the shock velocity in the tube. To measure the shock velocity precisely, we constructed a velocimeter based on time of flight (TOF) method. In this note, preliminary results on this setup are presented.

2. Experimental methods

Figure 1 illustrates a schematic of the shock velocimetry. Arrival of the shock front at two different longitudinal positions along the tube was detected by observing refraction of laser (633-nm He-Ne, 5 mW, 05-LHP-111, Melles Griot) beams induced by the shock. Si-PIN photodiodes (S5972, 500 MHz, ϕ0.8 mm, Hamamatsu Photonics) were used as the fast light sensor. The detector waveforms were recorded by a digital oscilloscope (WaveSurfer 510, 1 GHz, 10 GS/s, Teledyne LeCroy). A shock can be detected as a negative pulse in the signal waveform. To increase the sensitivity, the diameter of the laser beams in the tube were reduced using a lens system. The detectors were placed away from the tube (≈ 1 m from the final lens) to amplify the displacement of the laser beams.

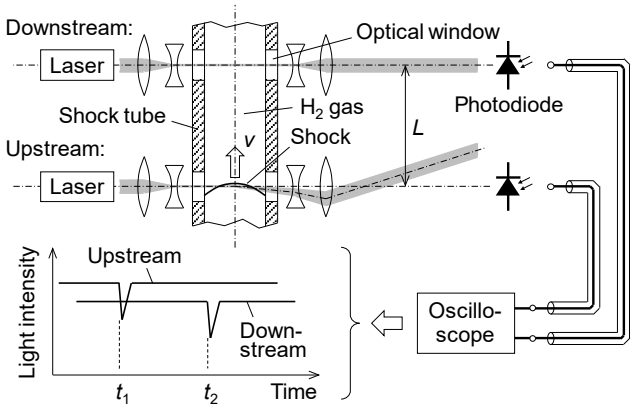

Fig. 1 Setup of the TOF laser velocimeter

The shock velocity u_s is given by

$$u_s = \frac{t_2 - t_1}{L}, \quad (1)$$

where t_1 and t_2 are the measured arrival time of the shock at the upstream- and the downstream position, respectively. The distance between the laser beams (50 mm) is denoted by L.

Details of the shock tube and the driver circuit have been reported elsewhere [Y. Hakozaki, Master thesis, Graduate Major in Nuclear Engineering, Tokyo Tech (2020)]. The total capacity of the capacitor bank was 3.52 μF. The discharge voltage was varied from 13 to 17 kV. The measurement was performed at different initial hydrogen gas pressures ranging from 400 to 1000 Pa.

3. Results and discussion

Figure 2 shows the shock velocity calculated from the measured t_1, t_2 and L at different discharge voltages and initial hydrogen gas pressures. We see the shock velocity increases with increasing the voltage. In contrast, the shock velocity is low when the pressure in the tube is high.

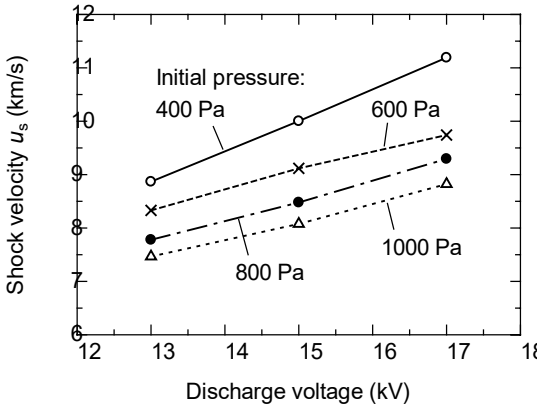

Fig. 2 Measured shock velocity as a function of the discharge voltage for different initial hydrogen gas pressures

4. Conclusions

By means of the velocimeter developed in this work, dependences of the shock speed on the discharge voltage and on the initial gas pressure were successfully measured.

This velocimeter is expected to be used for examining the performance of the shock tube after a modification of the capacitor bank in the driver circuit, where the connection between capacitors is changed so that the stray inductance is reduced and the discharge can be faster.

References

1. K. Kondo, T. Yokozuka and Y. Oguri, Laser and Particle Beams Vol. 33, pp. 679-683 (2015).

D.2 Study on Age-dependency of DNA Repair Ability Using Mice

Aoi Okawa and Yoshihisa Matsumoto

1. Background

It is generally thought that younger people, especially infants and children, are more susceptible to cancer development after exposure to ionizing radiation in reference to epidemiological studies of atomic bomb survivors of Hiroshima and Nagasaki. There are also a number of studies showing age-dependent changes in radiation-induced carcinogenesis in animal experiments.

DNA double-strand breaks (DSBs) are thought the most deleterious type of DNA damage among those induced by radiation and most intimately associated with the biological effects of radiation, including carcinogenesis. In eukaryotic cells, DSBs are repaired mainly through two pathways, i.e. non-homologous end joining (NHEJ) and homologous recombination (HR). NHEJ is generally considered less accurate than HR. Nevertheless, NHEJ has a merit of operating throughout the cell cycle, whereas HR is available only late S and G2 phases, where sister chromatids exist. The abundance of DNA repair proteins may be an important determinant of genomic stability, which in turn prevents carcinogenesis. There have been only a few studies on age-dependent alteration in DNA repair ability and the abundance of DNA repair proteins in mice.

In this study, we examined the age-dependency of the expression level of proteins that are involved in DSB repair through NHEJ, *i.e.*, DNA-dependent protein kinase catalytic subunit (DNA-PKcs), X-ray repair cross-complementing group 4 (XRCC4), and XRCC4-like factor (XLF). We focused on brain tissues, because NHEJ factors are implicated in the development of the brain.

2. Materials and methods

2.1. Mice

All animal experiments in this study were approved by the Institutional Animal Care and Use Committee of the National Institute of Radiological Sciences (NIRS), National Institutes for Quantum and Radiological Science and Technology (QST) and conducted in accordance with national and institutional guidelines. Males and female offsprings of crosses between C57BL/6NCrlCrlj female mice and C3H/HeNCrlCrlj male mice (B6C3FI) (Charles River Japan) were used for experiment.

2.2. Methods

The abundance of the proteins was measured by western blotting. The spatial distribution of the proteins was examined by immunohistochemistry. DNA repair kinetics and apoptosis induction were also examined by immunohistochemistry, using γ-H2AX and cleaved- caspase 3 as the marker.

3. Results

3.1. Differential expression of DNA-PKcs in the brain of neonatal mice and young adult mice

We first compared the expression level of NHEJ-related proteins in the brain tissues of mice at 1 week of age (1w; neonatal) and 7 weeks of age (7w; young adult) by western blotting. For each age, 2 male mice and 2 female mice were examined. It was found that the expression level of DNA-PKcs was much higher in the cerebrum and the cerebellum of 1w mice than in those of 7w mice (Fig. 1). In contrast, the expression level of XLF was higher in the cerebrum and the cerebellum of 7w mice than in those of 1w mice. The expression level of XRCC4 was not statistically different between 1w and 7w mice in the same brain regions.

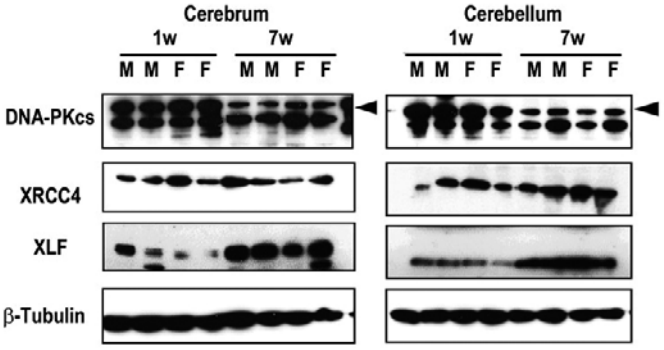

Fig. 1 Western blotting analyses of NHEJ-related proteins in the cerebrum and cerebellum of mice at different ages (ref.1).

To examine the spatial expression patterns of DNA-PKcs, sections of brain tissue were prepared from 1w and 7w mice with or without γ-ray irradiation and examined by immunostaining using anti-DNA-PKcs antibody. In agreement with the results of the above western blotting experiments, DNA-PKcs expression in the cerebrum and cerebellum was higher in 1w mice than in 7w mice (Fig. 2).

To assess the functionality of DNA-PKcs, the sections were also examined for the autophosphorylation of DNA-PKcs at Ser2056 (pS2056). Although DNA-PKcs Ser2056 phosphorylation increased after γ-ray irradiation in both of 1w and 7w mice, 1w mice exhibited higher levels of DNA-PKcs Ser2056 phosphorylation than 7w mice (Fig. 3).

2.2. Differential DNA double-strand break repair kinetics in the brain of neonatal mice and young adult mice

We next examined the kinetics of DSB repair in the brain tissues of 1w and 7w mice by immunostaining of γ-H2AX, which is a widely used DSB marker. In 1w mice, γ-H2AX declined considerably by 3 hr after irradiation (Figure 4c) and mostly diminished by 6 hr after irradiation (Figure 4d). On the other hand, in the cerebella of 7w mice, γ-H2AX was retained even 6 hr after irradiation (Figure 4j). This

observation indicated that DSBs were repaired more rapidly in the cerebella of 1w mice than in 7w mice.

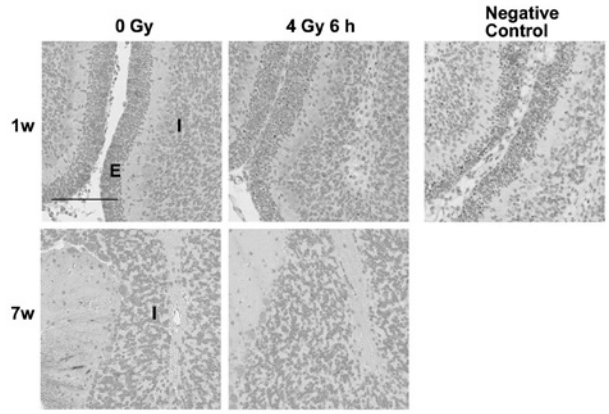

Fig. 2 Expression and spatial distribution of DNA-PKcs in the cerebellum of mice examined by immunostaining (ref.1). E: EGL, I: IGL.

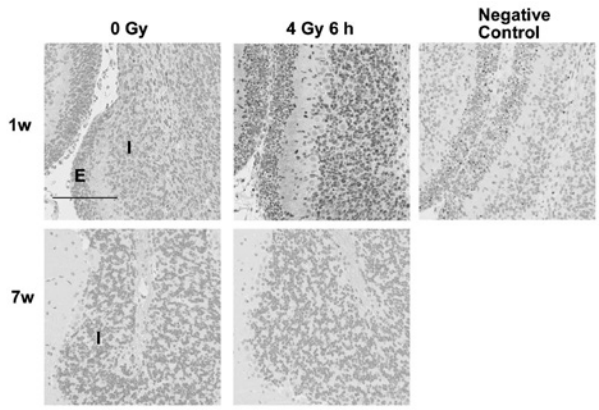

Fig. 3 DNA-PKcs phosphorylation at Ser2056 and its spatial distribution in the cerebellum of mice examined by immunostaining (ref.1). E: EGL, I: IGL.

It is also noted that, in the cerebella of 1w mice, more γ-H2AX-positive nuclei remained 3 hr after irradiation in the external granular layer (EGL) than in the internal granular layer (IGL) and that γ-H2AX increased at 12 and 24 hr after irradiation. In conjunction with this, the thickness of the EGL was considerably decreased 24 hr after irradiation. We examined the appearance of apoptosis by immunostaining of cleaved-caspase-3, which is commonly used as a marker for apoptosis. In 1w mice, cleaved-caspase-3-positive cells were seen most evidently on the outer edge of the EGL and in the middle and/or inner part of the EGL at later time points, in accordance with the distribution of γ-H2AX. This observation suggested that γ-H2AX-positive nuclei persisted in the EGL might represent cells undergoing apoptosis and most DSBs might have been repaired within 3 hr after irradiation in the EGL as well as the IGL.

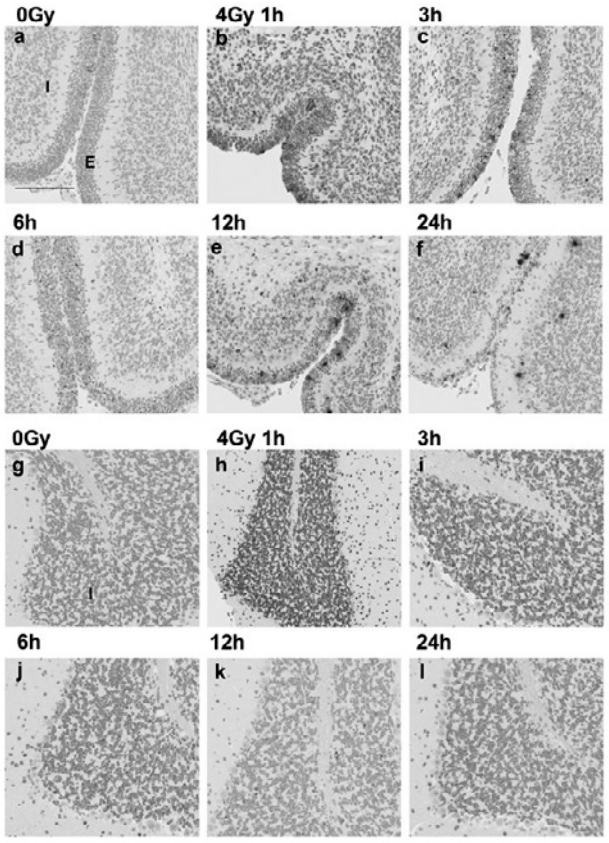

Fig. 4 Spatio-temporal kinetics of DNA double-strand breaks in the cerebellum of mice examined by γ-H2AX immunostaining. a-f, 1w mice; g-l, 7w mice (ref.1). E: EGL, I: IGL.

4. Conclusion

In this study, we demonstrated that DNA-PKcs is expressed at higher level in the brain tissues of neonatal mice than in young adult mice. Accordingly, DSBs were repaired more rapidly in the brains of neonatal mice than in the brains of young adult mice. These findings are contradictory to prevailing expectation that infants and children might be more susceptible to DNA damage and/or have lower DNA repair capability than adults, in consideration of higher susceptibility to cancer. The present finding suggested the alertness and preparedness for DNA damage in the developing neuronal system. This may be also applicable to humans and would be important in the consideration of cancer risk for radioprotection.

Acknowledgment

We are grateful to Drs. Takamitsu Morioka, Tatsuhiko Imaoka and Shizuko Kakinuma at NIRS, QST for their support and guidance.

Reference

1. A. Okawa, T. Morioka, T. Imaoka, S. Kakinuma and Y. Matsumoto. Proceedings of the Japan Academy, Series B, vol.96,171-179(2020).
(Note that Fig. 1-4 were reproduced from this publication appropriately following the guideline.)

D.3 Analysis of ionizing radiation dependent gene expression alteration in human induced pluripotent stem cells

Mikio Shimada

1. Introduction

Pluripotent stem cells (PSCs) such as embryonic stem cells (ESCs) and induced pluripotent stem cells (iPSCs) possess ability to differentiate to the all organs, and are expected to use for application of regenerative medicine. However, the presence of genetic mutation in PSCs is concern for their safe use in medical application. DNA damage response (DDR) machinery play a central role for genomic maintenance to prevent genetic mutation and aneuploidy. DDR machinery consists of DNA repair, cell cycle checkpoint, and apoptosis. Meanwhile, ionizing radiation (IR) induces several DNA damages, such as base damage, DNA single strand breaks and DNA double strand breaks. Despite there are many reports that DDR machinery is strictly regulated in PSCs, molecular mechanism of DDR machinery in PSCs remains largely unknown. In this study, to address IR dependent DDR genes expression alteration in iPSCs, we performed RNA-seq analysis using next generation sequencer.

2. Materials and Methods

2.1. Generation of iPSCs and neural stem cells

iPSCs were derived from NB1RGB by messenger RNA (mRNA) integration-free methods using the Stemgent® StemRNATM-NM Reprogramming Kit for Reprogramming Adult and Neonatal Human Fibroblasts (Stemgent, Cambridge, MA, USA). iPSC induction was performed according to the manufacturer's instructions.

NPCs were derived from iPSCs using the PSC neural induction medium (Gibco, Thermo Fisher Scientific) and maintained with a neural basal medium (Gibco, Thermo Fisher Scientific) according to the manufacturer's instructions with small modifications.

2.2. RNA sequencing

An hour after the 5 Gy IR treatment had been applied to the NB1RGB, NB1RGB C2 and NB1RGB NPCs C2, total RNA was extracted using the Fast Gene RNA premium kit (Nippon Genetics Co. Ltd., Tokyo, Japan). RNA-seq was done by Eurofins Genomics (Tokyo, Japan). For RNA-seq data analysis, FASTQ data were uploaded on the Illumina BaseSpace Sequence Hub. Gene differential expression profiles were obtained using Cufflinks Assembly & DE and indicated as fragments per kilobase of exon per million reads mapped (FPKM).

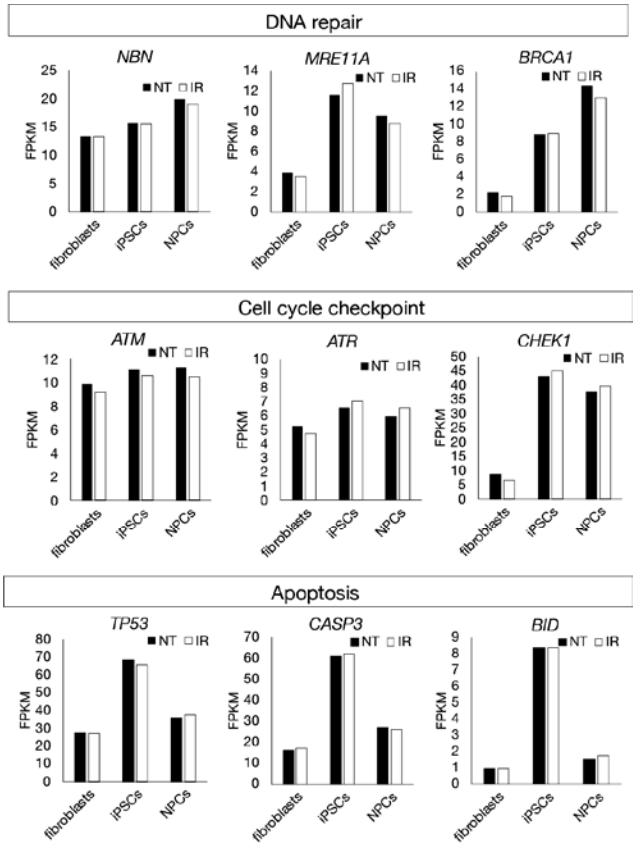

Fig. 1 Gene expression analysis in human fibroblasts, iPSCs, NPCs after IR exposure by next generation sequencer

DDR genes expression analysis by RNA -seq in human fibroblasts, iPSCs, NPCs after IR exposure. DDR pathways were classified as DNA repair, cell cycle checkpoint and apoptosis.

3. Results and Discussion

3.1. DDR in iPSCs and NPCs

To address gene expression alteration in iPSCs and PSCs after DNA damage, we established iPSCs from human neonatal skin fibroblasts NB1RGB using mRNA integration free methods. Pluripotency of iPSCs were confirmed by differentiation to the germ layer as ectoderm, mesoderm, and endoderm. NPCs were derived from iPSCs using the PSC neural induction medium.

NB1RGB, iPSCs and PSCs were exposed to the gamma ray at 5Gy and 1h after incubation, mRNA was

extracted and applied for RNA-seq analysis. Several DDR genes were highly upregulated after IR exposure in iPSCs compared with fibroblasts (Fig 1). Especially, apoptosis related genes such as TP53, CASP3 and BID were dominantly expressed. These results are consistent with high sensitivity to the IR exposure in iPSCs suggesting hyper-activation of apoptosis get rid of mutated cells from iPSCs population. Meanwhile, DNA repair and cell cycle checkpoint genes also upregulated in iPSCs. These results were consistent with protein level confirmed by western blotting analysis. Our results might be suggested that genome stability of PSCs is maintained by several DDR machinery and the cells having much DNA damage may remove from cell population for genome maintenance.

Acknowledgment

Author thanks to Dr. Matsumoto laboratory member for critical discussion and Mr. Isao Yoda for technical assistance.

Reference

1. Mikio Shimada, Kaima Tsukada, Nozomi Kagawa, Yoshihisa Matsumoto: Journal of Radiation Research, Vol. 60, No.6, pp.719-728(2019).

D.4 Investigation of Plasma Particle Dynamics in a Magnetic Nozzle by Two-dimensional Spectroscopic Imaging

Jun Hasegawa

1. Introduction

In the laser ion source, ions are extracted from a drifting source plasma, which is initially generated by pulsed laser as a tiny, dense plasma and then expanded freely into vacuum. This feature of the laser ion source has significant advantage in suppling low-emittance ion beams to high-energy accelerators. On the other hand, the source plasma density decreases rapidly accompanying with three-dimensional expansion, which makes it difficult to supply high-flux ions efficiently to the extraction gap. Although the magnetic confinement of the source plasma using a long solenoid has been tested to improve the plasma transportation, ion momentum mixing due to the Larmor motion of ions in the magnetic field obviously degrades the point-source-like feature of the laser plasma. To solve this problem, we proposed to compress the laser-produced plasma hydrodynamically and increase the ion flux by applying a magnetic nozzle to the plasma before it expands largely.

We have so far clarified that the directivity of ions in the laser-produced plasma that has passed through the magnetic nozzle is improved and the ion flux measured downstream is significantly increased [1]. On the other hand, in these previous experiments, it was difficult to investigate the effect of the magnetic nozzle on the behavior of each ion species separately. Since only ions having a specific charge-to-mass ratio are finally injected into the accelerator, it is important to observe the behavior of those ions in the magnetic nozzle. The purpose of this study is to develop a two-dimensional spectroscopic imaging system and clarify its applicability to the investigation of the behavior of ions having a specific charge.

2. Experimental Setup and Analysis Method

Figure 1 shows a schematic of a test stand for the laser ion source and the two-dimensional spectroscopic imaging system developed in this study. A plane copper target was mounted on a motorized XY linear motion stage in a vacuum chamber (~10^{-5} Pa). To produce a plasma, the target was irradiated by a frequency-doubled Nd:YAG laser (λ=532 nm, ~200 mJ, 10 ns FWHM) with an incidence angle of 30 degrees. The produced plasma expanded into vacuum in the direction perpendicular to the target surface and passed through a pulsed solenoid having an inner radius of 13 mm and a length of 1.5 mm. A divergent magnetic field was induced by driving the solenoid with an LCR circuit. The maximum field strength on the center axis of the solenoid was typically 90 mT with a driving current of 1 kA.

The plasma light was extracted in the x direction and focused by a condenser lens (f=100 mm, ø50 mm) at the entrance of an optical fiber (ø1 mm). Then it was introduced to a monochromator to observe the spectral intensity of a specific transition of atoms or ions in the plasma. The time evolution of light intensity at the outlet of the monochromator was recorded on an oscilloscope after signal amplification by a photomultiplier. Both the condenser lens and the inlet of the optical fiber were rigidly mounted on a motorized two-axis (y-z) linear motion stage to change the observation point. Figure 2 shows the positions of the laser target, the solenoid, and the observation points on the y-z plane. The solenoid was located 5 mm downstream from the target. The spectroscopic measurement was performed with respect to 209 different observation points, which were located at z = 10 to 20 mm and y = –9 to 9 mm with 1-mm spacings. At each observation point, the laser shot and measurement was repeated three times to reduce statistical errors. Ignitions of the laser and pulsed solenoid, change in observation points, and data acquisition were automatically synchronized by a computer program.

In Fig. 2, the method employed in this study to reconstruct two-dimensional distribution of emission intensity of a specific spectral line is also shown. By repeating laser plasma generation and spectroscopic measurement at each observation point, we obtain a series of waveforms corresponding to the time evolution of emission

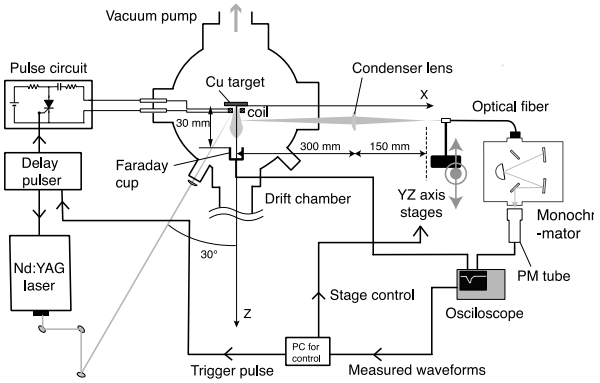

Fig. 1. A two-dimensional spectroscopic imagining system.

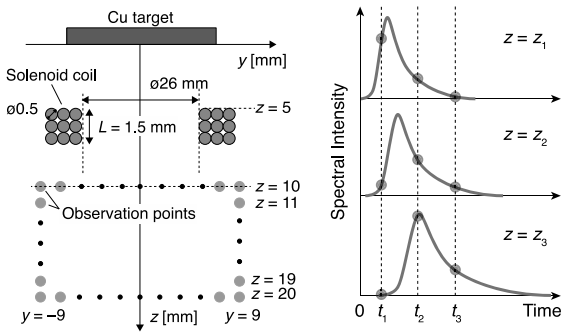

Fig. 2. Locations of observation points.

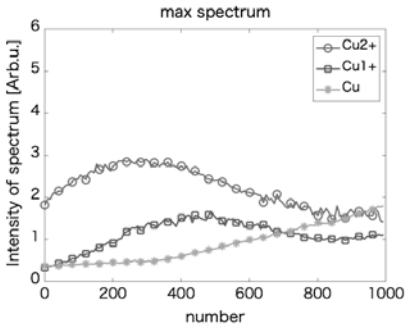

Fig. 3 Dependencies of emission intensities of Cu^{2+}, Cu^{+}, and Cu on the number of laser irradiation.

intensity as shown in Fig. 2. The observed waveform differs depending on the position of the observation point because the plasma plume expands three-dimensionally while drifting downstream. By reading the height of each waveform at a given time t_1, we reconstruct a two-dimensional distribution of emission intensity at this time. This process is repeated to obtain the snapshots for other elapsed times ($t = t_2$, t_3, ...), thereby imaging the behavior of specific atoms or ions in the plasma.

3. Results and Discussion

3.1 Reproducibility of the laser plasma

Figure 4 shows the change in the maximum value of the emission intensity (averaged for every 8 laser irradiations) of each spectral line. During the measurement, the position of the laser spot on the target was fixed. The measured spectral lines originate from Cu^{2+} (λ=437.0 nm), Cu^{+} (λ=491.0 nm), and Cu (λ=521.8 nm), respectively. From Fig. 3, one can see that the emission intensity from copper ions increases with the number of laser shots and decreases after reaching a peak at 300 to 400 shots. On the other hand, the emission from neutral atoms increases monotonically with the number of shots. Furthermore, the variation in emission intensity between shots increases with the number of shots. From the results in Fig. 4, we considered that it is possible to perform two-dimensional spectroscopic imaging with an error of about ± 10% by acquiring data when the number of laser irradiation ranges from 300 to 700. The change in plasma emission intensity with the number of laser irradiations is considered due to the change in the shape of the laser spot on the target, but it is still unclear why these tendencies were observed.

3.2 Two-dimensional spectroscopic image

The reconstructed images of emission intensity distribution of Cu^{2+} ions observed 328 ns and 408 ns after laser irradiation are compared in Fig. 5. The upper images were taken without applying a magnetic field to the magnetic nozzle, and the lower ones were taken with a maximum magnetic field of 90 mT. As shown in the figure, the plasma expands freely without a magnetic field, but when the magnetic nozzle is turned on, the plasma is strongly compressed radially. The expansion of the plasma in the axial direction also seems to be suppressed. This is a result that was not particularly observed in the previous

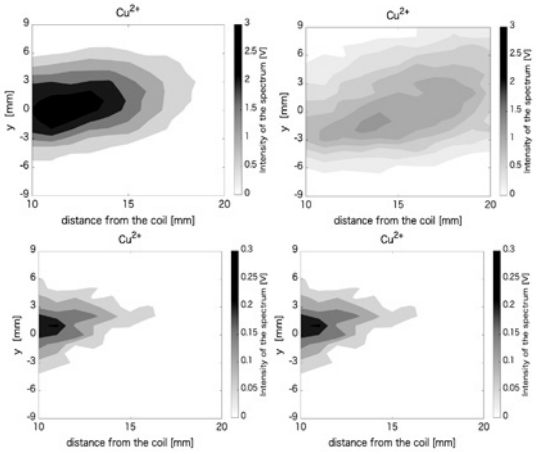

Fig. 4 Typical time evolution of emission intensity distribution of Cu^{2+} ions without magnetic field (top) and with a magnetic field of 90 mT (bottom). Elapsed times are 328 ns (left) and 408 ns (right).

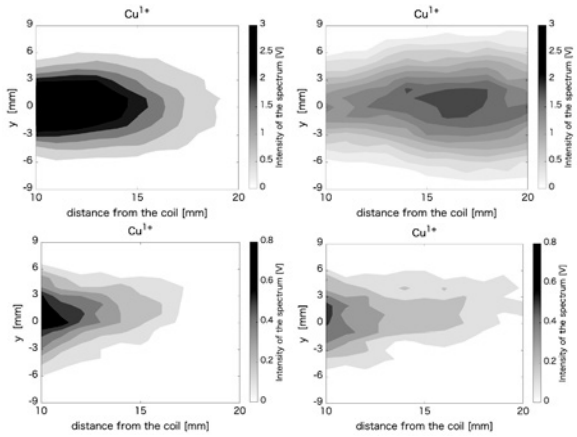

Fig. 5 Typical time evolution of emission intensity distribution of Cu^{+} ions without magnetic field (upper) and with a magnetic field of 90 mT (lower). Elapsed times are 328 ns (left) and 408 ns (right).

measurement of the ion flux using a Faraday cup. This trend may not have been seen in the previous measurement because all ion species were measured at the same time with the Faraday cup. From this result, the application of magnetic nozzles may not always be good for improving ion flux densities if axial expansion suppression and associated reduction in ion drift velocity actually occurs. The results for Cu^{+} ions are shown in Fig. 5. Although overall tendencies are similar to those for Cu^{2+}, the radial compression and the axial expansion suppression effects seems to be relatively moderate. This result is reasonable because it is natural that ions having higher charge are affected more strongly by the magnetic field. However, if the radial compression of the plasma occurs due to the $\boldsymbol{j}\times\mathbf{B}$ force, here $\boldsymbol{j}$ is the diamagnetic current flowing on the plasma surface, the compression effect should not be so sensitive to the charge state of the ions. To discuss the charge-state dependency of the plasma compression effect more precisely, we need to reduce the systematic errors in the laser plasma production and improve the spatial resolution of the two-dimensional scanning in the

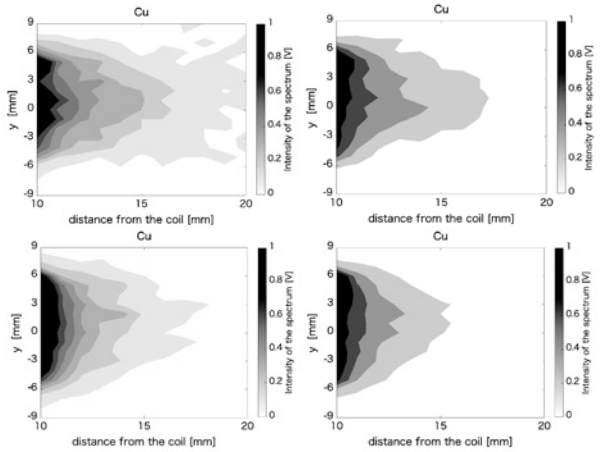

Fig. 6 Typical time evolution of emission intensity distribution of Cu atoms without magnetic field (top) and with a magnetic field of 90 mT (bottom). Elapsed times are 328 ns (left) and 408 ns (right).

spectral intensity measurement.

Finally, Fig. 6 shows the results for the copper atoms. The measurement conditions are the same as for ions. The effect of the magnetic nozzle is much smaller than that of ions, but the expansion of the plasma appears to be slightly suppressed. Since the neutral atoms do not interact directly with the magnetic field, they were considered to be indirectly affected by the magnetic nozzle. One possible explanation for this result is that the strong compression of ions by the magnetic nozzle increased the plasma pressure significantly, and as a result the behavior of the neutral atoms also changed due to hydrodynamic effects. However, the frequency of collisions between particles in the laser-produced plasma was considered to be quite low by the time they passed through the magnetic nozzle, and the classical fluid effect, *i.e.* the momentum exchange between particles is considered less pronounced. Another explanation is that increased plasma density may have facilitated collisional deexcitation of excited atoms, resulting in a reduced amount of light emission. In fact, the same is true for the ions. In other words, the particle density distributions reconstructed in this study are nothing more than the density distributions of excited ions and atoms, and they do not necessarily reflect the behavior of the entire particles including the ground state particles. For more accurate analysis, it should be combined with the analysis of atomic processes using the CR model.

4. Conclusions

In this study, we have developed a spectroscopic imaging system for investigating the behavior of specific ions and atoms in plasma. The preliminary experiments clarified that the radial compression of the copper ion distribution in the laser-produced plasma that passed through the magnetic nozzle depends weakly on the ion charge state. In addition, it is found that the behavior of neutral atoms was also slightly affected by the magnetic nozzle. However, we need to note that only excited ion and atoms are observed in these results, and the atomic processes in the plasma should be considered more carefully to analyze the behavior of the entire plasma particles including ground state ions and atoms. In any case, there is no doubt that this method will be a very powerful tool for optimizing the control of laser-produced plasma by magnetic nozzles.

References

[1] J. Hasegawa, H. Wakabayashi, H. Fujii, M. Tsukamoto, K. Horioka, “Control of a Laser-Produced Dense Plasma Flow by a Divergent Magnetic Field”, AIP Conf. Proc. 2011,030010-1-030010-3; https://doi.org/10.1063/1.5053271 (2018).

E. Fundamental Research Division

E.1 Study for nuclear fission and its application

Chikako Ishizuka and Chiba Satoshi

1. Introduction

Nuclear fission has been studied for eighty years since its discovery. However, we still cannot explain the whole property of nuclear fission even of ^{236}U with sufficient predictive power, although experimental data and/or empirical models have been applied for practical use. Such practical methods may work properly in the case of well examined n-induce fission of ^{235}U and ^{239}Pu. On the other hand, in order to develop a new system such as Accelerator-driven Systems (ADS) and Fast Reactors (FR) which may act as a transmuter of the TRU wastes, we need high quality nuclear data on minor actinides (MA). Experiments to obtain fission data for MA and long-lived fission products (LLFP) have been performed in various facilities. But it is still difficult to cover whole fission data, such as fission fragment mass distributions (FFMDs), total kinetic energy; TKE, number of prompt and delayed neutrons, and decay heat from the fission products. Chiba laboratory has developed nuclear models which can reproduce and predict these physical quantities on nuclear fission.

In addition to the above fundamental approaches, we are also working on the reduction of long-lived nuclear wastes by studying the whole mechanism of nuclear fission process from scission to β-decay, and by developing high-quality nuclear data. In our laboratory, we have also investigated the influence of nuclear data on the clearance problem of decommissioning. In Fig.1, we show the schematic view of nuclear fission process. The aim of Chiba laboratory is the improvement of fission nuclear data such as fission product yields, prompt neutrons and decay heats, by eludidating the fundamental mechanism of nuclear fission.

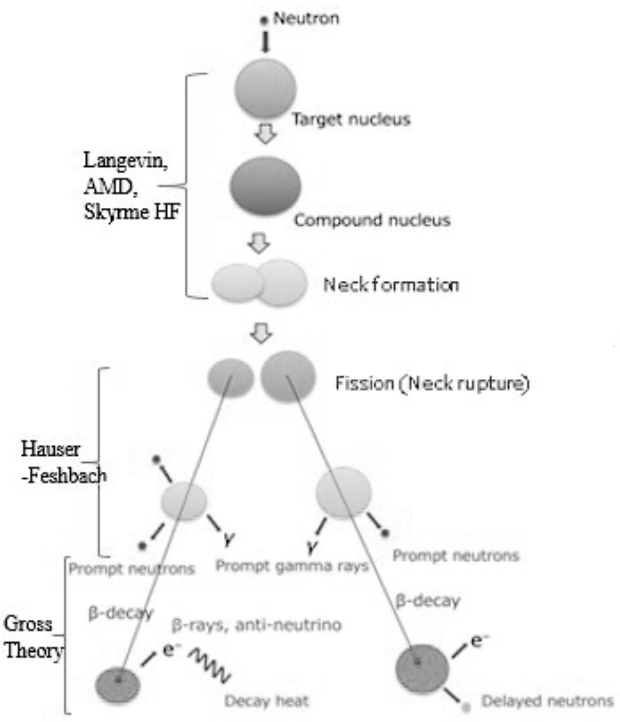

Fig.1 Schematic view of the whole process of nuclear fission and applicable theoretical models.

2. Fundamental studies for nuclear fission

Nuclear fission is a motion of a many-body quantum system. It is still very difficult to describe the whole feature of a nuclear fission process with a single model. Indeed, there is no theoretical model which can completely simulate the whole process of nuclear fission shown in Fig.1. Therefore, we have adopted different models depending on our purpose. In our laboratory, we have studied the fundamental mechanism of nuclear fission at low energies using various nuclear-physics theories such as multidimensional Langevin models, the Anti-symmetrized Molecular Dynamics model, and Time-dependent Hartree Fock model. Furthermore, we have used the statistical models to study prompt neutron emission from the fission fragments, and the gross theory of beta-decay and summation method to investigate the anti-neutrinos emitted from nuclear reactors. We also carried out experiments at tandem accelerator facility at JAEA Tokai to determine the fission barrier height.

2.1. Fission properties before prompt neutron emission

Langevin models can reproduce and predict not only the fission fragment mass yields but also the total kinetic energies of the fission fragments of various actinides very accurately. That is the strong point of this model. In the Langevin model, a nuclear fission process is regarded as a time-evolution of the nuclear shape of a compound nucleus, which is formed via neutron absorption by a target in a neutron-induced reaction, following the equation of motion under the friction force and the random force (so called the Langevin equation). We have developed the Langevin model by extending degree of freedom to describe a realistic fission-nuclear-shape, and by introduction of the microscopic transport coefficients based on the linear response theory. Recently, we performed the systematic survey of the nuclear fission pattern from actinide to super heavy nuclei [1]. Then we found fission patterns of super heavy nuclei are completely different from those of actinide, because the different nuclear shells dominate the fission.

2.2. Determination of fission-barrier heights by multi-nucleon transfer reactions

Height of the fission barrier is the most important physics quantity to be comprehended accurately in order make any predictions on nuclear fission. Many theoretical models fail to predict the fission barrier height with a good accuracy. On the other hand, experiment is also difficult

to be performed for many of the minor actinides for which preparation of samples is not easy. We have proposed a new method to determine the fission barrier height by using multi-nucleon transfer reactions. This method allows us to reach many nuclei which otherwise cannot be reached. As our first evidence that such a method works, we have applied this method for ^{18}O on ^{237}Np case, and derived the fission barrier heights for a few actinide nuclei [2].

2.3. Microscopic approach to develop a suitable effective-interaction to describe nuclear fissions

Microscopic approach such as Skyrme Hartree-Fock model and time-dependent Hartree-Fock model has been used to describe nuclear reaction, because it can provide the detailed information on nuclear deformations at scission (just after fission-fragment formation), and on fission barrier height etc. Nevertheless, there is no effective interaction designed for nuclear fission itself. In our laboratory, we have investigated fission properties of a few representative interactions to develop a brand-new effective instruction for fission, based on the constrained Hartree-Fock + BCS pairing [2] assuming the axial symmetry, and also on Skyrme Hartree-Fock model with BCS pairing without any symmetry assumptions which are often used to reduce computing cost. As a result, we found Skyrme type interactions overestimate the fission barrier heights independent on parameter sets of effective interactions and the axial symmetry assumption. Hence, we have investigated which term in the Skyrme parameter is effective to control the barrier height.

3. Beta decay of fission products

After prompt neutrons and gammas emitted from the fission fragments, the beta-decays of these nuclei will occur. Neutrinos produced by the beta-decay process play a significant role in the surveillance and in-service inspection in nuclear power plants. In our laboratory, we have studied the anti-neutrino spectrum from aggregate fission products beta-decays based on the gross theory.

4. Evaluation of nuclear data

4.1: Development of fission yield data library for various applications

High precision nuclear data is necessary to evaluate the total heat from the fission products and their toxicity. Major nuclear data libraries such as JENDL-4.0 contain ambiguity due to the experimental data and their analysis. Fortunately, a number of measurements of fission products yields (FPYs) have been accumulated, since the last major evaluation was performed in ENDF library which has provided the most of FPY data to JENDL/FPY library.

In our laboratory, we have developed FPY library based on original evaluation method of experimental data. Our FPY library contains not only yields such as independent yields and cumulative yields, but also the covariance information on uncertainty in each data. Recently, such covariance data is necessitated significantly. To develop the new library, we first gathered and evaluated experimental data from EXFOR database, and then developed a semi-phenomenological FPY model based on the recent knowledge of the shell effects including the even-odd staggering. The semi-phenomenological model is necessary to estimate the FPYs where no measured data exist. Hauser-Fechbach model was also applied to estimate unknown isomar ratios, and to obtain the covariance.

Thus, we constructed a brand-new FPY library for the first time in Japan. Our FPY library will be adopted in the next version of JENDL library as a national nuclear database.

4.2: Estimation of uncertainty of nuclear data

The uncertainty in various quantities relating to nuclear reactors becomes necessary information. Especially, the uncertainty in the evaluation for radioactivity due to neutron irradiation is strongly required by nuclear regulation procedures.

We have evaluated the uncertainty of the cross sections of some LLFP nuclides in JENDL-4.0 by use of T6 code which evaluate the nuclear data employing the Bayesian Monte Carlo calculations. Using these results, we have investigated the uncertainty of the nuclear transmutation of LLFP nuclides, and the uncertainty of radioactivity for decommissioning.

Acknowledgment

This work was supported by the grant "Research and development of an innovative transmutation system of LLFP by fast reactors" entrusted to the Tokyo Institute of Technology, "Development of prompt-neutron measurement in fission by surrogate reaction method and evaluation of neutron- energy spectra" entrusted to JAEA, and "Concept of a nuclear fuel cycle using an environmental load-reducing light-water reactor" entrusted to Toshiba by the Ministry of Education, Culture, Sports, Science and Technology of Japan (MEXT). The authors also thank Grant-in-Aid for Scientific Research (C) 18K03642.

Reference

1. C. Ishizuka, X. Zhang, M. D. Usang, F. A. Ivanyuk, S. Chiba, “Effect of the doubly magic shell closures in ^{132}Sn and ^{208}Pb on the mass distributions of fission fragments of superheavy nuclei”, Phys. Rev. C **101**, 011601 (R) (2020) published 27 January, 2020.

2. K. R. Kean, T. Nishikawa, Y. Iwata, “Perturbation Scheme for the Effective Nuclear Force”, JPS Conf. Proc., 010018 (2020) , received July 18, 2019.

E.2 Radial Dependence of Rotational Temperature of N_2 and N_2^+ Molecules in Microwave Discharge Nitrogen Plasma

Hiroshi Akatsuka, Atsushi Nezu

1. Introduction

Spectroscopic measurement of the plasma in a discharge tube is to find the integrated value along the line of sight. In an axially symmetric system, intensity of observed spectrum of optical emission spectroscopy (OES) can be re-determined as a function of each radial position r by applying Abel inversion. In this study, the radial dependence of the rotational temperature of molecules will be discussed. The objective of this study is to find the radial dependence of the rotational temperature T_r of neutral N_2 molecule with 2PS band, and that of molecular ion N_2^+ with 1NS band in nitrogen plasma by Abel inversion, and to discuss the dependence and its difference if any.

2. Experiment

Experimental apparatus applied in this study is the same one as used in the authors' previous studies [1]. The microwave frequency is 2.45 GHz and the power applied to the plasma is 400 W. The discharge tube is made of quartz with an inner diameter of 26 mm. A nitrogen plasma is generated inside this discharge tube, and the gas pressure at discharge is set at 1.0 Torr [1].

3. Results and Discussion

It is found that the vibrational temperature T_v of N_2 C state ranges from 0.6 to 0.9 eV, while that of N_2^+ B state from 1.1 – 3 eV, which are considered to be rather common for microwave discharge 1-Torr N_2 plasma. Almost no remarkable radial dependence was found for them.

Meanwhile, a remarkable difference in the radial distribution is found in the rotational temperatures. Figure 1 shows radial distributions of the rotational temperature T_r of 2PS and that of 1NS. The rotational temperature of 2PS was found to be T_r = 0.04 – 0.06 eV, which was monotonically decreasing function of the radial position r.

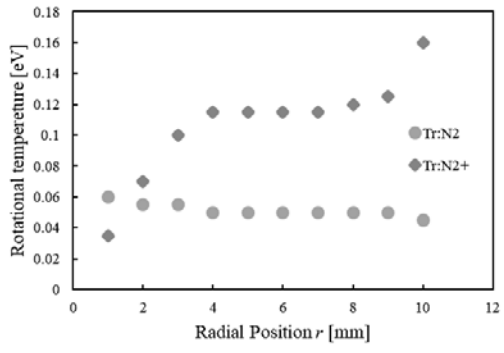

Fig. 1. Radial dependence of rotational temperatures $T_r(r)$ of 2PS (N2 in Fig.) and 1NS (N2+ in Fig.).

In many discharge experiments close to this condition, the rotation temperature of 2PS is widely applied to gas temperature measurement. Since the heat is removed from the wall by air cooling in this microwave discharge experiment, it is a reasonable result that the T_r of N_2 C state (or 2PS) becomes a monotonically decreasing function of the radial position r.

On the other hand, for the rotational temperature T_r of 1NS, which is the emission from the excited B $^2\Sigma_u^+$ state of the N_2 molecular ion, as shown in Fig. 1, it is found that it ranges from 0.04 to 0.13 eV. It is already found that the rotational temperature of molecular ions shows higher value than that of neutral molecules under the present discharge conditions, and consequently, the ranges of observed values are reasonable [4].

However, the most remarkable finding is the following. That is, the minimum value of rotational temperature of 1NS was found at the central portion of the discharge tube, and a completely opposite radial dependence was found as monotonous rising as going radially outward. The reason is considered as follows. The rotational temperature of 1NS, which is the emission from the excited state of the nitrogen molecular ion N_2^+, does not simply reflect the neutral gas temperature. It is considered that the rotational temperature of the molecular ion reflects the temperature information of the ion, although the absolute value may not be accurately represented.

It was numerically found that the ion temperature becomes higher at the outer peripheral part than the axially central position in the steady DC discharge plasma sealed in the discharge tube when the direct simulation Monte Carlo (DSMC) method is performed on the particle kinetics not only of neutrals but also ions, although such a simulation is conducted only for monatomic discharge species, i.e., rare gases. In these simulations, the radial dependence of neutral gas temperature observed as rotational temperature of N_2 2PS is also found to agree qualitatively well with Ichiki *et al.*'s simulation [5]. By measuring the rotational temperature of molecular ions, there is a possibility to obtain information on ion temperature, at least qualitatively.

Reference

1. Y. Yamashita, F. Yamazaki, A. Nezu and H. Akatsuka, Jpn. J. Appl. Phys. **58**, 016004 (2019).
2. J. Konami, A. Nezu, H. Akatsuka, Proc. DPS2019, 91 (2019).
3. J. Konami, A. Nezu, H. Akatsuka, Proc. Ann. Meeting 2018 JSPF, 6P15 (2018).
4. H. Akatsuka, H. Kawano, K. Naoi, H. Matsuura and A. Nezu, Jpn. J. Appl. Phys. **56**, 056102 (2017).
5. T. Ichiki, T. Sakamoto, H. Matsuura and H. Akatsuka, J. Plasma Fusion Res. SERIES **8**, 768 (2009).

E.3 Spectroscopic Study of CO Excited States in Microwave Discharge CO_2 Plasma

Hiroshi Akatsuka, Atsushi Nezu

1. Introduction

Carbon dioxide plasmas are widely applied in the decomposition of CO_2 into CO for energy storage, CO_2 laser technologies, etc. It should also be mentioned that CO molecules are sometimes added to the semiconductor processing plasmas for the improvement of the selection ratio in etching processes. However, the excitation kinetics of electronically excited states of the CO molecule are not fully understood yet. Particularly, the excitation processes of CO are not well investigated. In this study, spectroscopic characteristics of the Angstrom band ($B\ ^1\Sigma^+ \rightarrow A\ ^1\Pi$) and the third positive system (3PS) band ($b\ ^3\Sigma^+ \rightarrow a\ ^3\Pi$) of CO molecule in microwave discharge CO_2 plasma will be investigated.

2. Experiments

Experimental apparatus applied in this study is the same one as used in the authors' previous studies [1]. Microwave with its power 400 W is generated with a magnetron protected with an isolator, and guided to the discharge section through waveguides. As a discharge gaseous media, CO_2 gas is applied to the quartz discharge tube with an inner diameter 26 mm. CO_2 plasma is generated inside the quartz tube. After the spectrum with OES measurement is acquired, the rotational and vibrational temperatures, T_r and T_v, are determined. Further details are described in [1].

3. Results and Discussion

The CO 3rd PS can be identified between 280 and 360 nm, while the Angstrom band can be observed between 410 and 660 nm. In the present study, T_v and T_r of the CO Angstrom band of (v', v'') = (0, 1), (1, 2) are chosen such that the theoretical calculation fits the OES spectrum best, while (v', v'') = (0, 2), (1, 3) are adopted for CO 3PS band.

Concerning the 3PS band, general curve fitting method of diatomic molecular band spectrum [2] gave successful results of T_v and T_r as best fitting parameters. An example of spectral fitting is shown in Fig. 1.

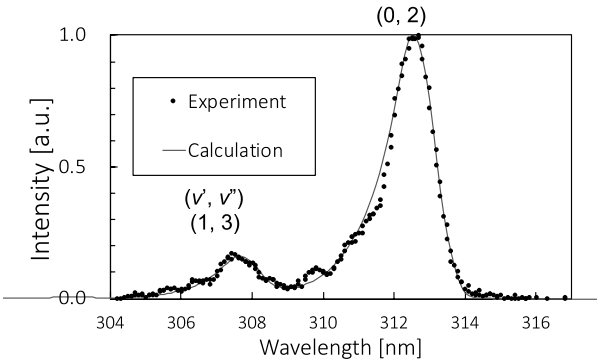

Fig. 1. Theoretical fitting of CO 3PS band spectrum with $\Delta v = -2$. $T_v = 0.24$ eV, $T_r = 0.15$ eV.

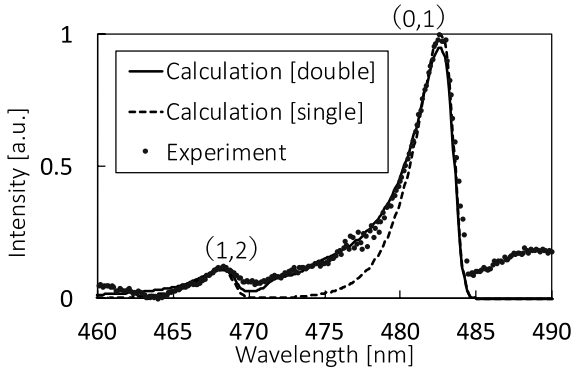

Fig. 2. Theoretical fitting of CO Angstrom band spectrum with $\Delta v = -1$. $T_v = 0.3$ eV. $T_r = 0.04$ eV for single-T_r fitting, while $T_r = 0.17$ and 0.04 eV for double- T_r fitting with their component-ratio 1:3.

In the meantime, although the same procedure was applied to the Angstrom band, the discrepancy of the spectral shape between experiments and calculations was not acceptable. Therefore, to improve the theoretical fitting to the experimental data, two-rotational temperature components are considered: a low and a high T_r components with weights of 3/4 and 1/4 respectively. As a result, calculated Angstrom band spectra are fitted to OES measurement. The result of the theoretical fitting is shown in Fig. 2. The double-T_r fitting can successfully work for other Δv bands of the CO Angstrom band [3].

Table 1 summarize the present results of T_v and T_r for 3PS and Angstrom bands. Together with the non-equilibrium characteristics between 3PS and Angstrom bands due to the difference in spin-multiplicity, the two rotational temperature distribution was newly found for the CO Angstrom band. The discussion on origin of this two- T_r distribution remains as future issues [4].

Table 1. Summary of vibrational and rotational temperatures of CO molecule obtained in the present CO_2 microwave discharge plasma.

	3PS	Angstrom bulk	Angstrom tail
T_v [eV]	~ 0.24	~ 0.30	
T_r [eV]	~ 0.15	0.03 – 0.05	0.13 – 0.17

Reference

1. Y. Yamashita, F. Yamazaki, A. Nezu and H. Akatsuka, Jpn. J. Appl. Phys. **58**, 016004 (2019).
2. Y. Morita, A. Nezu, H. Akatsuka, Proc. DPS2018, 108 (2018).
3. S. Yamada, A. Nezu, H. Akatsuka, Proc. XXXIV ICPIG & ICRP-10, PO18AM-029 (2019).
4. S. Yamada, A. Nezu, H. Akatsuka, Proc. 72-GEC, FT1.15 (2019).

E.4 Optical Emission Spectroscopic Measurement of Electron Temperature of Atmospheric-Pressure Non-Equilibrium Ar-CO_2 Plasma

Hiroshi Akatsuka, Atsushi Nezu

1. Introduction

Atmospheric-pressure nonequilibrium plasma has been widely applied However, there are few reports on their electron temperature. The authors measured its electron temperature T_e of the pure Ar atmospheric-pressure plasma by fitting the theoretical equation of the continuous spectrum. As a result, it was found that its electron temperature T_e = (0.8 – 0.9) eV, which almost coincided with the one obtained by Ar I line intensities and the Collisional Radiative (CR) model [1].

However, in practice, it seems normal to mix some reactive gases. Therefore, in this study, the same measurement as Ref. [1] will be conducted for CO_2-Ar plasma. LXcat database was used as the momentum transfer cross section of Ar and CO_2 required in this study.

2. Experiments

Figure 1 shows the schematic diagram of the discharge apparatus [2]. The 50-Hz AC discharge power was supplied by a transformer with its maximum voltage ~ 9 kVp-p.

The spectroscopic characteristics of the plasma can be observed through the optical window equipped with the discharge tube. Figure 2 shows the OES result observed experimentally as a time average over a discharge period. The electron temperature can be determined for the Maxwellian or Druyvesteynian EEDF as the best fitting parameter [2].

3. Results and Discussions

It was found that when CO_2 is mixed into atmospheric-pressure Ar discharge plasma, the emission gradually weakens as the mixing ratio increases. When the volume ratio of CO_2 was about 4.8%, the measurement was almost impossible due to its darkness. The volumetric fraction of CO_2 was varied in the range of (0 – 4)%.

Figure 2 also includes an example of theoretical fitting

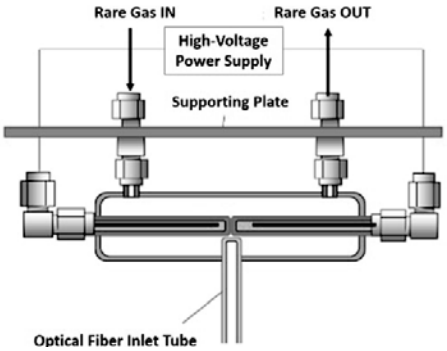

Fig. 1 Schematic diagram of the discharge tube. The electrodes are immersed in water in doubly sealed quartz tube. The outer tube is filled with the discharge rare gas.

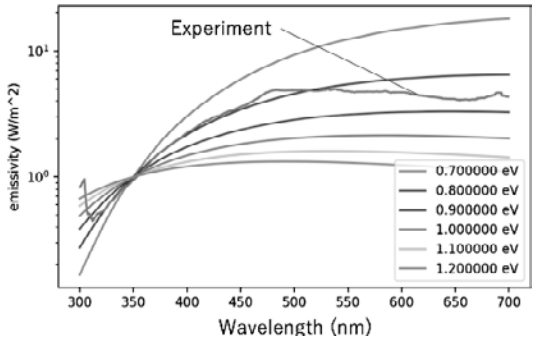

Fig. 2 Effective electron temperature plotted against CO_2 volumetric ratio. Flow rate of Ar is fixed at 4000 mL/min. EEDF is assumed to be Druyvesteynian.

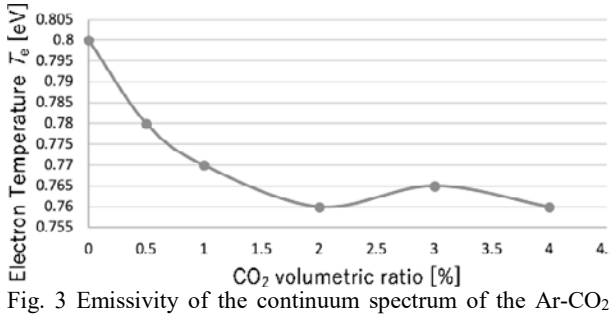

Fig. 3 Emissivity of the continuum spectrum of the Ar-CO_2 atmospheric-pressure non-equilibrium plasma and its theoretical fitting. Flow rate of Ar and CO_2 is set at 4000 and 20 [mL/min].

of continuum spectrum when the CO_2 volumetric ratio is 0.5%. Druyvesteyn EEDF is assumed and the fitting is performed with “effective electron temperature” equivalent to 2/3 times the average electron energy. The fitting is applied to the wavelength range from 300 – 45 nm. In the case of Fig. 1, the electron temperature can be obtained as T_e = 0.78 ± 0.01 eV by optimal fitting at 300 – 450 nm.

Next, Fig. 3 shows the relationship between the volumetric fraction of CO_2 and the electron temperature. As the volumetric ratio of CO_2 increases, a slight decrease in electron temperature is observed. This is considered a reasonable result, since electron energy is consumed in excitation processes such as vibration and rotation of CO_2 molecules [3, 4].

Reference

1. H. Akatsuka, H. Onishi, T. van der Gaag, and A. Nezu. Proc. SPP36/SPSM31, pp. 64-65, Jan. 2019.
2. H. Onishi, Y. Hakozaki, A. Nezu, and H. Akatsuka. Joint Technical Meeting on "Electrical Discharges" and "Plasma and Pulsed Power", IEE Japan, ED-18-047/PPP-18-029 (2018).
3. H. Lavigne, T. Shiroi, A. Nezu, K. Yambe, and H. Akatsuka: 36th JSPF Meeting, 202Ba06 (2019).
4. H. Lavigne, T. Shiroi, A. Nezu, K. Yambe, and H. Akatsuka ISPlasma2020/IC-PLANTS2020, 09pB01O (2020).

E.5 Horizontal Error Field Caused by Stray Toroidal Magnetic Flux through Iron Transformer in the PHiX Tokamak

Shunji Tsuji-Iio, Shin Naito, Hiroaki Tsutsui

1. Introduction

A small tokamak, PHiX, with an iron transformer suffers from horizontal error magnetic field. The main contributors to error fields in tokamaks are deviations of the toroidal field and poloidal field coils from their design positions [1]. As an example, correlation between systematic measurement error in radial field and toroidal field has been observed in the HT-2 tokamak [2]. Although we rearranged the set of toroidal field coils (TFCs) to make the major radii of their outer edges nearly the same and the central axis agrees with that of poloidal field coils (PFCs), the reduction in the strength of the error field was small.

By examining the time evolution of the error field, we found that it was generated with the excitation of the TFCs and the strength and distribution of error field change with the initial magnetization of the iron core. Some fraction of toroidal magnetic flux is considered to be attracted into the central iron core and to pass through the yokes. The leak of magnetic flux from side yokes which return to the iron core was identified to be the horizontal error field.

2. Experimental observation

2.1. PFC currents

An example of the time traces of PFC currents of a feedback controlled tokamak discharge is shown in Fig. 1. Four PFCs (PF1, PF2, PF5, PF6) at the outer side of torus shown in Fig. 2 generate vertical magnetic field and vary its curvature to shape the plasma cross section. The negative polarity of the currents means the counter direction to that of the plasma current so that it produces required vertical magnetic field for the MHD equilibrium. A set of bias currents like Fig. 1 is required for the plasma breakdown and it occurred around 0.237 s in this case. Note that the polarity of I_{PF6} current is opposite to the others and that its absolute value is nearly the same with those of the others. The PF1 and PF6 coil pair currents produces horizontal field comparable to the vertical field.

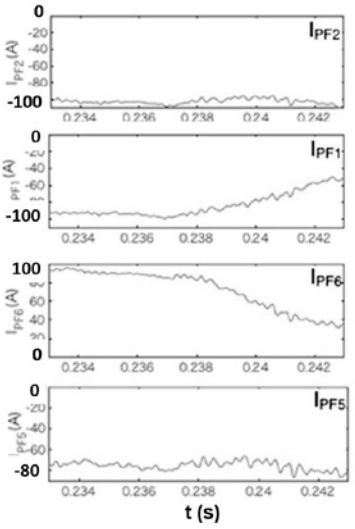

Fig. 1 A set of four current waveforms of PF1, PF2, PF5 and PF6 shown in Fig. 2

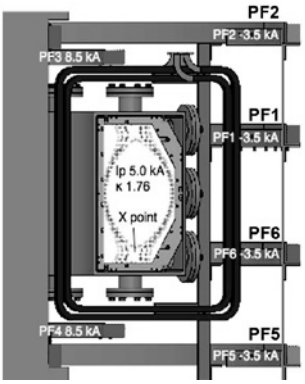

Fig. 2 The cross section of the PHiX tokamak with four PFCs devoted to generate vertical and horizontal magnetic fields. The ocherous cross section on the left-hand side indicates an iron core.

2.2. Poloidal magnetic fluxes

We examined the distribution of poloidal magnetic fluxes with 14 flux loops equipped in the vacuum vessel of PHiX. Its distribution after TFC excitation in the initial phase of the experiments are plotted in Fig. 3. When we subtract the fluxes between adjacent loops, we can see the average normal component of the magnetic flux between

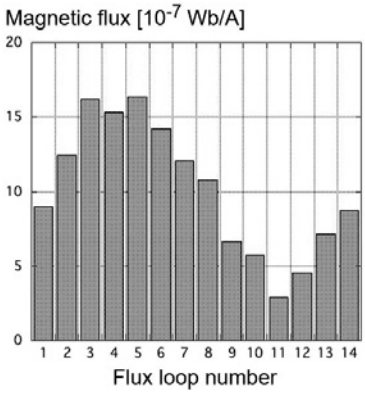

Fig. 3 Poloidal magnetic fluxes measured with 14 flux loops shown in Fig. 4

them as plotted in Fig. 4, which shows almost uniform horizontal magnetic field in the aperture of a D-shaped limiter.

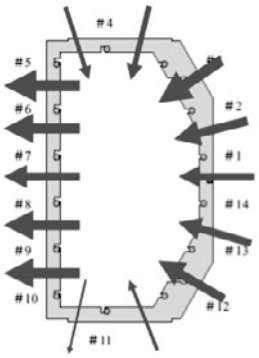

Fig. 4 The directions and widths of arrows illustrate the normal components of magnetic fluxes pass through adjacent poloidal magnetic flux loops shown by green circles which are hooked through notches of limiters.

Employing laser optics, we measured the outer major radii of the top and bottom semicircular rings on which TFCs were bolted and found that they differ by up 3.8 mm. And the center of the upper ones was displaced from that of the vacuum vessel by 4.0 mm. Consequently, we re-positioned the top and bottom rings to make them installed nearly on the same circumference of a circle within 0.5 mm. The concentricity between them and the outer PFCs were also secured within 0.5 mm.

Then we measured the distribution of poloidal magnetic fluxes with 14 flux loops after TFC excitation. The result shown in Fig. 5 means that the absolute values were reduced only by about one third. Although the polarity of the poloidal magnetic fluxes remeasured on the other day was reversed as shown in Fig. 6, the fluxes of loops at the inner side of torus from No. 5 to No. 10 drop monotonically in both cases, which imply that downward magnetic fluxes are added along the iron core.

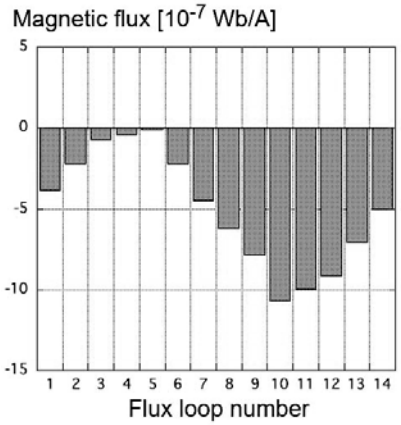

Fig. 5 Poloidal magnetic fluxes measured with 14 flux loops after rearrangement of TFCs

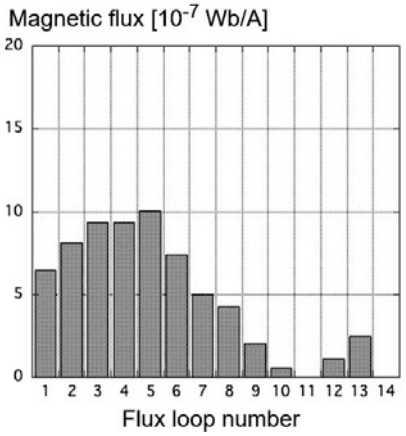

Fig. 6 Poloidal magnetic fluxes measured on another day after rearrangement of TFCs

2.3. Variation of magnetic flux inside iron transformer

We wound one-turn loops at upper and lower parts of the iron core and around the yokes to check the distribution of the changes in magnetization by excitation of TFCs. An example of results is shown in Fig. 7, where relative values of magnetic flux changes are plotted at the loop locations. Positive values indicate upward increase in the iron core and anti-clockwise one in the yokes. We confirmed that the magnetization in the transformer changes by excitation of TFCs. The opposite directions at the both ends of the iron core mean that magnetic fluxes were absorbed between them and the drops in magnetizations between adjacent loops imply a leak of magnetic flux as shown by the arrows in the apertures of the transformer. The overall directions of arrows explain the inward horizontal error field.

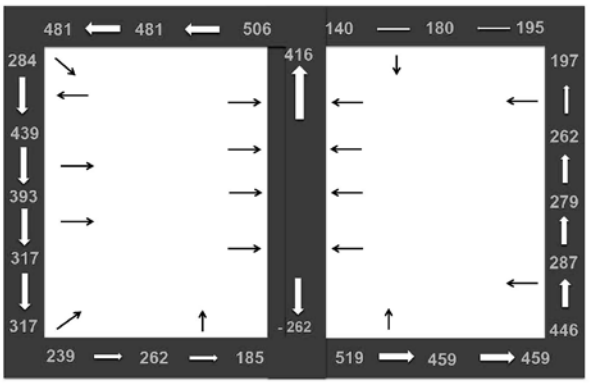

Fig. 7 Magnetic flux changes in the transformer by TFC excitation. The width of white arrows roughly indicates their relative magnitudes.

Acknowledgment

This work was supported by JSPS KAKENHI Grant Numbers 24360379 and 17K06990.

References

1. V. Amoskov *et al.*: Plasma Devices and Operations, Vol.13, No.2, pp. 87-103 (2005).
2. M. Abe, K. Takeuchi: Kakuyugo Kenkyu Vol.67, No.3, pp. 257-268 (1992).

III. Co-operative Researches

III. Co-operative Researches

III.1 Co-operative Researches within Tokyo Institute of Technology

(1) Development of concrete reinforced by metal fiber with low melting point, Nobuhiro Chijiwa, Minho O
(2) Collaborator, Study on Degradation of Fuel Debris by Radiation, Chemical, and Biological Damage, Advanced Research and Education Program for Nuclear Decommissioning, Ministry of Education, Culture, Sports, science and Technology (MEXT).
(3) Application of atmospheric plasma in medicine, Akitoshi Okino (FIRST)
(4) Biological effects of low dose/low dose rate radiation Research through integration of simulation and cell biology, Yuya Hattori (School of Engineering).
(5) Possible measurements of nuclear data using laser based neutron sources, Chikako Ishizuka, Satoshi Chiba
(6) Study on prompt-neutron emission mechanism of nuclear fission based on a statistical model, Chikako Ishizuka, Shin Okumura, Satoshi Chiba
(7) Development of quantitative evaluation method for charge polarization using Langevin model, Chikako Ishizuka, Satoshi Chiba
(8) Measurement of Underwater Arc Plasma by Optical Emission Spectroscopy and its Heat Transfer to Liquid Phase Injected into Water, Professor Shinsuke Mori, School of Materials and Chemical Technology — Department of Chemical Science and Engineering.
(9) Improve Understanding of Basic Engineering Lectures with e-learning, Professor Akira Chiba, Professor Koichi Yasuoka, Professor Shigeki Nakagawa, Professor Atsuhiro Nishikata, Professor Makoto Hagiwara, Professor Masahiro Watanabe, Professor Nozomi Takeuchi, Professor Shungo Zen, Doctor Ei Tokioka, School of Engineering — Department of Electrical and Electronic Engineering.

III.2 Co-operative Researches with Outside of Tokyo Institute of Technology

(1) Improvement to critical safety technology for Fukushima-Daiichi NPS decommissioning Research title, The name of collaborator, Toru Obara, Jun Nishiyama, Tokyo Institute of Technology, Hiroki Takezawa, Tokyo City University, Georgy V. Tikhomirov, Anton Smirnov, Ivan Saldikov, Ekaterina Bogdanova, Vladislav Romanenko, National Research Nuclear University (MEPhI).
(2) Conceptual study for Stationary Wave Reactor, Toru Obara, Jun Nishiyama, Tokyo Institute of Technology, Van Khanh Hoang, Vietnam Atomic Energy Institute.
(3) Study on burnup performance of Stationary Wave Reactor, Toru Obara, Jun Nishiyama, Tokyo Institute of Technology, Odmaa Sambuu, National University of Mongolia.
(4) Solid oxide electrolysis cell development for CO_2 reduction, JSPS Grant-in-Aid for Scientific Research (B), 2019-2022.
(5) High Temperature Thermal Energy Storage System, Agency of Natural Resources and Energy, METI, 2019-2023.
(6) Solid oxide electrolysis cell for Carbon recycling, New Energy and Industrial Technology Development Organization, 2020-2022.
(7) Chemical compatibility of thermal bonding fluids with reduced activation ferritic martensitic steel, National Institutes for Quantum and Radiological Science and Technology.
(8) Chemical compatibility of cement materials with liquid metals, National Institute for Fusion Science.
(9) Chemical compatibility of dissimilar material joint with liquid breeders, National Institute for Fusion Science.
(10) FRONTIER project TASK3 “Reaction dynamics between solid material-liquid metal interfaces for liquid divertor systems”, Oak Ridge National Laboratory, USA.
(11) Development of Subcritical Water Washing System for Cleanup and Reuse of Contaminated Soil, and Volume-reduction of Radioactive Waste, The Environment Research and Technology Development Fund, 1-1805.
(12) Study on Cs desorption from soil cay minerals by subcritical water containing metal ions, Grant-in-aid for Scientific research B, 18H03398.
(13) Study on radioactive Cs removal from soil containing organic compounds by subcritical water treatment, J&T Kankyo Co.
(14) Volume reduction and stable solidification of recovered Cs from classified contaminated soil, JESCO
(15) Separation of f-elements based on control of coordination space by ligand-immobilized stimuli-responsive hydrogels, Grant-in-Aid for challanging research (Exploratory), 18K19043
(16) Absorption study on specific trivalent lanthanide and valence-different uranium ions by ligand-immobilized soft materials-3, Inter-University Cooperative Research Program of the Institute for Materials Research, Tohoku University, 19K0002.
(17) Development of granulation method of MST, Hitachi-GE Nuclear Energy Ltd.
(18) Development of cyano-group bridge-type coordination polymer with a high sorption characteristic of Platinum-group elements for high quality and volume reduction of vitrified objects containing high-level radioactive nuclear wastes, H29 commissioned research from Nagoya University, Japan Science and Technology Agency (JST).
(19) Development of apatite ceramics for stabilization of ALPS precipitation wastes, Advanced Research and Education Program for Nuclear Decommissioning, Ministry of Education, Culture, Sports, science and

Technology (MEXT)

(20) Cross-disciplinary nuclear system research for load reduction of radioactive waste management, commissioned research from Radioactive Waste Management Funding and Research Center, Japan Science and Technology Agency (JST)

(21) Study on reprocessing and waste by diverse condition of nuclear fuel cycle, Subcontract from Radioactive Waste Management Funding and Research Center, Agency for Natural Resources and Energy

(22) Study on MA recovery flowsheet by extraction chromatography and in-line analysis, Subcontract from Japan Atomic Energy Agency, Agency for Natural Resources and Energy

(23) Study on extraction separation process of minor actinide suitable for its solidification and stabilization, and index development for evaluation of the impact of MA separation on final disposal. Mitsubishi Heavy Industry

(24) Development of recovery process of minor actinide flowsheet based on cold experiments , and its effect on final disposal (Phase 1), Mitsubishi Heavy Industry

(25) Study on trace metal separation and quantification, AGC

(26) Study on complexes formed in the adsorbent of the extraction chromatography column, Japan Atomic Energy Agency

(27) Study on separation of Platinum Group Elements by valence control, Challenge bounty for new research, Organiation of Fundamental Research, Tokyo Institute of Technology

(28) MEXT, "Development of Tailor-made Uranium Adsorbent from Seawater on the Basis of Uranyl Coordination Chemistry", Oct 2019-Mar 2022, 1,500,000 JPY.

(29) JSPS Grant-in-Aid (C), "Development of Nano-pore Sequencer for Uranyl Ion Detection", Apr 2019-Mar 2022, 4,420,000 JPY.

(30) Study on Low-Cost Process of SiC/SiC Composites: Japan Aerospace Exploration Agency (JAXA)

(31) Study on Properties of B_4C Neutron-Absorbing Materials for Control Rods: Japan Atomic Energy Agency (JAEA)

(32) Study on Neutron-Irradiation Resistance of Orientation-Controlled Ceramics: National Institute for Materials Science (NIMS)

(33) Sinterability of SiC Ceramics with Al_4SiC_4 Addition and Their Properties: National Institute for Materials Science (NIMS)

(34) Research on Formation and Characterization of Oxide Nanopowder : Vinca Institute, University of Belgrade, Serbia

(35) Fundamental Study on Plasma Resistance of Rare-Earth Fluoride Ceramics: Nippon Yttrium Co., Ltd.

(36) Study on Applicability of Alumina-Based Fibers for Ceramics-Based Composites, Denka Co. Ltd., Nitivy Co. Ltd.

(37) Creation of SiC Fiber-Reinforced Composites with Titanium Silicides Matrix, Grant-in Aid for Scientific Research (B), Japan Society for the Promotion of Science

(38) Development of Novel Environment-Resistant Interphase for Ceramic-Based Composites using Nanolayered-Ternary Carbides, Grant-in-Aid for Challenging Research (Exploratory), Japan Society for the Promotion of Science

(39) Development of Highly Microstructure-Controlled Ceramic Neutron Absorbers for Improving Safety of Fast Reactors, Innovative Nuclear Research and Development Program, MEXT.

(40) Fabrication of Simulated Solid Rocket Motor Slag: Japan Aerospace Exploration Agency (JAXA)

(41) Research on Adsorbents of Siloxane Compounds for Application under Extreme Environment: Japan Aerospace Exploration Agency (JAXA)

(42) Astrobiology Experiments Based on MeV Ion Beams, Division of Materials Science and Chemical Engineering, Faculty of Engineering, Yokohama National University.

(43) Development of Negative Ion Sources for Tandem Accelerators, Atomic Energy Research Laboratory, Tokyo City University.

(44) Detection and Quantification of Actinides by X-ray Fluorescence Analysis for Radiation Emergency Medicine, National Institutes for Quantum and Radiological Science and Technology.

(45) Synthesis of Anticancer Drugs inside Cancer Cells from Non-Toxic Precursors by Monochromatic X-ray Irradiation, Grant-in-Aid for Challenging Exploratory Research, Japan Society for the Promotion of Science.

(46) Development of Low-Dose X-ray Fluorescence Analysis for Cultural Heritage Samples by Proton-Induced Monochromatic X-rays Considering Late Effects after 100-1000 years, Grant-in-Aid for Scientific Research (B), Japan Society for the Promotion of Science.

(47) Structural biology on the effect of hyperthermia on DNA double-strand break recognition protein Ku, Grant-in-Aid for Challenging Research from JSPS.

(48) Exploratory research for new cancer therapy through integration of nanomedicine and radiation, Rujiwa Wanotayan (Mahidol University, Thailand), supported by Follow-up Research Fellowship for Former International students.

(49) Analysis of DNA damage response of skin cells and application of atmospheric plasma in cosmetics, TAKARA Belmont, Co. Ltd.

(50) Study on the biological effects of low dose/low dose rate radiation Research through integration of simulation and cell biology, Ritsuko Watanabe (QST).

(51) Building basic theories and research networks for the systematic and quantitative understanding of radiation effects, Yuichiro Manabe (Osaka

University), Masako Bando (Kyoto University).

(52) Study on the relationship between DNA damage repair capacity and cancer radiotherapy outcomes, Koichi Sakata, Masanori Someya (Sapporo Medical University).

(53) Possible measurements of nuclear data using laser based neutron sources, with Takehito Hayakawa (QST)

(54) Study on prompt-neutron emission mechanism of nuclear fission based on a statistical model, with Toshihiko Kawano (LANL, USA)

(55) Development of quantitative evaluation method for charge polarization using Langevin model, with Katsuhisa Nishio (JAEA)

(56) “Research and development of an innovative transmutation system of LLFP by fast reactors” entrusted to the Tokyo Institute of Technology by the Ministry of Education, Culture, Sports, Science and Technology of Japan (MEXT), with Toshio Wakabayashi(Tohoku Univ.), Yoshiaki Tachi (JAEA), Naoyuki Takaki (Tokyo City Univ.)

(57) "Development of prompt-neutron measurement in fission by surrogate reaction method and evaluation Development of a passive reactor shutdown device to prevent core damage accidents in fast reactors, MEXT Innovative Nuclear Research and Development Program in Japan, Kyushu University, University of Fukui, Tokyo City University, Japan Atomic Energy Agency.MEXT, with Katsuhisa Nishio (JAEA).

(58) "Concept of a nuclear fuel cycle using an environmental load-reducing light-water reactor" entrusted to Toshiba by MEXT, with Koji Hiraiwa (Toshiba corporation), Takanori Kitada and Satoshi Kitada (Osaka Univ.)

(59) "The study on nuclei and neutron matter using finite-range three-body force" Naoyuki Itagaki (Kyoto Univ.)

(60) "The study on the influence of nuclear fission on the rapid neutron capture process" Shinya Wanajo (AEI, Max Plank Institute), Yuichiro Sekiguchi (Toho Univ.)

(61) Diagnostics of Electron Energy Distribution Function of Atmospheric-Pressure Plasmas with Phase-Resolved Optical Emission Spectroscopy Measurement of Continuum Spectrum, JSPS Grant-in-Aid Scientific Research (B), 19H01867, 2019-2022.

(62) Measurement of Temperature of Spark-Discharge Plasma in Engine Cylinder by Optical Emission Spectroscopy for Innovative Automobile Engine Research, TOYOTA Central R&D Labs.

(63) Diagnostics of Low-Pressure Discharge Argon Plasma by Multi-Optical Emission Line Analysis Based on the Collisional-Radiative Model, Tokyo Metropolitan Industrial Technology Research Institute.

(64) Evaluation of Electron Density and Temperature using CR model in Interaction between Metal Object and Atmospheric Non-Thermal Argon Plasma, Niigata University.

(65) Determination of Electron Density and its Temperature using Collisional Radiative (CR) Model in High-density Helicon Plasma for Electric Propulsion of Artificial Satellites, Tokyo University of Agriculture and Technology, Chubu University

(66) Optical Emission Spectroscopic Measurement of Electron Temperature with Continuum Emission of Atmospheric-Pressure Non-Equilibrium Ar-CO_2 Mixed Plasma, Télécom Physique, Université de Strasbourg.

(67) An Evaluation of a Vacuum Arc Instability Phenomenon with the Silver-Palladium Compound Material on the Cathode Spot, King Mongkut’s University of Technology Thonburi, Thailand, University of Miyazaki, Kagawa University.

(68) Thermodynamic characterization of fuel debris and fission products in Fukushima Daiichi Nuclear Power Plant, OECD/NEA

(69) Elucidation of reaction mechanism and behavior between molten corium and inside wall of RPV in FDNPP, Sandia National Laboratory, U.S.A.

(70) Nuclear data and its preparedness for developing non-destructive assay technique for non-proliferation and nuclear security, Kakenhi, grant no. 17K07005

(71) Development of a passive reactor shutdown device to prevent core damage accidents in fast reactors, MEXT Innovative Nuclear Research and Development Program in Japan, Kyushu University, University of Fukui, Tokyo City University, Japan Atomic Energy Agency.

(72) Study on Advanced Nuclear Energy System Based on the Environmental Impact of Radioactive Waste Disposal, MEXT Innovative Nuclear Research and Development Program in Japan, grant no. JPMXD02 19209423, Radioactive Waste Management Funding and Resource Center, Hokkaido University, Japan Atomic Energy Agency.

(73) Nonproliferation features of molten salt fast reactor, Texas A&M University.

(74) Easy and Advanced Non-destructive assay technique to quantify nuclear material in various type of nuclear waste forms, Japan Atomic Energy Agency.

IV. List of Publications

IV. List of Publications

Journals

(1) Takeshi Muramoto, Jun Nishiyama, Toru Obara: Numerical analysis of criticality of fuel debris falling in water", *Annals of Nuclear Energy*; Vol. **131**, pp. 112-122 (2019).

(2) Hiroki Osato, Jun Nishiyama, Toru Obara: Application of Melt-refining Process to Transition State of CANDLE Burning Fast Reactor", *Annals of Nuclear Energy*, Vol. **128**, pp. 77-83 (2019).

(3) Kazuki Kuwagaki, Jun Nishiyama, and Toru Obara: Concept of breed and burn reactor with spiral fuel shuffling; *Annals of Nuclear Energy*, Vol **127**, pp. 130-138 (2019)

(4) Delgersaikhan Tuya, Toru Obara: Development of Monte Carlo Neutron Transport Method-Based Supercritical Transient Code with Time-Dependent Feedback Capability; *Nuclear Science and Engineering*, Vol. **193**, pp. 481-494 (2019).

(5) Shigehiko Funayama, Hiroki Takasu, Seon Tae Kim, Yukitaka Kato: Thermochemical storage performance of a packed bed of calcium hydroxide composite with a silicon-based ceramic honeycomb; *Energy*, 201 (2020) 117673.

(6) Seon Tae Kim, Haruka Miura, Hiroki Takasu, Yukitaka Kato, Alexandr Shkatulov, Yuri Aristov: "Adapting the MgO-CO_2 working pair for thermochemical energy storage by doping with salts: effect of the $(LiK)NO_3$ content"; *Energies*, 12(12), 2262 (2019).

(7) Seon Tae Kim, Takuya Nihei, Chisato Kurahashi, Hitoshi Hoshino, Hiroki Takasu, Yukitaka Kato: "Kinetic study of lithium orthosilicate pellets for high-temperature chemical heat pumps"; Energy Storage, Energy Storage. 2019;1:e72. (2019).

(8) Naoto Uchiyama, Hiroki Takasu, Yukitaka Kato: "Study of cyclic durability of calcium carbonate materials for calcium oxide/water thermo-chemical energy storage"; *Applied Thermal Engineering*, 160(2019)113893.

(9) S. Funayama, H. Takasu, M. Zamengo, J. Kariya, Y. Kato; "Composite Material for High-Temperature Thermochemical Energy Storage using Calcium Hydroxide and Ceramic Foam"; *Energy Storage*, pp. 1-12, 2019;1:e53.

(10) S. Funayama, H. Takasu, M. Zamengo, J. Kariya, S. T. Kim, Y. Kato: "Performance of thermochemical energy storage of a packed bed of calcium hydroxide pellets"; *Energy Storage,* pp. 1-11.

(11) Y. Numata, K. Nakajima, H. Takasu, Y. Kato: "Carbon Dioxide Reduction on a Metal-Supported Solid Oxide Electrolysis Cell for iACRES"; *ISIJ Int'l*, 59(4), pp. 628-633 (2019).

(12) Seon Tae Kim, Chisato Kurahashi, Hitoshi Hoshino, Chiharu Takahashi, Yoshiro Tamura, Hiroki Takasu, Shusuke Saito, Masaki Kurihara, Yukitaka Kato: "Thermal Driving Demonstration of Li_4SiO_4/CO_2/Zeolite Thermochemical Energy Storage System for Efficient High-Temperature Heat Utilizations"; *ISIJ Int'l*, 59(4) pp. 721-726 (2019).

(13) H. Takasu, Y. Kato: "Study of sodium ferrite/carbon dioxide reactivity for high temperature thermochemical energy storage"; *ISIJ Int'l*, 59(4) pp. 715-220 (2019).

(14) Alexandr Shkatulov, Seon Tae Kim, Haruka Miura; Yukitaka Kato; Yuri Aristov: Adapting the MgO-CO_2 working pair for thermochemical energy storage by doping with salts, Energy Conversion and Management; 185, pp. 473-481 (2019).

(15) Alexandr Shkatulov, Hiroki Takasu, Yukitaka Kato, Yuri Aristov: "Thermochemical Energy Storage by $LiNO_3$-Doped $Mg(OH)_2$: Rehydration Study"; Journal of Energy Storage, 22, pp. 302-310 (2019).

(16) Hiroki Takasu, Hitoshi Hoshino, Yoshiro Tamura, Yukitaka Kato: "Performance evaluation of thermochemical energy storage system based on lithium orthosilicate and zeolite"; Applied Energy, 240, pp. 1-5 (2019).

(17) Joaquim Romaní, Jaume Gasia, Aran Solé, Hiroki Takasu, Yukitaka Kato, Luisa F. Cabeza: Evaluation of energy density as performance indicator for thermal energy storage at material and system levels; *Applied Energy*, 235, 954-962 (2019).

(18) Takehiro Sumita, Yoshinao Kobayashi. Dissolution behavior of solid stainless steel by its molten eutectic mixture with B4C under dynamic condition, Progress in Nuclear Energy, Vol. **117**, Nov. 2019.

(19) Ayumi. Itoh, Yoshinao. Kobayashi, A. Suzuki, T. Sato, Y. Nagae. Thermodynamic approach for determination of fuel relocation condition in severe accident progression, Journal of Nuclear Materials,Nov. 2019.

(20) Takehiro Sumita, Yoshinao Kobayashi. Investigation of corrosion-erosion behavior of stainless steel considering SS-B4C melt, Journal of Nuclear Materials, Vol. **515**, pp. 71-79, Mar. 2019.

(21) Ayumi Itoh, Takehiro Sumita, Masanori Kajihara, yoshinao kobayashi. The release behavior of boron and silicon from degraded absorber rods on core degradation during BWR severe accident, Journal of nuclear materials, Vol. **514**,101-108, Feb. 2019.

(22) Takehiro Sumita, Yoshinao Kobayashi. Quantitative Analysis Method for Determination of Boron Concentration in Stainless Steel-B4C Alloy by ICP-OES, Journal of the Japanese Society for Experimental Mechanics, Vol. **18**, No. 4, pp. 247-249, Jan. 2019.

(23) Masatoshi Kondo: Forefront of liquid metal technologies for fusion reactors; IOP Conf. Ser.: Earth Environ. Sci. **Vol.364**, 012012 (2019).

(24) Masatoshi Kondo, Masaru Tada, Youko Ohtsuka, Yoshimitsu Hishinuma, Takeo Muroga: Corrosion resistance of Al-rich steel and Al2O3 ceramic bulk in liquid Sn; *Fusion Engineering and Design,* **Vol.146**, pp. 2450-2456 (2019).

(25) Masatoshi Kondo, Teruya Tanaka, Satoshi Fukada,

Tsusar Valentyn: Liquid Breeder Materials; Comprehensive nuclear materials, *Reference Module in Materials Science and Materials Engineering 2020*, **Vol. 6**, pp. 176-202, (2020).

(26) T. Kobayashi, K. Akutsu, M. Nakase, S. Suzuki, H. Shiwaku, T. Yaita: Complexation Properties and Structural Character of Lanthanides Complexes of O, N-Hetero Donor Ligand BIZA ; *Separation Science and Technology*, **Vol. 54, No. 13**, pp. 2077–2083(2019).

(27) M. Cibula, Y. Inaba, Y. Li, T. Suzuki, H. Narita, K. Takeshita: Effect of HNO_3 Concentration on the Pd(II) Extraction Properties using a Thiodiglycolamide Compound; *Solvent Extraction Research and Development, Japan*,**Vol. 26, No 2**,pp.43-49 (2019).

(28) N. Tsutsui, Y. Ban, H. Suzuki, M. Nakase, S. Ito, Y. Inaba, T. Matsumura, K. Takeshita: Effects of Diluents on the Separation of Minor Actinides from Lanthanides with Tetradodecyl-1,10-Phenanthroline-2,9-Diamide (TDdPTDA) from Nitric Acid Medium; *Analytical Sciences*, **Vol.36, No.2**, pp.241-246(2019).

(29) X. Yin, L. Zhang, C. Meng, Y. Inaba, X. Wang, A. Nitta, Y. Koma, K. Takeshita: Selective removal of radiocesium from micaceous clay for post-accident soil decontamination by temperature-controlled Mg-leaching in a column ; *Journal of Hazardous Materials*, **Vol.387**, 121677(2020) .

(30) R. Mishima, Y. Inaba, S. Tachioka, M. Harigai, S. Watanabe, Jun Onoe, M. Nakase, T. Matsumura, K. Takeshita: Sorption Properties of Aluminum Hexacyanoferrate for Platinum Group Elements ; *Chemistry Letters*, **Vol.49, Issue 1**, pp.83-86(2019).

(31) S. Kanagawa, Z. Dong, T. Baikie, T. White and K.Takeshita, Synthesis and Characterization of Apatite Wasteforms Using Simulated Radioactive Liquid Waste, *Chemistry Letter*, **Vol.48**, **issue 8**, pp.881-884, 2019

(32) Y. Sasaki, K. Morita, M. Matsumiya, M. Nakase: Simultaneous separation of Am and Cm from Nd and Sm by multi-step extraction using the TODGA-DTPA-BA-HNO_3 system; *Radiochimica acta,* published online(2020).

(33) X. Yin, L. Zhang, M. Harigai, Xinpeng Wang, Shunyan Ning, M. Nakase, Yoshikazu Koma, Y. Inaba, K. Takeshita: Hydrothermal-treatment desorption of cesium from clay minerals: The roles of organic acids and implications for soil decontamination; *Water Research*, **Vol.177**, 115804(2020).

(34) Kazama, H.; Tsushima, S.; Takao, K. "Crystallization of Anhydrous Proton from Acidic Aqueous Solution with Diamide Building Block" *Cryst. Growth Des.* **2019**, *19*, 6048-6052.

(35) Zheng, Z.; Arai, T.; Takao, K. "Kinetic and Thermodynamic Requirements to Extend Solvent Compatibility in Thermal-Assisted Extraction of Inert Platinum Group Metals" *ACS Sustainable Chem. Eng.* **2019**, *11*, 9750-9753.

(36) Mashita, T.; Tsushima, S.; Takao, K. "Photocatalytic Oxygenation of Cyclohexene Initiated by Excitation of $[UO_2(OPCyPh_2)_4]^{2+}$ under Visible Light" *ACS Omega*, **2019**, *4*, 7194-7199.

(37) Takao, K.; Kazama, H.; Ikeda, Y.; Tsushima, S. "Crystal Structure of Regularly Th-Symmetric $[U(NO_3)_6]^{2-}$ Salts with Hydrogen Bond Polymers of Diamide Building Blocks" *Angew. Chem. Int. Ed.* **2019**, *58*, 240-243.

(38) Takao, K.; Mori, T.; Kubo, M.; Uehara, A.; Ikeda, Y. "Wet chemical processing for nuclear waste glass to retrieve radionuclides" *J. Hazard. Mater.* **2019**, *362*, 368-374.

(39) Osamu Odawara, Anna Gubarevich, Hiroyuki Wada: Advances on Self-propagating High-temperature Synthesis for Efficient Improvements of Underground and Space Environments Utilizations; *Ceramics in Modern Technologies*, Vol.**1**, No.1, 20-24 (2019).

(40) Shigeki Shiba and Hiroshi Sagara: Fast reconstruction of Bayesian iterative approximation in passive gamma-ray tomography; *J. Nucl. Sci. Technol*., DOI: 10.1080/00223131.2019.1699192, Volume 57, No. 5, Pages 546-552, 2019.

(41) Takeshi Aoki, Hiroshi Sagara, Chi Young Han: Material attractiveness evaluation of inert matrix fuel for nuclear security and non-proliferation; *Annals of Nuclear Energy*, Volume 126, 2019, Pages 427-433.

(42) Rie Fujioka, Hiroshi Sagara, Chi Young Han: An innovative fast reactor core design for rapid reduction of separated Pu and its proliferation concerns; *Annals of Nuclear Energy*, Volume 125, 2019, Pages 148-156.

(43) Riku Akatsu, Toru Tsunoura, Katsumi Yoshida, Toyohiko Yano, Yukio Kishi: Densification Behavior of Yttrium Oxyfluoride Ceramics by Rate Controlled Sintering and Their Mechanical Properties; *Japanese Journal of Applied Physics*, Vol.**58**, SEEG02 (2019).

(44) Kenji Miyashita, Toru Tsunoura, Katsumi Yoshida, Toyohiko Yano, Yukio Kishi: Fluorine and oxygen plasma exposure behavior of yttrium oxyfluoride ceramics; *Japanese Journal of Applied Physics*, Vol.**58**, SEEC01 (2019).

(45) Toru Tsunoura, Katsumi Yoshida, Toyohiko Yano, Takuya Aoki, Toshio Ogasawara: Fabrication and bending behavior of amorphous SiC-fiber-reinforced Si-Co eutectic alloy composites at elevated temperatures; *Composites Part B*, Vol.**164**, 769-777 (2019).

(46) Toru Tsunoura, Katsumi Yoshida, Toyohiko Yano, Takuya Aoki, Toshio Ogasawara: Oxidation mechanisms of SiC-fiber-reinforced Si eutectic alloy matrix composites at elevated temperatures; *Journal of the American Ceramic Society*, Vol.**102**, No.10, 6309-6321 (2019).

(47) Yuhao Jin, Katsumi Yoshida, Zhengcao Li, Desheng

Ai, Tadashi Maruyama, Toyohiko Yano: Investigation of kinetic recovery process in low dose neutron-irradiated nuclear graphite by thermal annealing; *Journal of Nuclear Science and Technology*, Vol.**56**, No. 6, 533-540 (2019).

(48) Muhammad Fajar, Anna Gubarevich, Ryosuke S.S. Maki, Tetsuo Uchikoshi, Tohru S. Suzuki, Toyohiko Yano, Katsumi Yoshida: Effecr of Al_2O_3 adition on texturing in a rotating strong magnetic field and densification of B_4C; *Ceramics International*, Vol.4**5**, No. 15, 18222-18228 (2019).

(49) Hiroaki Ashizawa, Katsumi Yoshida: Effect of the microstructure of yttria ceramics on their plasma corrosion behavior; *Ceramics International*, Vol.4**5**, No.17, 21162-21167 (2019).

(50) K. Ishii, Y. Izumoto, T. Matsuyama, K. Fukutsu, Y. Sakai, Y. Oguri, H. Yoshii: Optimization of a Primary X-ray Filter for X-ray Fluorescence Analysis of Uranium and Plutonium; *X-Ray Spectrom.*, Vol. **48**, Issue 3, pp. 360-365 (2019).

(51) Y. Izumoto, T. Matsuyama, K. Ishii, Y. Sakai, Y. Oguri, H. Yoshii: X-ray Fluorescence Analysis of Samples Simulating Blood Collected from Uranium-Contaminated Wounds; *X-Ray Spectrom*., Vol. **48**, Issue 3, pp. 438-442 (2019).

(52) Okawa A, Morioka T, Imaoka T, Kakinuma S, Matsumoto Y: Differential expression of DNA-dependent protein kinase catalytic subunit in the brain of neonatal mice and young adult mice; *Proceedings of the Japan Academy Series B*, Vol.96, No.5, 171-179 (2020).

(53) Kitagawa M, Someya M, Hasegawa T, Mikami T, Asaishi K, Hasegawa T, Matsumoto Y, Kutomi G, Takemasa I, Sakata K: Influence of XRCC4 expression by breast cancer cells on ipsilateral recurrence after breast-conserving therapy; *Strahlentherapie und Oncologie*, 195, 648-658 (2019).

(54) Nishikubo K, Izumi Y, Matsumoto Y, Fujii K, Matsuo K, Yokoya A: Structural analysis of DNA repair protein XRCC4 applying circular dichroism in an aqueous solution; Radiation Protection and Dosimetry, Vol.182, No.1-2, *3*6-39 (2019).

(55) Mikio Shimada, and Tomoko Miyake: Is ionizing radiation-induced DNA damage in derived keratinocytes: a useful model for radiotoxicity research?; *International Journal of Oncology, Biology, Physics*, Vol.**106**, No.3, pp. 650 (2020).

(56) Mikio Shimada, Kaima Tsukada, Nozomi Kagawa, Yoshihisa Matsumoto: Reprogramming and differentiation-dependent transcriptional alteration of DNA damage response and apoptosis genes in human induced pluripotent stem cells; *Journal of Radiation Research*, Vol. **60**, No.6, pp.719-728(2019).

(57) Tomoko Miyake, Mikio Shimada, Yoshihisa Matsumoto, Akitoshi Okino: DNA Damage Response After Ionizing Radiation Exposure in Skin Keratinocytes Derived from Human-Induced Pluripotent Stem Cells; *International Journal of Oncology, Biology, Physics*, Vol.**105**, No.1, pp. 193-205 (2019).

(58) Heamin Ko, Myung-Ki Cheoun, Eunja Ha, Motohiko Kusakabe, Takehito Hayakawa, Hirokazu Sasaki, Toshitaka Kajino, Masa-aki Hashimoto, Masaomi Ono, Mark Dennis Usang, Satoshi Chiba, Ko Nakamura, Alexey Tolstov, Ken'ichi Nomoto, Toshihiko Kawano, Grant J. Mathews: Neutrino Process in Core-collapse Supernovae with Neutrino Self-interaction and MSW Effects; *The Astrophysical Journal Letters*, Vol.**891**, pp. L24-1-6 (2020).

(59) Chikako Ishizuka, X. Zhang, Mark Dennis Usang, Fedir A. Ivanyuk, Satoshi Chiba: Effect of the doubly magic shell closures in ^{132}Sn and ^{208}Pb on the mass distributions of fission fragments of superheavy nuclei; *Physical Review C*, Vol.**101**, Rapid communications, pp. 011601-1-5 (2020).

(60) Toshio Wakabayashi, Yoshiaki Tachi, Makoto Takahashi, Satoshi Chiba, Naoyuki Takaki: Study on method to achieve high transmutation of LLFP using fast reactor; *Scientific Reports*, Vol. **9**, pp. 19156-1-14 (2019).

(61) Kun Ratha Kean, Katsuhisa Nishio, Kentaro Hirose, Jochen Vermeulen, Hiroyuki Makii, R. Orlandi, K. Tsukada, Andreyev Andrei, Igor Tsekhanovich, Satoshi Chiba: Validation of the multinucleon transfer method for the determination of the fission barrier height; *Physical Review C*, Vol.**100**, pp. 014611-1-6 (2019).

(62) V. L. Litnevsky, Fedir A. Ivanyuk, G. I. Kosenko, Satoshi Chiba: Description of the mass-asymmetric fission of the Pt isotopes, obtained in the reaction ^{36}Ar+^{142}Nd within the two-stage fusion-fission model; *Physical Review C*, Vol. **99**, pp. 054624-1-8 (2019).

(63) Senna Fukukawa, Atsushi Nezu, Hiroshi Akatsuka: Non-Equilibrium Characteristics of Vibrational and Rotational Temperatures of N_2-B and C States Puffed onto Argon Arc Jet Plume; *Japanese Journal of Applied Physics*, Vol. **58**, No. 9, 096003 (2019).

(64) Jun Takeda, Atsushi Nezu, Hiroshi Akatsuka: $\boldsymbol{E} \times \boldsymbol{B}$ Drift of Electrons in a Radial Electric Field and Longitudinal Magnetic Field; *IEEE Transactions on Plasma Science*, Vol. **47**, No. 9, pp. 4250-4259 (2019).

(65) Masao Kinoshita, Takayuki Fuyuto, Yoshiyuki Mandokoro, Akimitsu Sugiura, Hiroshi Akatsuka: Measurement of Temperature of Spark-Discharge Plasma in Engine Cylinder; *Transactions of the JSME* (in Japanese), Vol. **86**, No. 883, 19-00319 (2020).

(66) Badari Narayana Rao, Shintaro Yasui, Yefei Han, Yosuke Hamasaki, Tsukasa Katayama, Takahisa Shiraishi, Takanori Kiguchi, Mitsuru Itoh: Redox-Based Multilevel Resistive Switching in $AlFeO_3$ Thin-Film Heterostructures; *ACS Appl. Electro. Mater.*, Vol. **2**, pp. 1065-1073(2020).

(67) Sou Yasuhara, Yosuke Hamasaki, Tsukasa Katayama, Takahiro Ao, Yoshiyuki Inaguma, Hajime Hojo, Maarit Karppinen, Anish Philip, Shintaro Yasui, Mitsuru Itoh: Modulating the Structure and Magnetic Properties of ε-Fe_2O_3 Nanoparticles via Electrochemical Li+ Insertion; *Inorg. Chem.*, Vol. **59**, pp. 4357-4365(2020).
(68) Badari Narayana Rao, Shintaro Yasui, Tsukasa Katayama, Ayako Taguchi, Hiroki Moriwake, Yosuke Hamasaki and Mitsuru Itoh: Investigation of ferrimagnetism and ferroelectricity in $Al_xFe_{2-x}O_3$ thin films; *J. Mater. Chem. C*, Vol. **8**, pp. 706-714(2020).
(69) Yosuke Hamasaki, Tsukasa Katayama, Shintaro Yasui, Takahisa Shiraishi, Akihiro Akama, Takanori Kiguchi, Tomoyasu Taniyama and Mitsuru Itoh: Switchable third $ScFeO_3$ polar ferromagnet with $YMnO_3$-type structure; *J. Mater. Chem. C*, Vol. **8**, pp. 4447-4452(2020).
(70) Akira Hosono, Yuji Masubuchi, Shintaro Yasui, Masaki Takesada, Takashi Endo, Mikio Higuchi, Mitsuru Itoh, and Shinichi Kikkawa: Ferroelectric $BaTaO_2N$ Crystals Grown in a $BaCN_2$ Flux; *Inorg. Chem.*, Vol. **58**, pp. 16752-16760(2019).
(71) Sou Yasuhara, Shintaro Yasui, Takashi Teranishi, Yumi Yoshikawa, Tomoyasu Taniyama and Mitsuru Itoh: The effects of $BaTiO_3$ nanodots density support on epitaxial $LiCoO_2$ thin-film for high-speed rechargeability; *Electrochem. Commun.*, Vol. **109**, p. 106604(2019).
(72) Sou Yasuhara, Shintaro Yasui, Takashi Teranishi, Yumi Yoshikawa, Tomoyasu Taniyama and Mitsuru Itoh: The effect of relative permittivity of surface supporting materials for high-speed rechargeable $LiCoO_2$ cathode film; *J. Power Sources*, Vol. **441**, p. 227194(2019).
(73) Yoshitaka Ehara, Takao Shimizu, Shintaro Yasui, Takahiro Oikawa, Takahisa Shiraishi, Hiroki Tanaka, Noriyuki Kanenko, Ronald Maran, Tomoaki Yamada, Yasuhiko Imai, Osami Sakata, Nagarajan Valanoor, and Hiroshi Funakubo: Ferroelastic domain motion by pulsed electric field in (111)/(11-1) rhombohedral epitaxial $Pb(Zr_{0.65}Ti_{0.35})O_3$ thin films: Fast switching and relaxation; *Phys. Rev. B*, Vol. **100**, p. 104116(2019).
(74) Shintaro Yasui, Tsukasa Katayama, Takuya Osakabe, Yosuke Hamasaki, Tomoyasu Taniyama, Mitsuru Itoh: Ferroelectric and Ferrimagnetic properties of e-$Rh_xFe_{2-x}O_3$ thin films; *J. Ceram. Soc. Jpn.*, Vol. **127**, pp. 474-477(2019).
(75) In-Tae Bae, Shintaro Yasui, Tomohiro Ichinose, Mitsuru Itoh, Takahisa Shiraishi, Takanori Kiguchi, and Hiroshi Naganuma: Short Range Biaxial Strain Relief Mechanism within Epitaxially Grown $BiFeO_3$; *Sci. Rep.*, Vol. **9**, p. 6715(2019).
(76) Mochizuki, H., Consideration on Nusselt numbers of liquid metals flowing in tubes, Nuclear Engineering and Design, 351, (2019), pp.1-19.

International Conference Proceedings

(1) Kazuki Kuwagaki, Jun Nishiyama, Toru Obara: Thermal Hydraulic Analysis for a Breed and Burn Core with Spiral Fuel Shuffling; *Proc. of Reactor Physics Asia Conference 2019 (RPHA19)*, December 2-3, 2019, Osaka, Japan, RPHA19-1087 (2019).
(2) Hoang Hai Nguyen, Jun Nishiyama, Toru Obara: Monte Carlo Based Analysis for CANDLE Burning Reactor; *Proc. of Reactor Physics Asia Conference 2019 (RPHA19)*, December 2-3, 2019, Osaka, Japan, RPHA19-1088 (2019).
(3) Takeshi Muramoto, Jun Nishiyama, Toru Obara: Development of Criticality Safety Evaluation Method Based on the Actual Dynamic Behavior of the Fuel Debris in Water; *Proc. of Reactor Physics Asia Conference 2019 (RPHA19)*, December 2-3, 2019, Osaka, Japan, RPHA19-1091 (2019).
(4) Kodai Fukuda, Jun Nishiyama, Toru Obara: Radiation Dose by Criticality Accidents of Fuel Debris in Water; *Proc. of Reactor Physics Asia Conference 2019 (RPHA19)*, December 2-3, 2019, Osaka, Japan, RPHA19-1092 (2019).
(5) Hiroki Takezawa, Delgersaikhan Tuya, Toru Obara: Development of Integral Kinetic Model with Delayed Neutrons Effect for Criticality Accident Analysis of Fukushima Daiichi NPP Fuel Debris; *Proc. of Reactor Physics Asia Conference 2019 (RPHA19)*, December 2-3, 2019, Osaka, Japan, RPHA19-1085 (2019).
(6) Toru Obara, Delgersaikhan Tuya: Development of super critical transient MIK code and its application to GODIVA core; *Proc. of ICNC2019 – 11th International Conference on Nuclear Criticality Safety*, September 15-20, 2019 – Paris, France, A93237TO (2019).
(7) Takeshi Muramoto, Jun Nishiyama, Toru Obara: Numerical analysis of criticality of fuel debris falling in water by coupling computational fluid dynamics and the continuous energy Monte Carlo code; *Proc. of ICNC2019 – 11th International Conference on Nuclear Criticality Safety*, September 15-20, 2019 – Paris, France, A93049MT (2019).
(8) Kodai Fukuda, Delgersaikhan Tuya, Jun Nishiyama, Toru Obara: Supercritical kinetic analysis in a simple fuel debris system by MIK code; *Proc. of ICNC2019 – 11th International Conference on Nuclear Criticality Safety*, September 15-20, 2019 – Paris, France, A93242KF (2019).
(9) Y. Maruyama, K. Nakajima, H. Takasu, Y. Kato: Development of solid oxide electrolysis cell for CO_2 reduction in active carbon recycling energy system for iron-making process; the Fifth International Symposium on Innovative Materials and Processes in Energy Systems (IMPRES2019), P124, Poster presentation, 22(20-23) October, 2019, Kanazawa,

Japan
(10) J. Kaneko, H. Takasu, K. Fujioka, Y. Kato: Development of thermochemical energy storage system by using metal chloride/ammonia system; the Fifth International Symposium on Innovative Materials and Processes in Energy Systems (IMPRES2019), P106, Poster presentation, 22(20-23) October, 2019, Kanazawa, Japan
(11) R. Guo, S. Funayama, H. Takasu, Y. Kato: Development of nano-modified material for thermochemical energy storage; the Fifth International Symposium on Innovative Materials and Processes in Energy Systems (IMPRES2019), A113, 21(20-23) October, 2019, Kanazawa, Japan
(12) H. Miura, S. T. Kim, H. Takasu, Y. Aristov, A. Shkatulov, Y. Kato: Study of the salt-doped MgO for thermochemical energy storage by reacting with CO_2; the Fifth International Symposium on Innovative Materials and Processes in Energy Systems (IMPRES2019), P104, Poster presentation, 22(20-23) October, 2019, Kanazawa, Japan
(13) S. Funayama, H. Takasu, K. Fujioka, Y. Kato: Thermochemical storage performance analysis of a packed bed reactor using calcium oxide/calcium hydroxide/water reaction system; the Fifth International Symposium on Innovative Materials and Processes in Energy Systems (IMPRES2019), P109, Poster presentation, 22(20-23) October, 2019, Kanazawa, Japan
(14) H. Takasu, S. T. Kim, Y. Kato: Study of additive effect on lithium orthosilicate and carbon dioxide reaction; the Fifth International Symposium on Innovative Materials and Processes in Energy Systems (IMPRES2019), P109, Poster presentation, 21(20-23) October, 2019, Kanazawa, Japan.
(15) Y. Kato: [Invited Lecture]: “Active Carbon Recycling Energy System (ACRES) for the Next Low-Carbon Society”; 5th International Workshop on Heat/Mass Transfer Advances for Energy Conservation and Pollution Control, August 14(13-16), 2019, Novosibirsk, Russia
(16) Rui Guo, Hiroki Takasu, Shigehiko Funayama, Seon Tae Kim, Yukitaka Kato: Development of composite pellet of calcium carbonate for thermochemical energy storage; Asian Pacific Confederation of Chemical Engineering (APCChE2019), 101079-1, 2019/09/26, Sapporo.
(17) T. Okamura, E. Minari, M. Nakase, H. Asano, K. Takeshita: Reduction of geological disposal area by introducing partitioning technologies under conditions of high burn-up fuel and high content vitrified waste; International Conference on the Management of Spent Fuel from Nuclear Power Reactors (SFM) 2019, Vienna, Austria, June 24-28, 2019.
(18) H. Asano, T. Okamura, E. Minari, M. Nakase, K. Takeshita: Cross-sectoral study on nuclear energy system for less-impacted geological disposal of high-level radioactive waste in consideration of variation of spent nuclear fuel and technical feasibility of reprocessing and vitrification processes; International Conference on the Management of Spent Fuel from Nuclear Power Reactors (SFM) 2019, Vienna, Austria, June 24-28, 2019.
(19) M. Nakase, E. Minari, T. Okamura, H. Asano, H. Sagara, M. Saito, K. Takeshita: Effective use of ^{234}U in Th fuel cycle; International Conference on the Management of Spent Fuel from Nuclear Power Reactors (SFM) 2019, Vienna, Austria, June 24-28, 2019.
(20) E. Minari, T. Okamura, M. Nakase, H. Asano, K. Takeshita: Environmental Load Reduction of Geological Repository by Minor Actinide Separation; Utilization of MOX Fuel in Future Fuel Cycle System; nternational Conference on the Management of Spent Fuel from Nuclear Power Reactors (SFM) 2019, Vienna, Austria, June 24-28, 2019.
(21) N. Tsutsui, M. Nakase, S. Ito, Y. Ban, T. Matsumura, K. Takeshita: Extraction separation of minor actinides and lanthanides by 1,10-phenanthroline-2,9-diamide with phenyl group in nitric acid systems; GLOBAL2019, Seattle, USA, September 22-26, 2019.
(22) T. Matsumura, Y. Ban, H. Suzuki, Shinobu Hotoku, N. Tsutsui, T. Toigawa, K. Morita, Y. Tsubata: Development of SELECT Process Using CHON Extractants for Partitioning and Transmutation; GLOBAL2019, Seattle, USA, September 22-26, 2019.
(23) E. Minari, Ki Seob Sim, R. Yoshioka, H. Asano, K. Takeshita: Scenario analysis tool Nuclear Fuel Cycle Simulation System (NFCSS): Safety assessments in the context of spent fuel management and disposal; GLOBAL2019, Seattle, USA, September 22-26, 2019.
(24) Zheng, Z.; Arai, T.; Takao, K. "Rapid and Efficient Extraction of Inert Platinum Group Metals from HNO3(aq) at Elevated Temperature" *GLOBAL2019 International Nuclear Fuel Cycle Conferenc*e, The Westin Seattle, USA (Sep 22-26, 2019).
(25) Kubo, M.; Takao, K. "Alteration and Leaching Behavior of Simulated Nuclear Waste Glass in Different Acidic Solutions" *GLOBAL2019 International Nuclear Fuel Cycle Conference*, The Westin Seattle, USA (Sep 22-26, 2019).
(26) Takao, K.; Mori, T.; Kubo, M.; Ikeda, Y. "Development of Acid Leaching Method to Retrieve High-Level Wastes from Nuclear Waste Glass" *GLOBAL2019 International Nuclear Fuel Cycle Conference*, The Westin Seattle, USA (Sep 22-26, 2019).
(27) Inoue, T.; Kazama, H.; Tsushima, S.; Takao, K. "Desgn of Molecular Structures of Uranyl Nitrate Coordination Polymers Bridged by Double-Headed 2-Pyrrolidone Derivatives" *Migration 2019*, PA3-14, Kyoto Univ. Japan (Sep 15-20, 2019).
(28) Takao, K.; Tsushima, S. "Photochemical Reduction of $[UO_2(CO_3)_3]^{4-}$ with Borohydrides" *Migration 2019*,

PA4-6, Kyoto Univ. Japan (Sep 15-20, 2019).
(29) Natsumi Mitsuboshi and Hiroshi Sagara: Feasibility study on innovative small and medium modular reactor with inherent nuclear safety, security, and non-proliferation features (1) Silicide fuel with MA and/or RepU; *Proc. 40th Annual Mtg. INMMJ Japan Chapter*, P4001, 2019.
(30) Tsukasa Amano, Hiroshi Sagara, Chi Young Han: Feasibility study on light water reactor fuel with inherent safety and non-proliferation features (2) U-Pu Silicide Fuel; *Proc. 40th Annual Mtg. INMMJ Japan Chapter*, P4002, 2019.
(31) Ryo Aoyagi, Sunil S. Chirayath, Hiroshi Sagara: Nonproliferation features of molten salt fast reactor; *Proc. 40th Annual Mtg. INMMJ Japan Chapter*, P4003, 2019.
(32) Yuichi Kagayama, Hiroshi Sagara and Chi Young Han: Characteristics of Nuclide Composition in Spent Nuclear Fuel from Light Water Reactors for Nuclear Forensics Research Plan for finding out new discrimination indices; *Proc. 40th Annual Mtg. INMMJ Japan Chapter*, P4004, 2019.
(33) Kim Wei Chin, Hiroshi Sagara, Chi Young Han and Rei Kimura: Applicability Study of Photofission Reaction to Identify High-Enriched Uranium by utilizing the Bremsstrahlung Photon (2) Selection of incident electron energies and validation of PFRR principle; *Proc. 40th Annual Mtg. INMMJ Japan Chapter*, P4005, 2019.
(34) Shigeki Shiba and Hiroshi Sagara: Development of Image Reconstruction Technology using Passive Gamma Emission Tomography (2) Reconstruction of Gamma-ray Sources in Mock-up Fuel Assembly; *Proc. 40th Annual Mtg. INMMJ Japan Chapter*, P4006, 2019.
(35) Sho NAKAGUKI, Hiroshi SAGARA, and Chi Young HAN: Feasibility of Application of DDSI Assay Technique for Nuclear Material Quantification in Various Radioactive Waste Forms (1)Research Plan; *Proc. 40th Annual Mtg. INMMJ Japan Chapter*, P4007, 2019.
(36) Takaya Tokuda, Shigeki Shiba, Hiroshi Sagara: A study of the NDA Technology using Passive Gamma and Neutron Emission Tomography (1) The research plan of application to Passive Neutron Emission Tomography for partial defect verification; *Proc. 40th Annual Mtg. INMMJ Japan Chapter*, P4008, 2019.
(37) Koji Tsutsui and Hiroshi Sagara: Institutional and Technical Measures for Rational Nuclear Safeguards of Next Generation Nuclear Fuel Cycle (1) Research Plan; *Proc. 40th Annual Mtg. INMMJ Japan Chapter*, P4009, 2019.
(38) Hamza El-Asaad, Hiroshi Sagara, Chi Young Han, Haruyasu Nagai: Development of a user-friendly interface for atmospheric dispersion database and its application for nuclear emergency preparedness-Application for optimizing measurement points for effective detection of released radioactive nuclides; *Proc. 40th Annual Mtg. INMMJ Japan Chapter*, P4011, 2019.
(39) Shuichiro Ebata, Chi Young Han , Hiroshi Sagara, Yoshihisa Matsumoto, Satoshi Chiba, Noriyosu Hayashizaki1 Masako Ikegami, Akira Omoto, Kenji Takeshita, Tatsuya Katabuchi, Hiroshige Kikura, and Koichiro Takao: Nuclear Regulation Human Resource Development Program in Tokyo Tech "The Advanced Nuclear 3S Education and Training (ANSET)" – (4) Implementation Status FY2019 -; *Proc. 40th Annual Mtg. INMMJ Japan Chapter*, 4015, 2019.
(40) Chi Young HAN, Shuichiro EBATA, Tatsuya KATABUCHI, Satoshi CHIBA, and Hiroshi SAGARA: Nuclear Regulation Human Resource Development Program in Tokyo Tech"The Advanced Nuclear 3S Education and Training (ANSET)" (5) Radiation Disaster Response Exercise; *Proc. 40th Annual Mtg. INMMJ Japan Chapter*, 4016, 2019.
(41) Katsumi Yoshida, Chin-Chet See, Anna Gubarevich, Toyohiko Yano: Effects of aluminum, boron and carbon additives on microstructure of porous silicon carbide ceramics and their properties; Materials Today; Proceedings, Vol. **16**, Part 1, 65-71 (2019).
(42) Toru Tsunoura, Katsumi Yoshida, Toyohiko Yano, Takuya Aoki, Toshio Ogasawara: High temperature bending behavior of polycrystalline Si and SiC particle-reinforced Si matrix composites; Materials Today; Proceedings, Vol. **16**, Part 1, 78-87 (2019).
(43) Jelena Maletaškić, Jelena Luković, Katsumi Yoshida, Toyohiko Yano, Ryosuke S.S. Maki, Anna Gubarevich, Branko Matović: High-temperature synthesis and characterization of boron suboxide (B_6O) and boron containing hard materials; Materials Today; Proceedings, Vol. **16**, Part 1, 95-101 (2019).
(44) Anna V. Gubarevich, Riki Tamura, Jelena Maletaskić, Katsumi Yoshida, Toyohiko Yano: Effect of aluminium addition on yield and microstructure of Ti_3SiC_2 prepared by combustion synthesis method; Materials Today; Proceedings, Vol. **16**, Part 1, 102-108 (2019).
(45) Branko Matović, Jelena Maletaškić, Katsumi Yoshida, Toyohiko Yano: Synthesis, characterization and sintering of fluorite and pyrochlore-type compounds: $Pr_2Zr_2O_7$, $Sm_2Zr_2O_7$ and $PrSmZr_2O_7$; Materials Today; Proceedings, Vol. **16**, Part 1, 156-162 (2019).
(46) Ryosuke S.S. Maki, Muhammad Fajar, Jelena Maletaskic, Anna V. Gubarevich, Katsumi Yoshida, Toyohiko Yano, Tohru S. Suzuki, Tetsuo Uchikoshi: Evaluation of thermal shock fracture resistance of B_4C/CNT composites with a high-frequency induction-heating furnace; Materials Today; Proceedings, Vol. **16**, Part 1, 137-143 (2019).
(47) Mikio Shimada, Kaima Tsukada, Tomoko MIyake, Norie Kanzaki, Hiromi Yanagihara, Yoshihisa Matsumoto. Transcriptional alteration of DNA damage response genes after ionizing radiation exposure in induced pluripotent stem cells, *Radiation*

Research Society 65th Annual International Meeting, Nov. 2019.

(48) Mikio Shimada, Kaima Tsukada, Nozomi Kagawa, Yoshihisa Matsumoto. Analysis of mechanism of DNA repair machinery and cell death in induced pluripotent stem cells, *International Congress of Radiation Research 2019*, Aug. 2019.

(49) Anie Day Asa De Castro, Rujira Wanotayan, Mikio Shimada, Mukesh Kumar Sharma, Yoshihisa Matsumoto. Functional Analysis of Disease-associated XRCC4 Mutations and its implication in DNA Repair and Immune System, *International Congress of Radiation Research 2019*, Aug. 2019.

(50) Akitoshi Okino, Satoshi Kohno, Tomoko Miyake, Yuma Suenaga, Takahiro Iwai, Mikio Shimada, Yoshihisa Matsumoto, Koichi Chiba. Development of Droplet Injection ICP-AES/MS and Elemental Analysis of Single Human Cancer Cells, *ILASS-Americas*, p. 56, May. 2019.

(51) K. R. Kean, T. Nishikawa, Y. Iwata: Perturbation Scheme for the Effective Nuclear Force; JPS Conf. Proc., 010018 (2020).

(52) Hiroshi Akatsuka: Optical Emission Spectroscopic Analysis for Diagnostics of Electron Density and Temperature in Non-Equilibrium Plasmas; *XXXIV International Conference on Phenomena in Ionized Gases (XXXIV ICPIG) and the 10th International Conference on Reactive Plasmas (ICRP-10)*, July 14-19, 2019, Sapporo, Japan, TL-14 [Topical Invited Lecture].

(53) Thijs van der Gaag, Hiroshi Onishi, Hiroshi Akatsuka: Determination of the EEDF by Continuum Spectrum Analysis of Atmospheric Pressure Plasma Using a Genetic Algorithm; *XXXIV International Conference on Phenomena in Ionized Gases (XXXIV ICPIG) and the 10th International Conference on Reactive Plasmas (ICRP-10)*, July 14-19, 2019, Sapporo, Japan, PO16PM-024.

(54) Shota Yamada, Atsushi Nezu, Hiroshi Akatsuka: Spectroscopic Study of CO Excited States in Microwave Discharge CO_2 Plasma; *XXXIV International Conference on Phenomena in Ionized Gases (XXXIV ICPIG) and the 10th International Conference on Reactive Plasmas (ICRP-10)*, July 14-19, 2019, Sapporo, Japan, PO18AM-029.

(55) Noritsugu Kamata, Narong Mungkung, Toshifumi Yuji, Yoshifumi Suzaki, Hiroshi Akatsuka: An Evaluation of a Vacuum Arc Instability Phenomenon with the Silver-Palladium Compound Material on the Cathode Spot; *5th International Conference on Applied Electrical and Mechanical Engineering (5^{th} ICAEME) 2019*, September 4 – 6, 2019, Nakon Phanom, Thailand, OP-03.

(56) Hiroshi Akatsuka, Hiroshi Onishi, Thijs van der Gaag, Atsushi Nezu: Optical Emission Spectroscopic (OES) Analysis of Electron Temperature and Density in Atmospheric-Pressure Non-Equilibrium Argon Plasmas, *3rd Asia-Pacific Conference on Plasma Physics (AAPPS-DPP3)*, November 4-8, 2019, Hefei, China, A-I16 [Invited Talk].

(57) June Konami, Atsushi Nezu, Hiroshi Akatsuka: Radial Dependence of Rotational Temperature of N_2 and N_2^+ Molecules in Microwave Discharge Nitrogen Plasma; *2019 International Symposium on Dry Process*, November 21-22, 2019, Hiroshima, Japan, pp. 91-92, P-18.

(58) Thijs van der Gaag, Hiroshi Akatsuka: A Machine Learning Approach to Determine Arbitrary EEDF of Atmospheric Pressure Plasma from OES Continuum Spectrum Analysis; *The 11th Asia Pacific International Symposium on the Basics and Applications of Plasma Technology (APSPT11)*, December 11-14, 2019, Kanazawa, Japan, OC-2.

(59) Fuminori Yamazaki, Atsushi Nezu, Hiroshi Akatsuka: Diagnostics of Electron Temperature and Density of Low-pressure Microwave Discharge Ar Plasma by Optical Emission Spectroscopy Based on Collisional Radiative Model; *The 11th Asia Pacific International Symposium on the Basics and Applications of Plasma Technology (APSPT11)*, December 11-14, 2019, Kanazawa, Japan, B-14.

(60) Kiyoyuki Yambe, Naoya Kuramoto, Hiroshi Akatsuka: Current Reflection Due to Interaction between Plasma and Metal Conductor in Atmospheric Pressure Non-Thermal Equilibrium Plasma; *The 11th Asia Pacific International Symposium on the Basics and Applications of Plasma Technology (APSPT11)*, December 11-14, 2019, Kanazawa, Japan, P1-2.

(61) Shota Yamada, Yuki Morita, Atsushi Nezu, Hiroshi Akatsuka: Rotational Non-Equilibrium of CO Excited States in Microwave Discharge CO_2 Plasma; *72nd Annual Gaseous Electronics Conference (GEC)*, October 28 – November 1, 2019, College Station, TX, USA, FT1.00015.

(62) Thijs Van Der Gaag, Hiroshi Akatsuka: Genetic-Algorithm-Assisted Reconstruction of Arbitrary EEDF of Atmospheric-Pressure Plasma Using Optical Emission Spectroscopic Measuremen; *72nd Annual Gaseous Electronics Conference (GEC)*, October 28 – November 1, 2019, College Station, TX, USA, FT1.00031.

(63) Hiroshi Akatsuka, Hiroshi Onishi, Fuminori Yamazaki, Atsushi Nezu: Electron Temperature Measurement of Atmospheric-pressure Non-Equilibrium Ar Plasma by Line Intensities with CR Model and by Continuum Emissivity; *72nd Annual Gaseous Electronics Conference (GEC)*, October 28 – November 1, 2019, College Station, TX, USA, FT1.00032.

(64) Shuichiro Okada, Atsushi Nezu, Hiroshi Akatsuka: Experimental Study of Plasma-Parameter Dependence of High-Pressure Microwave Discharge on External Magnetic Field; *ISPlasma2020/IC-PLANTS2020*, March 8-11, 2020, Nagoya, Japan, 1027, 10P3-3.

(65) Kento Kishida, Takashi Ogura, Hiroshi Akatsuka:

Analysis of the Sheath in the Weakly Ionized Plasma by the Particle Simulation, *ISPlasma2020/IC-PLANTS2020*, March 8-11, 2020, Nagoya, Japan, 1066, 10P3-4.

(66) Hugo Lavigne, Tomohiro Shiroi, Atsushi Nezu, Kiyoyuki Yambe, Hiroshi Akatsuka: Optical Emission Spectroscopic Measurement of Electron Temperature of Atmospheric-Pressure Non-Equilibrium Ar-CO_2 Plasma; *ISPlasma2020/IC-PLANTS2020*, March 8-11, 2020, Nagoya, Japan, Oral 1209, 09pB01O.

Oral Presentation in international or domestic conferences

(1) Toru Obara: Reactor Physics in SMR development; *Proc. of 2019 autumn meeting of Atomic Energy Society of Japan*,1J_PL01(2019).

(2) Anton Smirnov, Ekaterina Bogdanova, Georgy Tikhomirov, Hiroki Takezawa, Jun Nishiyama, Toru Obara: Criticality calculations of fuel debris in various conditions during falling down; Proc. of 2020 Annual meeting of Atomic Energy Society of Japan, 1I01 (2020).

(3) Takeshi Muramoto, Jun Nishiyama, Toru Obara: Criticality Safety Evaluation of Powder Fuel Debris using DEM and MPS Method; *Proc. of 2020 Annual meeting of Atomic Energy Society of Japan*, 1I02 (2020).

(4) Kodai Fukuda, Jun Nishiyama, Toru Obara: Radiolysis gas reactivity feedback effect on prompt supercritical transient analysis of fuel debris; *Proc. of 2020 Annual meeting of Atomic Energy Society of Japan*, 1I04 (2020).

(5) Kazuki Kuwagaki, Jun Nishiyama, Toru Obara: Characteristics of spent fuel from breed and burn fast reactor; *Proc. of 2020 Annual meeting of Atomic Energy Society of Japan*, 3H06 (2020).

(6) Sergei Ryzhov, Georgy Tikhomirov, Toru Obara: Minor actinides transmutation technology optimization methods; *Proc. of 2020 Annual meeting of Atomic Energy Society of Japan*, 3H02 (2020).

(7) Aronne Travaglia, Kazuki Kuwagaki, Jun Nishiyama, Toru Obara: Possibility of Sodium Cooled Breed and Burn Fast Reactor with Rotational Fuel; P*roc. of 2020 Annual meeting of Atomic Energy Society of Japan*, 1H03 (2020).

(8) J. Kaneko, H. Takasu, Y. Kato: “Thermochemical energy storage material for metal chloride/annmonia reaction system”; JSME ICMS 2019 Winter Meeting, 20 December, 2019, Tokyo.

(9) Y. Kato: [Invited Lecture] Heat storage performance of high thermal conductivity composite using calcium hydroxide for thermochemical energy storage; *56th Japan Heat Transfer Symposium*, OS-I311, 31 June, 2019, Tokushima.

(10) S. Funayama, R.Guo, H. Takasu, Y. Kato: Heat storage performance of high thermal conductivity composite using calcium hydroxide for thermochemical energy storage; *56th Japan Heat Transfer Symposium*, 29-31 June, 2019, Tokushima.

(11) Rui GUO, Shigehiko FUNAYAMA, Hiroki TAKASU, Yukitaka KATO: Nano-modified materials for $CaO/H_2O/Ca(OH)_2$ thermochemical energy storage;*56th Japan Heat Transfer Symposium*, 29-31 June, 2019, Tokushima.

(12) Jiajun Li, Qianyun Li, Yoshinao Kobayashi. Determination of Gibbs Free Energy of Formation of Ni-rich Precipitate, *Annual Meeting of Atomic Energy Society of Japan*, Sep. 2019.

(13) Henghui Chen, Rizky Dwi Septian, Yoshinao Kobayashi. Thermodynamics of the B_2O_3-Cs_2O binary system, *Annual Meeting of Atomic Energy Society of Japan*, Sep. 2019.

(14) K. Takeshita, X. Yin: Recovery of Radioactive Cesium from Clay Minerals in Soil contaminated by Fukushima Dai-ichi Nuclear Power Plant accident; International Conference on Materials Research and Nanotechnology, Rome, Italy, June 10-12, 2019.

(15) S. Kanagawa, Z. Dong, Tom Baikie, T. White, Y. Aoyama, M. Iizuka, T. Hijikata,, K. Takeshita: Synthesis and Characterization of Simulated Nuclear Waste in Apatite Wasteforms; International Conference on Materials Research and Nanotechnology, Rome, Italy, June 10-12, 2019.

(16) T. Okamura, E. Minari, M. Nakase, H. Asano, K. Takeshita: Reduction of geological disposal area by introducing partitioning technologies under conditions of high burn-up fuel and high content vitrified waste; International Conference on the Management of Spent Fuel from Nuclear Power Reactors (SFM) 2019, Vienna, Austria, June 24-28, 2019.

(17) H. Asano, T. Okamura, E. Minari, M. Nakase, K. Takeshita: Cross-sectoral study on nuclear energy system for less-impacted geological disposal of high-level radioactive waste in consideration of variation of spent nuclear fuel and technical feasibility of reprocessing and vitrification processes; International Conference on the Management of Spent Fuel from Nuclear Power Reactors (SFM) 2019, Vienna, Austria, June 24-28, 2019.

(18) Y. Inaba, T. Hara, M. Harigai, K. Takeshita: Recovery and immobilization of Cs by functional porous glasses; 8th annual meeting of the Society for Remediation of Radioactive Contamination in Environment, Fukushima, Japan, July 10-11, 2019.

(19) K. Takeshita, X. Yin, Y. Inaba, M. Harigai, S. Watanabe, J. Onoe: Devlopment of subcritical water treatment system for remediation and reuse of contaminated soil and the volume reduction of waste; 1. Kinetics and equilibrium of Cs desorption by ion exchange under subcritical water condition; 8th annual meeting of the Society for Remediation of Radioactive Contamination in Environment, Fukushima, Japan, July 10-11, 2019.

(20) K. Takeshita, X. Yin, Y. Inaba, M. Harigai:

Devlopment of subcritical water treatment system for remediation and reuse of contaminated soil and the volume reduction of waste; 2. Continuous treatment of contaminated soil by column method; 8th annual meeting of the Society for Remediation of Radioactive Contamination in Environment, Fukushima, Japan, July 10-11, 2019.

(21) K. Takeshita: Separation of Platinum Group Metals in HNO3 Using Thiodglycolamide and Amide-containing Tertiary Amine Extractants; The 5th China Japan Academic Symposium on Nuclear Fuel Cycle (ASNFC2019), China, July 24-27, 2019.

(22) M. Nakase, K. Takeshita: Development of selective ligands for f-block elements differenciation -Relation between complex structure and coordination-; The 5th China Japan Academic Symposium on Nuclear Fuel Cycle (ASNFC2019), China, July 24-27, 2019.

(23) L. Zhang, M. Harigai, Y .Inaba, M. Nakase, K. Takeshita: Removal of Cs from Clay Minerals by Hydrothermal Treatment Using Organic Acids; The 5th China Japan Academic Symposium on Nuclear Fuel Cycle (ASNFC2019), China, July 24-27, 2019.

(24) S. Kanagawa, Z. Dong, T. Baikie, T. White, K. Takeshita: Synthesis and Characterization of Simulated Apatite-type Wasteforms Containing REE; The 5th China Japan Academic Symposium on Nuclear Fuel Cycle (ASNFC2019), China, July 24-27, 2019.

(25) R. Mishima, S. Tachioka, Y. Inaba, M. Harigai, S. Watanabe, J. Onoe, M. Nakase, K. Takeshita: Adsorption study of platinum group metals by Aluminium ferrocyanide from nitric acid solution; The 5th China Japan Academic Symposium on Nuclear Fuel Cycle (ASNFC2019), China, July 24-27, 2019.

(26) T. Hara, K. Yamashita, H. Takahashi, M. Harigai, Y. Inaba, M. Nakase, K. Takeshita: Recovery and immobilization of Cesium using functional porous glass; The 5th China Japan Academic Symposium on Nuclear Fuel Cycle (ASNFC2019), China, July 24-27, 2019.

(27) X. Yin, Y. Koma, Y. Inaba, K. Takeshita: Removal of Radioactive Cesium from Fukushima Contaminated Soil by Hot-pressing Water Extraction in a Column; Atomic Energy Society of Japan, 2019 Fall Meeting, Toyama, Japan, September 11-13, 2019.

(28) K. Takeshita, Y. Inaba, X. Yin, Y. Koma: Desorption of Cs+ from vermiculite by subcritical water ion-exchange method; Atomic Energy Society of Japan, 2019 Fall Meeting, Toyama, Japan, September 11-13, 2019.

(29) S. Kanagawa, Z. Dong, T. White, T. Hijikata, Y. Aoyama, K. Takeshita: Synthesis and Characterization of immobilization of Cs in Apatite Wasteforms Containing Al; Atomic Energy Society of Japan, 2019 Fall Meeting, Toyama, Japan, September 11-13, 2019.

(30) S. Watanabe, M. Harigai, Y. Inaba, M. Nakaya, K. Takeshita, J. Onoe: Development of cyano-group bridge-type coordination polymer with a high sorption charactersitic of Platinum-group elements for high quality and volume reduction of vitrified objects containing high-level raditoactive nuclear wastes (6) Analysis of Physical Factors in Metal Ion Sorption to Hexacyanoferrate by First-principles Calculations; Atomic Energy Society of Japan, 2019 Fall Meeting, Toyama, Japan, September 11-13, 2019.

(31) Y. Inaba, M. Harigai, S. Tachioka, R. Mishima, K. Saito, K. Takeshita, S. Watanabe, J. Onoe: Development of cyano-group bridge-type coordination polymer with a high sorption charactersitic of Platinum-group elements for high quality and volume reduction of vitrified objects containing high-level raditoactive nuclear wastes (5) Synthesis and sorption studies of aluminum ferrocyanide; Atomic Energy Society of Japan, 2019 Fall Meeting, Toyama, Japan, September 11-13, 2019.

(32) T. Okamura, E. Minari, M. Nakase, H. Asano, K. Takeshita: Interrelationship and the Effects of Introducing Separation Technologies in the Nuclear Fuel Cycle for Enhanced Radioactive Waste Management; GLOBAL2019, Seattle, USA, September 22-26, 2019.

(33) S. Kanagawa, Z. Dong, T. Baikie, T. White, Y. Aoyama, M. Iizuka, T. Hijikata,, K. Takeshita: Synthesis of Simulated Nuclear Waste immobilization in Apatite Wasteforms Containing Al.; GLOBAL2019, Seattle, USA, September 22-26, 2019.

(34) Y. Sasaki, K. Morita, M. Matsumiya, M. Nakase: Behavior of lanthanides and actinides for their mutual separation using extractants and masking agent; GLOBAL2019, Seattle, USA, September 22-26, 2019.

(35) N. Tsutsui, M. Nakase, S. Ito, Y. Ban, T. Matsumura, K. Takeshita: Extraction separation of minor actinides and lanthanides by 1,10-phenanthroline-2,9-diamide with phenyl group in nitric acid systems; GLOBAL2019, Seattle, USA, September 22-26, 2019.

(36) M. Nakase, T. Yamamura, Kenji Shirasaki, Mitsuie Nagai, Daiju Matsumura, T. Kobayashi, K. Takeshita: Study on U/Th separation by monoamide?immobilized hydrogel adsorbents; GLOBAL2019, Seattle, USA, September 22-26, 2019.

(37) T. Matsumura, Y. Ban, H. Suzuki, S. Hotoku, N. Tsutsui, T. Toigawa, K. Morita, Y. Tsubata: Development of SELECT Process Using CHON Extractants for Partitioning and Transmutation; GLOBAL2019, Seattle, USA, September 22-26, 2019.

(38) E. Minari, Ki Seob Sim, R. Yoshioka, H. Asano, K. Takeshita: Scenario analysis tool Nuclear Fuel Cycle Simulation System (NFCSS): Safety assessments in the context of spent fuel management and disposal;

GLOBAL2019, Seattle, USA, September 22-26, 2019.
(39) K. Takeshita, X. Yin, L. Zhang, T. Hara, M. Harigai, Y. Inaba: Utilization of X-ray analysis for radioactive Cs removal from contaminated soil in Fukushima and its immobilization; 55th Conference on X-ray analysis, Fukushima, Japan, October 30-31, 2019.
(40) Y. Inaba, R. Mishima, S. Tachioka, K. Saito, M. Harigai, K. Takeshita, S. Watanabe, J. Onoe: Adsorption of PGMs and Mo from high level liquid waste by Aluminium hexaferrocyanide; 33th annual meeting of the Japan Society on Adsorption, November 14-15, 2019.
(41) M. Nakase, B.J. Mincher, T.S. Grimes, K. Takeshita: Relation between structure of monoamide ligand and separation behavior of americyl from lanthanide; 38th Solvent Extraction Conference, Saga, Japan, November 20-21, 2019.
(42) K. Takeshita, X. Yin, S. Watanabe: Development of ion-exchange process in subcritical water for remediation of radioactive cesium from contaminated soil; 38th Solvent Extraction Conference, Saga, Japan, November 20-21, 2019.
(43) S. Kanagawa, Z. Dong, T. White, K. Takeshita: Irradiation effect of apatite ceramics containing heat generating nuclides; Atomic Energy Society of Japan, 2019 Spring Meetin, March 16-18, 2020.
(44) T. Sakuragi, H. Asano, E. Minari, T. Okamura, M. Nakase, K. Takeshita, Y. Inagaki, Y. Niibori, S. Sato: Technical options of radioactive waste management for the second half of the 21st Century, in consideration of Pu utilization and less environmentally impacted geological disposal(13) Challenge of waste treatment and disposal in Pu utilization by light water reactor; Atomic Energy Society of Japan, 2019 Spring Meeting, March 16-18, 2020.
(45) T. Okamura, E. Minari, K. Kawai, M. Nakase, H. Asano, K. Takeshita: Technical options of radioactive waste management for the second half of the 21st Century, in consideration of Pu utilization and less environmentally impacted geological disposal(14) Thermal property of spent MOX fuel and its effect on geological disposal; Atomic Energy Society of Japan, 2019 Spring Meeting, March 16-18, 2020.
(46) E. Minari, T. Okamura, M. Nakase, H. Asano, K. Takeshita: Technical options of radioactive waste management for the second half of the 21st Century, in consideration of Pu utilization and less environmentally impacted geological disposal(15) Study on setting a standard case of the MOX vitrified waste disposal and the effect of MA separation to the thermal property; Atomic Energy Society of Japan, 2019 Spring Meeting, March 16-18, 2020.
(47) H. Asano, T. Sakuragi, E. Minari, T. Okamura, M. Nakase, K. Takeshita, Y. Inagaki, Y. Nibori, S. Sato: Technical options of radioactive waste management for the second half of the 21st Century, in consideration of Pu utilization and less environmentally impacted geological disposal, (16) Load evaluation of geological disposal for MOX fuel-derived wastes; Atomic Energy Society of Japan, 2019 Spring Meeting, March 16-18, 2020.
(48) M. Nakase, Y. Aoyama, S. Tachioka, K. Morita, Y. Sasaki, K. Takeshita: Coordination and structural studies on complexes of f-block elements and amide-type-polyaminocalboxylic acid ligands; Atomic Energy Society of Japan, 2019 Spring Meeting, March 16-18, 2020.
(49) J. Onoe, S. Watanabe, Y. Inaba, M. Harigai, K. Takeshita: Development of cyano-group bridge-type coordination polymer with a high sorption characteristic of platinum-group elements for high quality and volume reduction of vitrified objects containing high-level radioactive nuclear wastes(7) Project outline and summary; Atomic Energy Society of Japan, 2019 Spring Meeting, March 16-18, 2020.
(50) S. Watanabe, M. Harigai, Y. Inaba, M. Nakaya, K. Takeshita, J. Onoe: Development of cyano-group bridge-type coordination polymer with a high sorption characteristic of platinum-group elements for high quality and volume reduction of vitrified objects containing high-level radioactive nuclear wastes(8) Analysis of physical factors on the metal sorption of ferrocyanide nanoparticles and examination of a coordination polymer with a high sorption characteristic; Atomic Energy Society of Japan, 2019 Spring Meeting, March 16-18, 2020.
(51) Y. Inaba, M. Harigai, R. Mishima, S. Tachioka, K. Saito, K. Takeshita, S. Watanabe, J. Onoe: Development of cyano-group bridge-type coordination polymer with a high sorption characteristic of platinum-group elements for high quality and volume reduction of vitrified objects containing high-level radioactive nuclear wastes(9) Synthesis and sorption studies of aluminum ferrocyanide; Atomic Energy Society of Japan, 2019 Spring Meeting, March 16-18, 2020.
(52) R. Mishima, Y. Inaba, S. Tachioka, M. Harigai, S. Watanabe, J. Onoe, M. Nakase, T. Matsumura, K. Takeshita: Development of cyano-group bridge-type coordination polymer with a high sorption characteristic of platinum-group elements for high quality and volume reduction of vitrified objects containing high-level radioactive nuclear wastes(10) Platinum-group elements sorption studies of aluminum ferrocyanide; Atomic Energy Society of Japan, 2019 Spring Meeting, March 16-18, 2020.
(53) K. Takeshita, Y. Inaba, M. Harigai, S. Watanabe, J. Onoe: Development of cyano-group bridge-type coordination polymer with a high sorption characteristic of platinum-group elements for high quality and volume reduction of vitrified objects containing high-level radioactive nuclear wastes(11) Process evaluation; Atomic Energy Society of Japan, 2019 Spring Meeting, March 16-18, 2020.
(54) Zheng, Z.; Arai, T.; Takao, K. "Rapid and Efficient Extraction of Inert Platinum Group Metals from

HNO3(aq) at Elevated Temperature" *GLOBAL2019 International Nuclear Fuel Cycle Conferenc*e, The Westin Seattle, USA (Sep 22-26, 2019).

(55) Kubo, M.; Takao, K. "Alteration and Leaching Behavior of Simulated Nuclear Waste Glass in Different Acidic Solutions" *GLOBAL2019 International Nuclear Fuel Cycle Conference*, The Westin Seattle, USA (Sep 22-26, 2019).

(56) Takao, K.; Mori, T.; Kubo, M.; Ikeda, Y. "Development of Acid Leaching Method to Retrieve High-Level Wastes from Nuclear Waste Glass" *GLOBAL2019 International Nuclear Fuel Cycle Conference*, The Westin Seattle, USA (Sep 22-26, 2019).

(57) Kazama, H., Inoue, T., Takao, K., Effects of Alkyl Chain Length of Bridging Moiety on Solubility of Uranyl Nitrate Coordination Polymers with Double-Headed 2-pyrrolidone Derivatives, Preprint of AESJ Spring Mtg., Fukushima, 2E05, (2020).

(58) Takao, K., Kaneko, M., Tsushima, S., Development of Advanced Adsorbent for Uranium Recovery from Seawater Based on Uranyl Coordination Chemistry (1) Molecular Design of Planar Pentadentate Ligand and Synthesis of Its Uranyl Complex, Preprint of AESJ Spring Mtg., Fukushima, 1E01, (2020).

(59) Anna V Gubarevich, Jelena Maletaskic, Katsumi Yoshida: Combustion synthesis of MAX phase solid solutions in Ti-Zr-Al-C and Ti-Zr-Si-C systems; *5th Conference of the Serbian Society for Ceramic Materials*, June 11, 2019, Belgrade, Serbia (Invited).

(60) Toru Tsunoura, Katsumi Yoshida, Toyohiko Yano, Takuya Aoki, Toshio Ogasawara: Oxidation behavior of $HfSi_2$ with boron addition; 43rd International Conference and Exposition on Advanced Ceramics and Composites, January 28, 2019, Florida, USA, ICACC-S1-003-2019.

(61) Toru Tsunoura, Katsumi Yoshida, Toyohiko Yano, Takuya Aoki, Toshio Ogasawara: Fabrication of SiC/silicides composites by melt infiltration method; 43rd International Conference and Exposition on Advanced Ceramics and Composites, January 29, 2019, Florida, USA, ICACC-S1-026-2019.

(62) Toru Tsunoura, Kenji Miyashita, Ryuki Tahara, Katsumi Yoshida, Toyohiko Yano: Fabrication and plasma corrosion behavior of yttrium oxyfluoride ceramics; 43rd International Conference and Exposition on Advanced Ceramics and Composites, January 29, 2019, Florida, USA, ICACC-CYIF-P001-2019.

(63) Muzakkiy P. M. Akihr, Katsumi Yoshida: Molecular Dynamics Simulation of a Primary Knocked Atom Collision Cascade on 3C-SiC Ceramics at Reactor-Relevant Temperatures; The 11th International Conference on the Science and Technology for Advanced Ceramics (STAC-11), Tsukuba, Japan, July 9, 2019, 1P-22.

(64) Yanzhou Hou, Anna Gubarevich, Katsumi Yoshida: Fabrication and properties of titanium-based ternary materials; The 11th International Conference on the Science and Technology for Advanced Ceramics (STAC-11), Tsukuba, Japan, July 9, 2019, 1P-28.

(65) Thanataon Pornphatdetaudom, Katsumi Yoshida, Tohru S. Suzuki, Toyohiko Yano: Effect of Particle Orientation on Lattice Parameter and Recovery Changes in Aluminum Nitride; The 11th International Conference on the Science and Technology for Advanced Ceramics (STAC-11), Tsukuba, Japan, July 9, 2019, 1P-29.

(66) Muhammad Fajar, Tohru S. Suzuki, Katsumi Yoshida, Toyohiko Yano, Anna Gubarevich: Study of Al_2O_3 addition effect on densification of B4C textured using rotating strong magnetic field by slip-casting; The 11th International Conference on the Science and Technology for Advanced Ceramics (STAC-11), Tsukuba, Japan, July 10, 2019, 2a-401-05.

(67) Ryosuke S.S. Maki, Muhammad Fajar, Jelena Maletaskic, Anna Gubarevich, Tatsuya Katabuchi, Toyohiko Yano, Katsumi Yoshida, Tohru S. Suzuki, Tesuo Uchikoshi: Release Behavior of Helium Gas in the He-Implanted Highly Microstructure-Controlled B_4C-based Ceramic Neutron Absorber; The 11th International Conference on the Science and Technology for Advanced Ceramics (STAC-11), Tsukuba, Japan, July 10, 2019, 2P-09.

(68) Katsumi Yoshida, Tohru S. Suzuki, Koji Maeda: Development of Highly Microstructure-Controlled Boron Carbide Neutron Absorbers for Fast Reactors; International Conference on Materials Science and Engineering 2019, Melbourne, Australia, September 17, 2019 (Invited).

(69) Takuya Aoki, Toru Tsunoura, Katsumi Yoshida, Naoki Hayama, Takaya Sawahiraki, Ryuta Kitamura, Shinji Ogihara, Toshio Ogasawara: SiC fiber-reinforced CoSi matrix composite fabricated by melt infiltration processing; 10th International Conference on High Temperature Ceramic Matrix Composites (HT-CMC10), Bordeaux, France, September 23, 2019, 2213.

(70) Katsumi Yoshida, Mayuko Kasakura, Ryo Shirata, Takashi Ajito Takashi, Toyohiko Yano, Masaki Kotani: Mechanical Properties of SiC_f/SiC Composites with BN Interphase Formed by Electrophoretic Deposition; 10th International Conference on High Temperature Ceramic Matrix Composites (HT-CMC10), Bordeaux, France, September 23, 2019, 2241.

(71) Mayuko Kasakura, Katsumi Yoshida, Masaki Kotani: Formation of BN interphase for SiC_f/SiC composites using flaked BN suspension by electrophoretic deposition method; 10th International Conference on High Temperature Ceramic Matrix Composites (HT-CMC10), Bordeaux, France, September 25, 2019, 2453.

(72) Anna V. Gubarevich, Jelena Maletaskic, Katsumi Yoshida: Synthesis and Thermal Stability of $Ti_{3-x}Zr_xSiC_2$ MAX Phase Solid Solutions; The 13th Pacific Rim Conference of Ceramic Societies

(PacRim13), Okinawa, Japan, October 28, 2019, 28-A3-S03-05.

(73) Ying Chung, Anna Gubarevich, Katsumi Yoshida: Effects on Microstructure of Silicon Carbide Ceramics with Boron and Aluminum Additives; The 13th Pacific Rim Conference of Ceramic Societies (PacRim13), Okinawa, Japan, October 29, 2019, 29-P-S13-08.

(74) Tsubasa Watanabe, Anna Gubarevich, Katsumi Yoshida: Combustion synthesis of single-phase Al_4SiC_4 powder by induction heating; The 13th Pacific Rim Conference of Ceramic Societies (PacRim13), Okinawa, Japan, October 29, 2019, 29-P-S13-09.

(75) Shota Azuma, Tetsuo Uchikoshi, Katsumi Yoshida, Tohru S. Suzuki: Evaluation of Highly Structured B_4C Ceramics Prepared via Strong Magnetic Field-Assisted Colloid Processing; The 13th Pacific Rim Conference of Ceramic Societies (PacRim13), Okinawa, Japan, October 29, 2019, 29-P-S13-19.

(76) Ryosuke S.S. Maki, Muhammad Fajar, Jelena Maletaskic, Anna Gubarevich, Toyohiko Yano, Katsumi Yoshida, Tohru S. Suzuki, Tetsuo Uchikoshi: High thermal shock resistance B_4C/CNT composite fabricated by hot-pressing method; The 13th Pacific Rim Conference of Ceramic Societies (PacRim13), Okinawa, Japan, October 29, 2019, 29-P-S13-23.

(77) Muhammad Fajar, Anna Gubarevich, Tohru S. Suzuki, Toyohiko Yano, Katsumi Yoshida: Processing and Properties of Textured Boron Carbide Ceramic with Alumina Additive Fabricated Under Rotating High Magnetic Field; The 13th Pacific Rim Conference of Ceramic Societies (PacRim13), Okinawa, Japan, October 30, 2019, 30-B1C-S13-13.

(78) Katsumi Yoshida, Tatsuya Nakane, Anna Gubarevich, Yutaka Shinoda, Yoshikazu Suzuki: Sintering of Silicon Carbide Ceramics with Al_2O_3-TiO_2 Additives by Hot- Pressing and Its Properties; The 13th Pacific Rim Conference of Ceramic Societies (PacRim13), Okinawa, Japan, October 30, 2019, 30-B1C-S13-17.

(79) Hiroaki Ashizawa, Masakatsu Kiyohara, Katsumi Yoshida: Plasma Corrosion Behavior of Yttrium Oxide Coating prepared by Aerosol Deposition Method; The 13th Pacific Rim Conference of Ceramic Societies (PacRim13), Okinawa, Japan, October 31, 2019, 31-B1C-S13-28 (Invited).

(80) Hiroaki Ashizawa, Katsumi Yoshida: Effect of the microstructures of Yttria Coatings on their Fluorination Behavior in Fluorine-based Plasma; 41st International Symposium on Dry Process (DPS2019), Hiroshima, Japan, November 22, 2019, P-9.

(81) Kenji Miyashita, Katsumi Yoshida, Toyohiko Yano: Corrosion behavior of yttrium oxyfluoride ceramics in HCl and HNO_3 solution; 41st International Symposium on Dry Process (DPS2019), Hiroshima, Japan, November 22, 2019, P-14.

(82) Anna V. Gubarevich, Katsumi Yoshida: Combustion synthesis of submicron B_4C with induction heating assistance; Materials Research Meeting 2019 (MRM 2019), Yokohama, December 12, 2019, C3-12-O10.

(83) Ryuki Tahara, Katsumi Yoshida: Evaluation for hydrothermal corrosion resistance of neutron irradiated SiC and SiC_f/SiC composites; 12th Student Meeting of the Kanto-Koetsu Division of the Atomic Energy Society of Japan, Tokyo, March 8, 2019, B01.

(84) Thanataon Pornphatdetaudom, Katsumi Yoshida, Toyohiko Yano, Tohru S. Suzuki: Lattice Parameter Change of Highly Oriented Aluminum Nitride by Neutron Irradiation; 12th Student Meeting of the Kanto-Koetsu Division of the Atomic Energy Society of Japan, Tokyo, March 8, 2019, B02.

(85) Muhammad Fajar, Tohru S. Suzuki, Anna Gubarevich, Toyohiko Yano, Katsumi Yoshida: Investigation of crystallographic orientation of boron carbide fabricated in high magnetic field for improvement of fast breeder reactor; 12th Student Meeting of the Kanto-Koetsu Division of the Atomic Energy Society of Japan, Tokyo, March 8, 2019, B05.

(86) Katsumi Yoshida, Tohru S. Suzuki, Koji Maeda: Development of Highly Microstructure-Controlled Ceramic Neutron Absorbers for Improving Safety of Fast Reactors (1) Outline of the Research Program; 2019 Annual Meeting of the Atomic Energy Society of Japan, Mito, March 21, 2019, 2M01.

(87) Ryosuke S. S. Maki, Fajar Muhammad, Jelena Maletaskic, Anna Gubarevich, Tatsuya Katabuchi, Toyohiko Yano, Yoshida Katsumi, Tohru S. Suzuki, Tetsuo Uchikoshi: Development of Highly Microstructure-Controlled Ceramic Neutron Absorbers for Improving Safety of Fast Reactors (2) Fabrication and Helium Implantation Test of Carbon Nanotube-added B_4C-based Ceramics; 2019 Annual Meeting of the Atomic Energy Society of Japan, Mito, March 21, 2019, 2M02.

(88) Tohru S. Suzuki, Shota Azuma, Tetsuo Uchikoshi, Katsumi Yoshida: Development of Highly Microstructure-Controlled Ceramic Neutron Absorbers for Improving Safety of Fast Reactors (3) Control of crystallographic orientation in ceramics for Fast Reactors by a magnetic field; 2019 Annual Meeting of the Atomic Energy Society of Japan, Mito, March 21, 2019, 2M03.

(89) Shota Azuma, Tetsuo Uchikoshi, Katsumi Yoshida, Tohru S. Suzuki: Development of Highly Microstructure-Controlled Ceramic Neutron Absorbers for Improving Safety of Fast Reactors (4) Fabrication of Highly Controlled Microstructure in B_4C Control rods by Magnetic Field-Assisted Colloidal Processing; 2019 Annual Meeting of the Atomic Energy Society of Japan, Mito, March 21, 2019, 2M04.

(90) Shigetaka Maeda, Wataru Itagaki, Koji Maeda, Ryosuke S. S. Maki, Katsumi Yoshida: Development of Highly Microstructure-Controlled Ceramic Neutron Absorbers for Improving Safety of Fast Reactors (5) Evaluation of effect on control rod worth; 2019 Annual Meeting of the Atomic Energy Society of Japan, Mito, March 21, 2019, 2M05.

(91) Yuta Shizukawa, Koji Maeda, Toshihiko Inoue, Yoshihiro Sekio, Katsumi Yoshida: Development of Highly Microstructure-Controlled Ceramic Neutron Absorbers for Improving Safety of Fast Reactors (6) Evaluation of Microstructure of B_4C Absorber Material for Fast Reactor after Irradiation; 2019 Annual Meeting of the Atomic Energy Society of Japan, Mito, March 21, 2019, 2M06.

(92) Kohei Yoshida, Jelena Maletaskic, Anna Gubarevich, Katsumi Yoshida: Fabrication of $LaPO_4$-coated Al_2O_3-basedfiber/Al_2O_3 matrix composites and their mechanical properties; Annual Meeting of The Ceramic Society of Japan, 2019, Tokyo, March 24, 2019, 1P018.

(93) Anna V. Gubarevich, Jelena Maletaskic, Katsumi Yoshida: Synthesis of novel $Zr_xTi_{3-x}SiC_2$ MAX phase solid solutions; Annual Meeting of The Ceramic Society of Japan, 2019, Tokyo, March 25, 2019, 2F09.

(94) Toru Tsunoura, Katsumi Yoshida, Toyohiko Yan, Naoki Hayama, Takaya Sawahiraki, Takuya Aoki, Toshio Ogasawara: Fabrication of tensile test specimens of unidirectional SiC fiber-reinforced composites by melt infiltration; Annual Meeting of The Ceramic Society of Japan, 2019, Tokyo, March 25, 2019, 2K07.

(95) Hiroaki Ashizawa, Masakatsu Kiyohara, Katsumi Yoshida: Effect of Microstructure of Y_2O_3 coatings on their Plasma Corrosion Behavior; Annual Meeting of The Ceramic Society of Japan, 2019, Tokyo, March 25, 2019, 2K23.

(96) Ryosuke S. S. Maki, Fajar Muhammad, Jelena Maletaskic, Anna Gubarevich, Katsumi Yoshida, Toyohiko Yano, Tohru S. Suzuki, Tetsuo Uchikoshi: Residual strength of B_4C-base ceramic neutron absorber after thermal shock testing; Annual Meeting of The Ceramic Society of Japan, 2019, Tokyo, March 26, 2019, 3K19.

(97) Y. Izumoto, K. Takamura, T. Matsuyama, H. Nagai, Y. Sakai, Y. Oguri, H. Yoshii: TXRF Analysis of Uranium in the Presence of Competing Elements; *18th International Conference on Total Reflection X-ray Fluorescence Analysis and Related Methods (TXRF2019)*, June 25-28, 2019, Centre Cultural La Mercè, Girona, Spain.

(98) Y. Izumoto, K. Fukutsu, K. Takamura, H. Yoshii, Y. Oguri, Y. Sakai: Evaluation of Uranium and Plutonium in Simulated Blood Extracted from Wounds by X-ray Fluorescence Analysis; *68th Denver X-ray Conference*, August 5-9, 2019, the Westin Lombard Yorktown Center, IL, USA, F-44.

(99) Y. Oguri, J. Hasegawa, H. Fukuda, N. Hagura: FT-IR Measurement on the Damage of Japanese Paper Induced by PIXE Analysis; *35th Annual Meeting of the Japan Society for Particle Induced X-ray Emission (PIXE) Research*, November 13-15, 2019, Tokyo City University, Tokyo, Japan, #2-1.

(100) Y. Oguri, J. Hasegawa, H. Fukuda, N. Hagura: FT-IR Analysis on the Damage of Simulated Cultural Heritage Samples Induced by Ion-Beam and X-Ray Irradiation; *2020 Annual Meeting of Atomic Energy Society of Japan*, March 16-18, 2020, Fukushima University, Fukushima, Japan, 3O05.

(101) Kaima Tsukada, Carl Morrow, Mikio Shimada, Yoshihisa Matsumoto, Andrew N Blackford: DNA repair mechanism regulated by BLM; *56th Isotope and Radiation Research Workshop*, Tokyo July 3-5, 2019, 2a-III-04 (Presentation Award).

(102) Mikio Shimada, Tomoko Miyake, Yoshihisa Matsumoto: Analysis of radiation response of skin keratinocyte derived from human iPS cells. *56th Isotope and Radiation Research Workshop*, Tokyo, July 3-5, 2019, 2a-III-09.

(103) Kaima Tsukada, Morrow Carl, Mikio Shimada, Yoshihisa Matsumoto, Andrew N Blackford: Mechanisms for DNA repair and maintenance of genomic stability regulated by BLM helicase; *2019 Research Workshop of Young Radiation Biologists' Association in Japan*, Chiba, September 8, 2019 (Presentation Award).

(104) Rikiya Imamura, Kaima Tsukada, Kotaro Saikawa, Mikio Shimada, Yoshihisa Matsumoto: Role of DNA repair fator PNKP in cell cycle checkpoint; *2019 Research Workshop of Young Radiation Biologists' Association in Japan*, Chiba, September 8, 2019.

(105) Kaima Tsukada, Rikiya Imamura, Kotaro Saikawa, Mikio Shimada, Yoshihisa Matsumoto: Elucidation of the novel function and signaling pathway of DNA repair factor PNKP; *25th DNA Replication, Recombination and Repair Workshop*, Nara, November 9-11, 2020 (Presentation Award).

(106) Rujira Wanotayan, Natpapus Sitthirat, Tharit Khununyhaporn, Kamolporn Sasoda, Petchlada Sopon, Papichaya Yudech, Tanwiwat Jaikuna, Kulachart Jangpatarapongsa, Yoshihisa Matsumoto. Enhancement effect of gold nanoparticle on radiotherapy of MDA-MB-231 and HeLa cells. *62nd Annual Meeting of Japanese Radiation Research Society*, November 14-16, 2020, OS6-5.

(107) Yoshihisa Matsumoto: Recognition and repair of DNA double-strand breaks: from molecular mechanism to application in cancer radiotherapy; *32nd Annual Meeting of Japan Society for Radiation Oncology*, Nagoya, November 21-23, 2020, S2-3.

(108) C. Ishizuka: Study on Nuclear Fission at Tokyo Tech.; *YITP workshop "Nuclear Fission Dynamics 2019"*, Kyoto, October 26-November 8, 2019.

(109) Kazuki Fujio, Shuichiro Ebata, Satoshi Chiba: Study of fission path on ^{236}U with the microscopic mean-field theory; *The international workshop on nuclear physics for astrophysical phenomena*, Tokyo, October 23-25, 2019.

(110) C. Ishizuka, X. Zhang, M.D. Usang, F.A. Ivanyuk, S. Chiba:The international workshop on nuclear physics for astrophysical phenomena; *2019 Fall Meeting of Atomic Energy Society of Japan*, Toyama, September 11-13, 2019, 3M05.

(111) T. Inakura, N. Yamano, C. Ishizuka, S. Chiba: A

study of uncertainty due to nuclear data in a long-lived fission product (LLFP) transmutation system utilizing a fast reactor (1) Estimation of covariance of neutron capture cross section of LLFP; *2019 Fall Meeting of Atomic Energy Society of Japan*, Toyama, September 11-13, 2019, 2M07.

(112) N. Yamano, T. Inakura, C. Ishizuka, S. Chiba: A study of uncertainty due to nuclear data in a long-lived fission product (LLFP) transmutation system utilizing a fast reactor (2) Uncertainty of reaction rate due to neutron capture cross section error of LLFP; *2019 Fall Meeting of Atomic Energy Society of Japan*, Toyama, September 11-13, 2019, 2M08.

(113) T. Amitani, T. Inakura, N. Yamano, K. Tanaka, C. Ishizuka, S. Chiba: Estimation of covariance of neutron cross sections for reactor decommissioning; *2019 Fall Meeting of Atomic Energy Society of Japan*, Toyama, September 11-13, 2019, 2M09.

(114) H. Miyuki, G. Shinzawa, K. Ueda, S. Haga, Y. Kodama, T. Miyakawa, N. Yamano, K. N. Ishihara: Class-On-Demand “Radiation Education and HLW Geological disposal” in Elementary schools in Japan Transition of the last eight years; *2019 Fall Meeting of Atomic Energy Society of Japan*, Toyama, September 11-13, 2019, 1H13.

(115) H. Miyuki, G. Shinzawa, K. Ueda, S. Haga, Y. Kodama, T. Miyakawa, N. Yamano, K. N. Ishihara: Class-On-Demand “HLW Geological disposal” in Elementary schools in Japan, Application of Miyu Cafe; *2019 Annual Meeting of Japan Association of Energy and Environmental Education*, Kochi, August 5-7, 2019, 2D-1.

(116) K. Fujio, S. Ebata, S. Chiba: Study of the fission path on U-236 with the microscopic mean-field model; *2019 Fall Meeting of Atomic Energy Society of Japan*, Toyama, September 11-13, 2019, 3M08.

(117) X. Zhang, C. Ishizuka, T. Inakura, F.A. Ivanyuk, S. Chiba: Nuclear shape of fission fragments and their deformation energies; *2019 Fall Meeting of Atomic Energy Society of Japan*, Toyama, September 11-13, 2019, 3M06.

(118) T. Inakura, N. Yamano, C. Ishizuka, S. Chiba: Research and development of an innovative transmutation system of LLFP by fast reactors (6) Evaluation of covariance of cross section of LLFP; *2020 Annual Meeting of Atomic Energy Society of Japan*, Fukushima, March 16-18, 2020, 2H15.

(119) N. Yamano, T. Inakura, C. Ishizuka, S. Chiba: Research and development of an innovative transmutation system of LLFP by fast reactors (7) Estimation of uncertainty on transmutation rate; *2020 Annual Meeting of Atomic Energy Society of Japan*, Fukushima, March 16-18, 2020, 2H16.

(120) T. Amitani, T. Inakura, N. Yamano, K. Tanaka, C. Ishizuka, S. Chiba: Estimation of Covariance of Neutron Cross Sections for Decommissioning; *2020 Annual Meeting of Atomic Energy Society of Japan*, Fukushima, March 16-18, 2020, 2O01.

(121) K. Fujio, S. Ebata, S. Chiba: Energy valance and the fission path on U-236 with the microscopic mean-field theory; *2020 Annual Meeting of Atomic Energy Society of Japan*, Fukushima, March 16-18, 2020, 1O04.

(122) C. Ishizuka, X. Zhang, M.D. Usang, F.A. Ivanyuk, S. Chiba: Systematic study on nuclear fission of SHEs using 4D Langevin model; *2020 Annual Meeting of The Physical Society of Japan*, Nagoya, March 16-19, 2020, 16pK15-3.

(123) X. Zhang, C. Ishizuka, T. Inakura, F.A. Ivanyuk, S. Chiba: Excitation energy of fission fragments and prompt neutron multiplicity; *2020 Annual Meeting of Atomic Energy Society of Japan*, Fukushima, March 16-18, 2020, 1O02.

(124) S. Chiba: Correlated transition of TKE and mass distributions in nuclear fission; *International Conference on Nuclear Data for Science and Technology (ND2019)*, Beijing, China, May 19-24, 2019.

(125) S. Chiba: Recent progress on study of nuclear fission and synthesis of super heavy element and r-process nucleosynthesis; *YITP workshop* “*Recent progress on study of nuclear fission and synthesis of super heavy element and r-process nucleosynthesis”*, Kyoto, May 22-24, 2019.

(126) S. Chiba: Needs for and requests to fission-related data compilation from theory and evaluation viewpoints; *IAEA Consultancy Meeting on the Fission Product Yield Experimental Database*, Tokyo, May 27-30, 2019.

(127) S. Chiba, M.D. Usang, C. Ishizuka, F.A. Ivanyuk, X. Zhang: Systematic and anomalous trends in fragment mass and TKE distributions and fragment shape in terms of 4D Langevin model; *Fifth edition of the THEORY Scientific Workshop on "Nuclear Fission Dynamics and the Emission of Prompt Neutrons and Gamma Rays" (THEORY-5)*, Barga, Italy, September 24-26, 2019.

(128) S. Chiba, M.D. Usang, C. Ishizuka, F.A. Ivanyuk, X. Zhang: Correlated transitions in symmetric and dominant fission modes, and multipole moments of fission fragments; *International Workshop on Fission Product Yields 2019)*, Santa Fe, U.S.A., September 30-October 4, 2019.

(129) S. Chiba, M.D. Usang, C. Ishizuka, F.A. Ivanyuk, X. Zhang: Deformation of Fission Fragments at Scission studied by 4D Langevin Model; *The 14th Asian-Pasific Physics Conference (APPC14))*, Kuchin, Malaysia, November 17-21, 2019.

(130) S. Chiba: Research and development of an innovative transmutation system of LLFP by fast reactorss; *Annual Nuclear Data Symposium*, Fuoka., November 28-19, 2019.

(131) Hiroshi Akatsuka, Hiroshi Onishi, Thijs van der Gaag, Atsushi Nezu: Diagnostics of Electron Parameters of Atmospheric-Pressure Non-Equilibrium Plasmas by OES Measurement of Continuum Spectrum; *2019 Annual Meeting of the*

Spectroscopical Society of Japan, Uji, May 14-16, 2019, p. 92.

(132) Hiroshi Akatsuka, Hiroshi Onishi, Thijs van der Gaag, Atsushi Nezu: Optical Emission Spectroscopic Measurement of Continuum Radiation of Atmospheric-PressureNon-Equilibrium Argon Plasma; *2019 Annual Conference of Fundamentals and Materials Society IEE of Japan*, Morioka, September 3-4, 2019, p. 216, 3-D-a2-1.

(133) June Konami, Atsushi Nezu, Hiroshi Akatsuka: Radial Dependence of Rotational Temperature of N_2 and N_2^+ in Nitrogen Plasma, *80th JSAP Autumn Meeting 2019*, Sapporo, September 18-21, 2019, 20a-B11-1.

(134) Yuya Yamashita, Hiroshi Akatsuka: The Excited-State Distribution Analysis of the Low-Pressure Microwave Discharge Argon Plasma for Electron Energy Distribution Function Diagnosis by Optical Emission Spectroscopic Measurement; *80th JSAP Autumn Meeting 2019*, Sapporo, September 18-21, 2019, 20a-B11-2.

(135) Hugo Lavigne, Tomohiro Shiroi, Atsushi Nezu, Kiyoyuki Yambe, Hiroshi Akatsuka: Optical Emission Spectroscopic Measurement of Electron Temperature with Continuum Emission of Atmospheric-Pressure Non-Equilibrium Ar-CO_2 Mixed Plasma; *36th Annual Meeting of Japan Society of Plasma Science and Nuclear Fusion Research*, Kasugai, November 29 – December 2, 2019, 02Ba06.

(136) Kiyoyuki Yambe, Tomoya Izumids, Hiroshi Akatsuka: Evaluation of Electron Density and Temperature using CR model in Interaction between Metal Object and Atmospheric Non-Thermal Argon Plasma; *36th Annual Meeting of Japan Society of Plasma Science and Nuclear Fusion Research*, Kasugai, November 29 – December 2, 2019, 02P76.

(137) Shota Yamada, Yuki Morita, Atsushi Nezu, Hiroshi Akatsuka: Non-Equilibrium of Rotational Distribution of Electronic Excited States of Carbon Monoxide Molecule in Microwave Discharge Carbon Dioxide Plasma; *2019 Joint workshop on "Forefront of fusion of plasma spectroscopy and atomic/molecular elementary process research" "Atomic and molecular data application forum seminar"*, Toki, December 24-26, 2019.

(138) Yuya Yamashita, Hiroshi Akatsuka: Dependence of Excited State Number Density Distribution on Electron Density, Temperature and Energy Distribution Function of Argon Plasma Based on Global-Model and Collisional Radiative Model; *2019 Joint workshop on "Forefront of fusion of plasma spectroscopy and atomic/molecular elementary process research" "Atomic and molecular data application forum seminar"*, Toki, December 24-26, 2019.

(139) Hiroshi Akatsuka: Diagnostics of Plasma Parameters of Optical Emission Spectroscopy (OES) Measurement; *223rd Research Meeting of Silicon Technology Division "Nano-machining precision and damage control in plasma process", Japanese Society of Applied Physics*, Tokyo, February 14, 2019.

(140) Shota Yamada, Yuki Morita, Atsushi Nezu, Hiroshi Akatsuka: Non-Equilibrium Rotational Energy Distribution of Electronically Excited States of CO Molecules in Reduced-Pressure CO_2 Plasma; *67th JSAP Spring Meeting 2020*, Tokyo, March 12-15, 2020, 06-006, 12p-A302-6.

(141) Hiroshi Akatsuka, Jun Takeda, Atsushi Nezu: Measurement of Diamagnetic Current and $\boldsymbol{E} \times \boldsymbol{B}$ Drift of Electrons in a Radial Electric Field and Longitudinal Magnetic Field in a Linear Device with Mach Probe; *2020 Annual (75th) Meeting of the Physical Society of Japan*, Nagoya, March 16-19, 2020, Vol. **75**, No. 1, p. 810, 17aD13-5.

(142) Shintaro Yasui, and Hiroshi Funakubo: (Invited) Lead-free Tetragonal Ferroelectric Material: $Bi(Zn_{1/2}Ti_{1/2})O_3$- based; *The 36th International Japan-Korea Seminar on Ceramics(JK-Ceramics 36)*, Tottori, Nov. 21, 2019.

(143) Shintaro Yasui, Tsukasa Katayama, Yosuke Hamasaki, Takahisa Shiraishi, Akihiro Akama, Takenori Kiguchi, Ayako Konishi, Hiroki Moriwake, and Mitsuru Itoh: Kappa-almina-type Structured Multiferroics; *International Conference on Materials and Systems for Sustainability 2019 (ICMaSS 2019)*; Nagoya, Nov. 2, 2019.

(144) Shintaro Yasui: (Invited) Pb-free perovskite thin films and their piezoelectricity at MPB, *Asia-Pacific PFM 2019*; Seoul, Aug. 14, 2019.

(145) Shintaro Yasui: (Invited) Ultra-High Rate Performance of Li Thin Film Battery with $BaTiO_3$, *International Conference on Materials for Advanced Technologies (ICMAT2019)*; Singapore, June 26, 2019.

(146) Mochizuki, H.,Chiba, S., Research and development of an innovative transmutation system of LLFP by fast reactors (5) Thermal integrity evaluation of LLFP targets, Preprint of AESJ Spring Mtg., 2H14, (2020), 2H14.

(147) Mochizuki, H., Consideration on Heat Transfer Coefficient of Liquid Metal in Tube Flow, Preprint of AESJ Spring Mtg., 3I10,（2019）,3I10.

(148) Mochizuki, H., Yamawaki, M., Coupled Neutronics and Thermalhydraulics of Molten Salt Fast Reactor, Preprint of AESJ Fall Mtg., 2F09,（2019）, 2F09.

BULLETIN OF THE
LABORATORY FOR ADVANCED NUCLEAR ENERGY

Vol.5 2020

2021年2月　印刷

編集兼
発行者　東京工業大学科学技術創成
研究院先導原子力研究所
責任者　竹　下　健　二
〒152-8550 東京都目黒区大岡山2丁目12-1
電話　03－5734－3052
FAX　03－5734－2959

印刷所　昭和情報プロセス㈱
東京都港区三田5－14－9

Printed by
SHOWA JOHO PROCESS
Minato-ku, Tokyo, Japan